

Motion Control for Haptics and Its Application to Delayed Communication Systems

September 2015

A thesis submitted in partial fulfilment of the requirements for the degree of
Doctor of Philosophy in Engineering



Keio University

Graduate School of Science and Technology
School of Integrated Design Engineering

Shoyo Hyodo

Acknowledgements

I joined Professor Ohnishi's laboratory in 2005 when I was an undergraduate student, and I had been with the laboratory for three years. After receiving the M.E. degree in 2008, I joined Mitsubishi Heavy Industries, Ltd where I have been engaged in researches and developments of space transportation systems. In 2013, I decided to join Professor Ohnishi's laboratory again in order to complete my work. This dissertation is the result of five years of work at Keio University whereby I have been supported and encouraged by many people. I would like to express my gratitude to all those who gave me the possibility to complete this dissertation here.

First of all, I would like to express my deep and sincere gratitude to my supervisor Professor Dr. Kouhei Ohnishi in Keio University. His stimulating, critical and thoughtful comments and his warming support throughout this work are a great help to me. He taught me how to create own research fields and provided me a lot of opportunity to attend conferences and discussions with other researchers in the world. These experiences are fortune in my life. In the future, I would like to be a researcher who creates valuable domains from invisible areas like him.

I greatly appreciate to the members of my Ph.D. dissertation committee, Professor Dr. Satoshi Honda in Keio University, Professor Dr. Ikehara Masaaki in Keio University, and Associate Professor Dr. Takahiro Yakoh in Keio University. It was a great opportunity for me to review my research and consider it more deeply.

I also would like to express my sincere gratitude to Professor Dr. Toshiyuki Murakami, Keio University Professor Dr. Yutaka Uchimura, Shibaura Institute University and Associate Professor Dr. Seiichi Katsura, Keio University for giving me beneficial advices through technical meetings. Associate Professor Dr. Toshiaki Tsuji, Saitama University, Associate Professor Dr. Tomoyuki Shimono, Yokohama National University, Assistant Professor Dr. Kenji Natori, Chiba University and Assistant Professor Dr. Motoi Naoki, Kobe University are giving me a lot of interesting comments and warm advices. Assistant Professor Dr. Ryogo Kubo, Keio University taught me how to make a research when I joined Ohnishi laboratory. Discussions with him make the basement of my research about haptics. Assistant Professor Dr. Sho Sakaino, Saitama University and Assistant Professor Dr. Daisuke Yashiro, Mie University gave me a lot of constructive discussions. Assistant Professor Dr. Takahiro Nozaki, Keio University and

Dr. Takahiro Mizogushi, Kanagawa Academy of Science and Technology are kindly guiding the laboratory when I visited there for starting as a Ph.D. student. They gave me helpful supports to continue a research. Mr. Kazuki Tanida, Keio University Mr. Yoshiki Ohno, Canon, Ltd and Mr. Shuhei Shimizu, Keio University are always supporting me to conduct experiments. I gratefully acknowledge to the all of current and past SUM members including colleagues in Ohnishi laboratory, who gave me discussions, assistances and comments for all of my works. They kindly took me in and helped me a lot. I enjoyed spending time with them.

I greatly appreciate my bosses and colleagues in Mitsubishi Heavy Industries, Ltd. Mr. Mitsutoshi Tsujioka and Mr. Yoshichika Tanabe who are my supervisors gave me a chance to engage in the doctoral program and always supported me.

I would like to express my sincere thanks and appreciations to my family. My father is an engineer and motivated me to the world of engineering. My mother has cheered me up by kind words. My wife, Riho has supported me emotionally and warmly by her humor.

I would like to express my gratitude again to all those who supported my research.

September, 2015
Shoyo Hyodo

Contents

Acknowledgements	i
Table of Contents	ii
List of Figures	vi
List of Tables	x
1 Introduction	1
1.1 Background	1
1.1.1 Tactile Sense	1
1.1.2 Haptics	3
1.1.3 Application to Network System	4
1.2 Orientation of Research	4
1.3 Chapter Organization	5
2 Fundamental Technology of Motion Control	8
2.1 Motion Control Based on Acceleration Control	8
2.1.1 Disturbance Observer	9
2.1.2 Reaction Force Observer	11
2.2 Control System	11
2.2.1 Position Control	13
2.2.2 Force Control	14
2.2.3 Compliance Control	15
2.3 Control System Based on Virtual Space	16
2.3.1 Virtual Space	16
2.3.2 Bilateral Control Based on Differential Mode and Common Mode	17
2.4 Summary	18

3	Robot Hand Using Flexible Actuator	19
3.1	Background and Outline	19
3.2	Flexible Actuator	20
3.2.1	Outline of Flexible Actuator	20
3.2.2	Thrust Wire	21
3.3	Verification of Flexible Actuator	22
3.3.1	Verification System	22
3.3.2	Verification Result	26
3.4	Application to Bilateral Teleoperation System	29
3.4.1	Bilateral Teleoperation System with Flexible Actuator	29
3.4.2	Experimental Result	30
3.5	Summary	32
4	Reproduction of Environment Based on Frequency Characteristic	33
4.1	Background and Outline	33
4.2	Abstraction of Environment Based on Frequency Characteristic	35
4.2.1	Modeling of Environment	35
4.2.2	Control System	35
4.3	Reproduction of Environment Using FIR Filter	36
4.3.1	Design of FIR Filter for Reproduction of Environment	37
4.3.2	Control System	39
4.4	Experiment	41
4.4.1	Experimental System	41
4.4.2	Experimental Result	42
4.5	Summary	48
5	Haptic Motion Display System Based on Directionality	49
5.1	Background and Outline	49
5.2	Abstraction of Human Motion	54
5.2.1	Master-Slave System	54
5.2.2	Control System	54
5.2.3	Action Mode and Action Index	55
5.3	Motion Display System Based on Force Information	58
5.3.1	Outline of Motion Display System Based on Force Information	58
5.3.2	Control System	58
5.3.3	Experiment	60

5.4	Motion Display System Based on Position and Force Information	65
5.4.1	Outline of Motion Display System Based on Position and Force Information . .	65
5.4.2	Control System	65
5.4.3	Design of Modal Compliance Controller	67
5.4.4	Experiment	70
5.5	Summary	75
6	Motion Control System with Time Delay	76
6.1	Background and Outline	76
6.2	Time Delay Compensation	77
6.2.1	Time Delay Effect	77
6.2.2	Time Delay Compensation by CDOB	78
6.3	Time Delay Compensation Considering Unstable Time Delay	81
6.3.1	Candidate for the structure of CDOB	81
6.3.2	Simulation	83
6.3.3	Discussion	86
6.4	Experiment	91
6.4.1	Experimental System	91
6.4.2	Experimental Result	92
6.5	Summary	93
7	Bilateral Teleoperation System with Time Delay	94
7.1	Background and Outline	94
7.2	Time Delay Problem	97
7.3	Time Delay Compensation with Model-Based Compensator	99
7.3.1	Communication Disturbance Observer	99
7.3.2	Stability Analysis in Modal Space	100
7.3.3	Stability Improved Bilateral Control Structure	103
7.3.4	Discussion of Stability and Performance	106
7.3.5	Experiment	112
7.4	Time Delay Compensation with Model-Free Time Delay Compnesator	116
7.4.1	Two Flow Expression of Four-Channel Bilateral Control System	116
7.4.2	Validation of Model-Free Time Delay Compensator	119
7.4.3	Experiment	127
7.5	Synchronization of Haptic and Visual Sense	130
7.5.1	Utilization of Round Trip Time Delayed Force Information	130

7.5.2	Discussion of Stability and Performance	133
7.5.3	Experiment	138
7.6	Performance Improvement	140
7.6.1	Performance of Conventional Bilateral Control System	140
7.6.2	Allocation of HPF	141
7.6.3	Experiment	144
7.7	Summary	146
8	Conclusions	147
	References	149
	Achievements	157

List of Figures

1-1	Characteristics of various sensations.	2
1-2	Fundamental technologies of motion control for haptics.	5
1-3	Chapter organization.	6
2-1	Motion control system based on acceleration control.	9
2-2	Acceleration control based on DOB.	10
2-3	Equivalent system of Fig. 2-2.	10
2-4	Reaction force observer.	11
2-5	Position control system.	13
2-6	Force control system.	14
2-7	Compliance control system based on position control.	15
2-8	Control system based on virtual space.	16
2-9	Bilateral control system based on common mode and differential mode.	17
3-1	Flexible actuator.	20
3-2	Structure of thrust wire.	21
3-3	Verification system for position transfer characteristic.	22
3-4	Verification system for force transfer characteristic.	24
3-5	Allocation of actuator part and end-effector part.	26
3-6	Position transfer characteristic.	27
3-7	Force transfer characteristic.	28
3-8	A bilateral teleoperation system with flexible actuator.	29
3-9	Frequency spectra.	31
4-1	The process of abstraction and reproduction of environment.	34
4-2	Modeling of environment.	35
4-3	Example of frequency characteristic of environment.	36
4-4	Control system for abstraction of environment.	36
4-5	4th order FIR filter.	37

4-6	Control system for reproduction of environment.	39
4-7	Experimental system.	41
4-8	Experimental materials.	42
4-9	Band-limited signal.	43
4-10	Frequency spectrum of force response.	44
4-11	Frequency spectrum of position response.	44
4-12	Frequency spectrum of abstracted environment.	45
4-13	Impulse response of FIR filter.	46
4-14	Each frequency spectrum of environment.	46
5-1	Outline of each mode.	51
5-2	Process for motion measurement, abstraction and display.	53
5-3	Master-slave system.	54
5-4	Bilateral control system based on common mode and differential mode.	55
5-5	Motion display system based on force information.	58
5-6	Control system of motion display system based on force information.	59
5-7	Flexible actuator.	60
5-8	Experimental system.	61
5-9	Experimental cases.	62
5-10	Experimental results for motion measurement.	64
5-11	Abstracted action modes.	64
5-12	Experimental results for motion display.	64
5-13	Motion display system based on position and force information.	65
5-14	Control system of motion display system based on position and force information.	66
5-15	Experimental system.	70
5-16	Experimental results for motion measurement.	73
5-17	Abstracted action modes.	74
5-18	Experimental results for motion display.	74
6-1	Feedback control system with time delay.	77
6-2	Time delay compensation.	79
6-3	Candidate for the structure of CDOB.	82
6-4	Simulation result.	84
6-5	Analysis model.	87
6-6	Gain characteristic of transfer function of network noise n to y	90
6-7	Experimental system.	91

6-8	Experimental results.	92
7-1	Overview of teleoperation system with haptic and visual sense feedback.	95
7-2	Four-channel bilateral control system with time delay.	97
7-3	Performance deterioration from time delay.	98
7-4	Block diagram of four-channel structure with CDOB.	99
7-5	Block diagram in modal space.	102
7-6	Block diagram of the proposed structure.	105
7-7	Nyquist diagram.	107
7-8	Parametric study results of Nyquist diagram of common modal space.	109
7-9	Gain characteristics of hybrid parameter.	111
7-10	Experimental system.	112
7-11	The model and time history of time delay for case 2 to case 7.	113
7-12	Experimental results.	115
7-13	Two flow expression of acceleration based four-channel bilateral control system.	117
7-14	Time delay compensation in feedback control system.	120
7-15	Bilateral control system with model-free time delay compensator.	122
7-16	Two flow expression of bilateral control system with model-free time delay compensator.	123
7-17	Nyquist diagram for bilateral control system without and with model-free time delay compensator.	124
7-18	Parametric study results of Nyquist diagram.	126
7-19	Gain characteristics of open loop transfer function.	127
7-20	Experimental system.	128
7-21	Experimental results.	129
7-22	Bilateral control system to synchronize haptic and visual sense.	131
7-23	The advantage of using round trip time delayed force information.	132
7-24	Nyquist plot.	133
7-25	Gain characteristics of hybrid parameters.	136
7-26	Gain characteristics of reproducibility and operability.	137
7-27	Experimental system.	138
7-28	Experimental results.	139
7-29	Comparison of performance.	140
7-30	Candidates for allocating the HPF.	142
7-31	Comparisons from type 1 to type 3.	143
7-32	Experimental system.	144
7-33	Experimental results.	145

List of Tables

2.1	Control stiffness	12
3.1	Specifications of thrust wire	21
3.2	Control parameters	27
4.1	Control parameters for abstraction of environment	41
4.2	Control parameters for reproduction of environment	42
5.1	Control parameters	61
5.2	Control parameters	71
6.1	Number of communication channel passage in each CDOB.	81
6.2	Parameters for simulation and experiment.	83
7.1	Parameters for analysis and experiment	106
7.2	Parameters for analysis and experiment	125
7.3	Parameters for analysis and experiment	133
7.4	Parameters for analysis and experiment	144

Chapter 1

Introduction

1.1 Background

This section describes tactile sense and introduce researches of haptics to clarify the position of this dissertation.

1.1.1 Tactile Sense

Human beings use tactile sense to sense and recognize various motions in daily life. There will be a little time which tactile sense is not utilized. However, technologies about tactile sense are less developed compared to technologies about acoustic sense and visual sense. Mikes and speakers for recording and replaying sound have been developed maturely. In the point of visual sense, technologies about videos and televisions are developed enough. On the other hand, technologies for recording and replaying tactile sense are now developing [1]. This is caused from characteristics of tactile sense. Fig. 1-1 shows characteristics of acoustic sense, visual sense and tactile sense. As shown in Fig. 1-1, human beings sense acoustic information and visual information unilaterally. But, human beings recognize tactile sense by two motions. One is adding the action force by touching the object. The other is receiving the reaction force from the object. Bilateral motion is needed to receive tactile sense [2]. Thus, recoding and replaying of tactile sense are not realized just expanding technologies of acoustic sense and visual sense. Acoustic information and visual information are constructed in the time frame. But, tactile information should include a touching motion. This makes the development of technologies for recording and replaying tactile sense difficult.

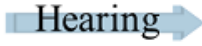
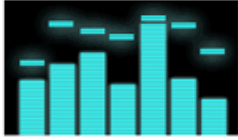
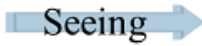
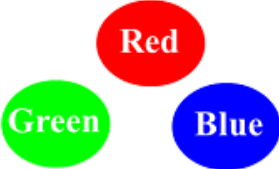
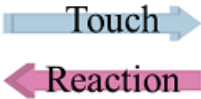
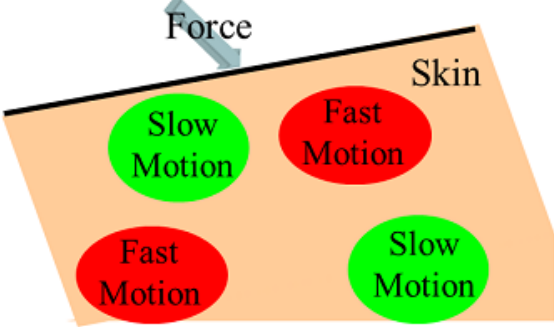
Sensation	Sensing Method	Sensing Bandwidth
Auditory Sensation 	Unilateral 	Continuous in Time Frequency 
Eyesight 	Unilateral 	Sensing the Magnitude of Red, Green and Blue Color 
Tactile Sense 	Bilateral 	Sensing the Magnitude of Fast Motion and Slow Motion 

Fig. 1-1: Characteristics of various sensations.

The ways for sensing acoustic sense, visual sense and tactile sense are diverse. Fig. 1-1 shows that human beings sense sound based on Fourier transformed acoustic information. Human beings sense visual information based on the magnitude of red, green and blue color. Human ear can recognize the frequency difference of sound. But, human eye can not recognize the continuous frequency difference of color. So, human eye cannot discriminate coupled yellow color which is made from red color and green color and pure yellow color. Human beings have two types of tactile receptors in the point of the response speed [5]. One type feels fast motion, the other type feels slow motion. And, each tactile

receptor has been allocated spatially to sense spatial differences [6].

Tactile sense is generated from reaction force. It is considered that tactile receptors sense time and spatial differences. There are many challenges to improve technologies for recording and replaying tactile sense to the level of real applications.

1.1.2 Haptics

Haptic means sense of touch. “Haptics” is defined as the research field applying tactile sensation and control to interaction with computer applications. The word haptics includes human haptics and machine haptics [7]. Human haptics focuses on how human begins recognize tactile sense from touching motions [8]. This area includes psychology, brain science and cognitive science. Machine haptics focus on how to give tactile sense to human beings. Machine haptics are trying to transmit virtual tactile sense. One of the utilization of machine haptics are joysticks for game machines or cell phones which transmit vibrations [9]. Human beings can notice that there are callings even if ring alerts cannot be recognized.

As an application of haptics, bilateral teleoperations are considered [10–13]. If tactile sense is received in the teleoperation of atomic power plants or space environments, more dexterous tasks will be achieved. Applications to micro-nano manipulations are also considered [14, 15]. Cell manipulation techniques will be improved by transmitting tactile sense exaggeratingly. It will increase the success rate of cell manipulations.

Presentations of tactile sense are researched in the field of haptics [16]. Two objectives are considered for the presentation of tactile sense. One is environment and the other is human. In the point of environment, textures of objects are focused. If textures of objects are known in internet stoppings, we can buy more preferred things. In the point of human, human motions or techniques are focused. These technologies are expected to apply in simulators for training [17]. Doctors in training can learn operations from textbooks and video images but they do not know feelings of teleoperations. By utilizing simulators which are transmitting not only sound and visual information but also tactile sense information, doctors in training rehearse operations. Haptics have many potential to enrich human life [18].

For expanding the haptics to multi degree of freedom robot hands, manipulability problems have to be considered for realizing the targeted motions. Manipulability is a quantitative measure of a manipulating ability of robot arms in positioning and orienting end-effectors [19]. It is mainly researched on redundant manipulators and multi-fingered robot systems [20, 21]. The quality of the master arm design has a considerable influence on the maneuverability of master-slave systems [22]. This dissertation assumes

that there is no constraint from manipulability to focus on basic researches for haptics.

1.1.3 Application to Network System

Network technologies are rapidly developing. These technologies are applied to factory communications, broadcastings, internets and so on. Audiovisual communications are at the core of multimedia systems that allow users to interact across distances. It is common understanding that both audio and video are required for high-quality interaction. While audiovisual information provides users with satisfactory impressions of being present in remote environment, physical interactions and manipulations are not supported. True immersion into distant environment and efficient distributed collaborations require the ability to physically interact with remote objects and to literally get in touch with other people. Thus, haptics is expected to be applied to network systems [23].

However, network systems cause the problems of communication constraints such as delay for packet transmission, latency for packet processing, throughput limitation, and so on. These communication constraints often causes time delay [24]. In real network systems, time delay is caused from various layers and various processing. Unfortunately, this time delay makes the control system for haptics such as bilateral teleoperation systems unstable [25].

This dissertation tackles the time delay problems to control systems for applying haptics to network systems. Here, network systems are assumed to be delayed communication systems.

1.2 Orientation of Research

This research aims to establish fundamental technologies of motion control for haptics as shown in Fig. 1-2. There are three players in haptics, human, environment and robots. Then, robots have to analyze haptic data from human and environment. Robots have to play as haptic display to human. Network communications of each robot should be considered to construct haptic networks. Thus, fundamental technologies of haptics are composed of haptic data analysis, haptic display and communication. Thus, main research topics mentioned in this dissertation are described as follows.

- Haptic data analysis technology
- Haptic display technology
- Communication technology

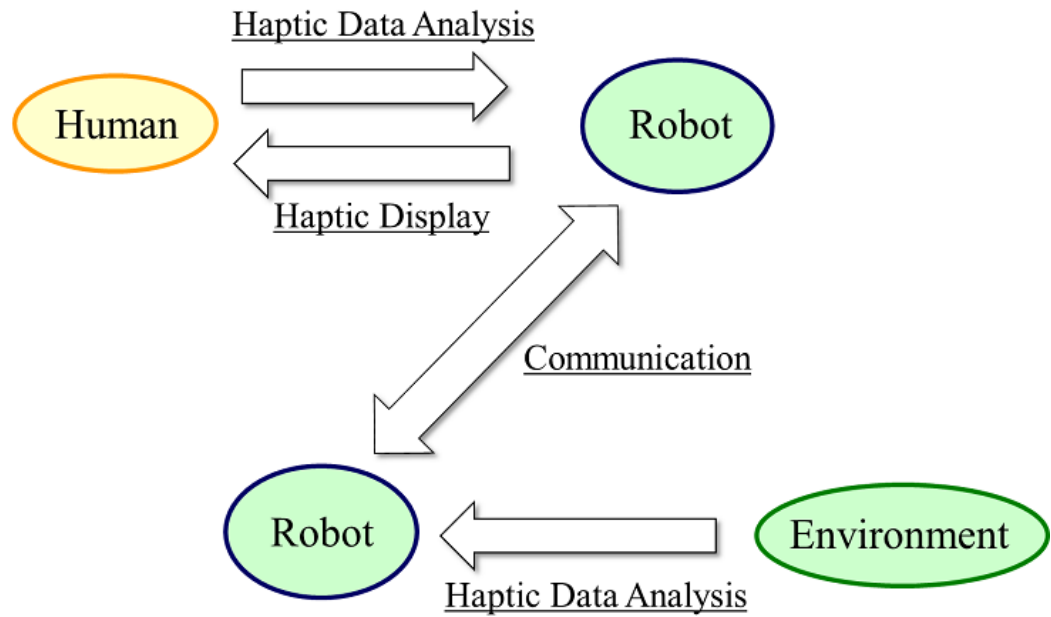


Fig. 1-2: Fundamental technologies of motion control for haptics.

Haptic data analysis technology is to sense and analyze haptic data. This includes how to sense environmental impedances and human motions. Haptic data analysis is important to abstract core components of haptic data.

Haptic display technology is to replay haptic data to human beings. Control systems have to be constructed considering characteristics of human tactile receptors.

Here, robot hands play a role of haptic analyzer and display. Robot hand mechanisms are common technologies for haptic data analysis and haptic display.

Communication technology includes time delay compensation for motion control systems with delayed communication systems. Communication technology is a key part to expand the utility of haptics.

1.3 Chapter Organization

The chapter organization is described in Fig. 1-3. The following chapter mentions general motion control techniques based on the acceleration control.

Chapter 3 to Chapter 5 focuses on haptic data analysis and haptic display technologies as basic researches of motion control for haptics. Chapter 3 proposes the flexible actuator as robot hand mecha-

CHAPTER 1 INTRODUCTION

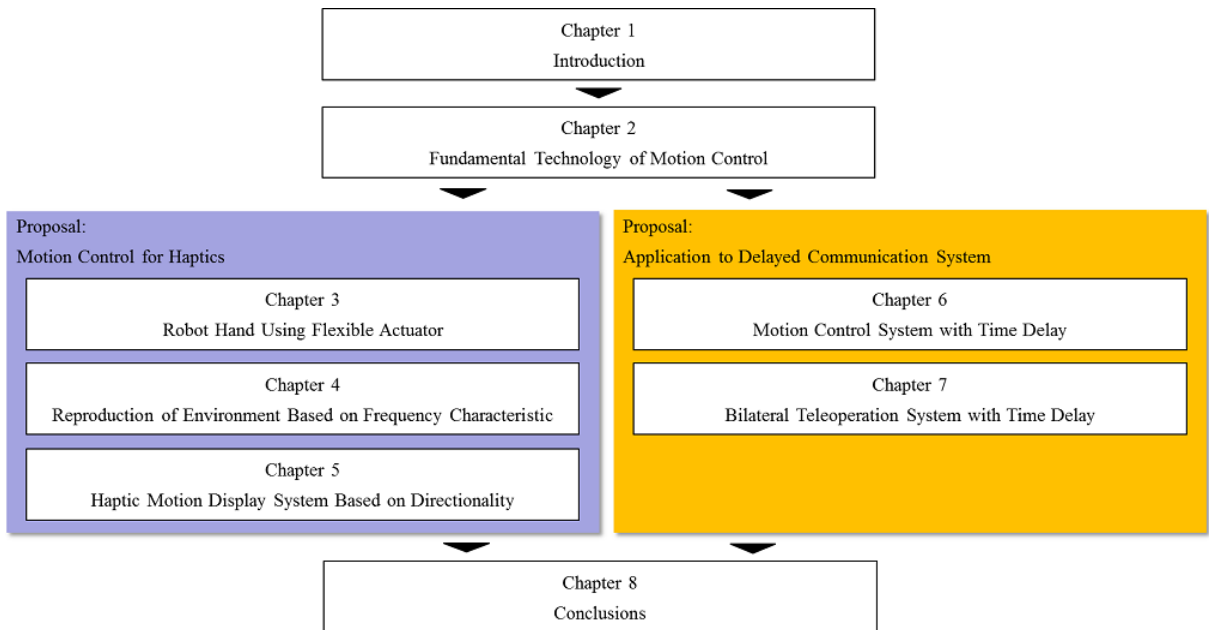


Fig. 1-3: Chapter organization.

nisms for haptics. The position and the force transfer characteristics of the flexible actuator have been verified. It is shown the flexible actuator is considered to be valuable for robot hand mechanisms for haptics. Moreover, as one of the application of the flexible actuator, the experimental results of the bilateral teleoperation system with the flexible actuator are shown. Chapter 4 focuses on haptic data analysis and display for environmental impedances. A method for abstraction of environment based on frequency characteristics has been proposed. The force response and the position response of environment are transformed from time domain to frequency domain. Then, frequency characteristics of environment are abstracted. A method for reproduction of environment using finite impulse response (FIR) filter is also proposed. Desired frequency characteristics are approximated by using FIR filter. This method is valuable for abstraction and reproduction of real environment based on frequency characteristics. Chapter 5 focuses on haptic data analysis and display for the human motions. This chapter defines human action mode and environmental action mode. A measured haptic motion is divided to each human action and environmental action by human action mode and environmental action mode. Furthermore, two types of haptic motion display systems are designed. One is based on human action mode. The other is based on human action mode and environmental action mode.

Chapter 6 and Chapter 7 focuses on communication technology for applying haptics to delayed communication systems. Chapter 6 studies the time delay effect to motion control systems. This chapter proposed the control system which is robust to unstable time delay. This chapter modifies the structure of the time delayed control system with communication disturbance observer (CDOB) considering unstable time delay. As the nonlinear effect like communication packet dropouts or jitter can deteriorate the total control system with integrators, a case study has been accomplished considering allocations of the system model in CDOB. Then, the more robust CDOB structure against packet dropouts and jitter is designed. Chapter 7 proposes the bilateral teleoperation system for delayed communication systems. Firstly, model-free time delay compensator is proposed. The proposed control system does not utilize the time delay model and the plant model, but the position control and the force control of the bilateral control system are stabilized. A bilateral teleoperation system to synchronize haptic and visual sense is also proposed. Moreover, allocations of high pass filter (HPF) are studied to attain the almost same performance with systems which do not include time delay. By allocating HPF correctly, the performance is improved with keeping the stability.

Finally, this thesis is summarized and concluded in Chapter 8. Contributions of this thesis and overall discussions of technologies about haptic data analysis, haptic display and communication are mentioned.

The related studies are explained in the introduction section of each chapter. The precise motivation of each topic is also described in the section.

Chapter 2

Fundamental Technology of Motion Control

This chapter describes the fundamental technology of motion control. Since the acceleration is the primary state in the motion, the acceleration control is utilized as the fundamental technology of motion control. 2.1 explains about basic technologies of the acceleration control. 2.2 describes the position, the force and the compliance control systems. 2.3 shows the control system based on a virtual space. Finally, this chapter is summarized in section 2.4.

2.1 Motion Control Based on Acceleration Control

Motion control is a technology for realizing various motions from integrated electrical and mechanical systems [26]. In this thesis, robots are utilized as integrated electrical and mechanical systems. The output of motion control is the position and the force. By increasing the control performance of the position and the force, the quality of the motion increases.

Since the acceleration is the primary state in the motion, the acceleration control is utilized as the fundamental technology of motion control. The position is derived from the double integration of the acceleration and the force is derived from the multiplication of the inertia. Thus, the position and the force are controlled by the acceleration control. Figure 2-1 shows the motion control system based on the acceleration control.

A motion control system is composed of a robot system, an acceleration controller and an acceleration reference generator. The acceleration reference generator generates the acceleration reference for realiz-

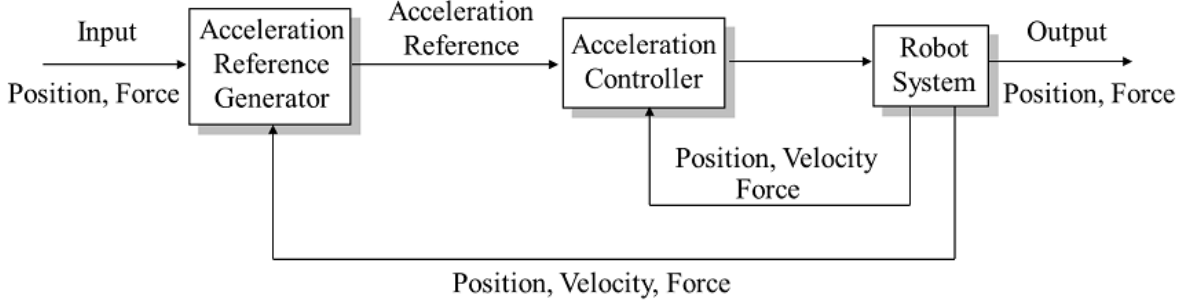


Fig. 2-1: Motion control system based on acceleration control.

ing the targeted position and force in the outer loop. The acceleration controller controls the acceleration of the robot system in the inner loop. The position and the force are outputted from the robot system.

2.1.1 Disturbance Observer

In the actual robot motion control, the disturbance force f^{dis} and the external force f^{ext} as well as the reference force f^{ref} are added to the robot. The disturbance force f^{dis} includes the external force f^{ext} , the frictional force f^{fric} and the force caused by the parametric fluctuation of the robot mass M and the thrust coefficient K_t as shown in (2.1).

$$f^{dis} = f^{ext} + (M - M_n)\ddot{x}^{res} + (K_{tn} - K_t) i_a^{ref}. \quad (2.1)$$

Hear, n means a nominal value.

Figure 2-2 shows the block diagram of disturbance observer (DOB) [26]. In Fig.2-2, \ddot{x}^{ref} , i^{cmp} and i_a^{ref} are the acceleration reference, the compensation current for the motor and the current reference for the motor. The disturbance force f^{dis} in (2.2) is estimated through low pass filter (LPF) as shown in (2.2). g_d is cut-off frequency of LPF.

$$\hat{f}^{dis} = \frac{g_d}{s + g_d} f^{dis}. \quad (2.2)$$

From (2.2), a robot system which is shown in Fig. 2-2 is equivalently transformed to Fig. 2-3. Figure 2-3 shows that the disturbance fore f^{dis} is transmitted to a robot system through HPF. If the cut-off frequency of HPF g_d is large enough, the disturbance force f^d hardly affects the system. The bandwidth for the acceleration control is decided from the cut-off frequency of HPF g_d .

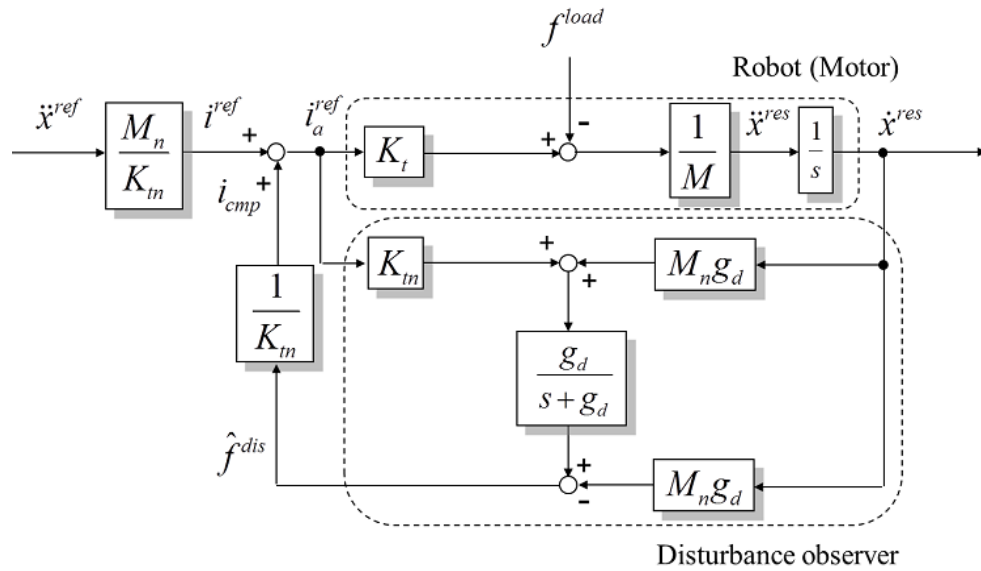


Fig. 2-2: Acceleration control based on DOB.

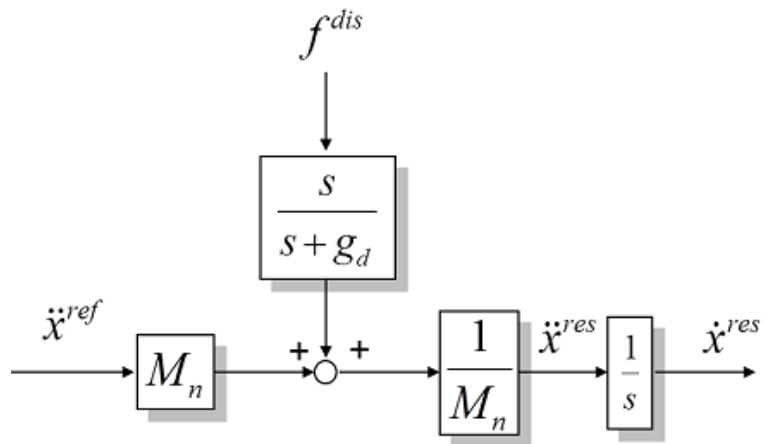


Fig. 2-3: Equivalent system of Fig. 2-2.

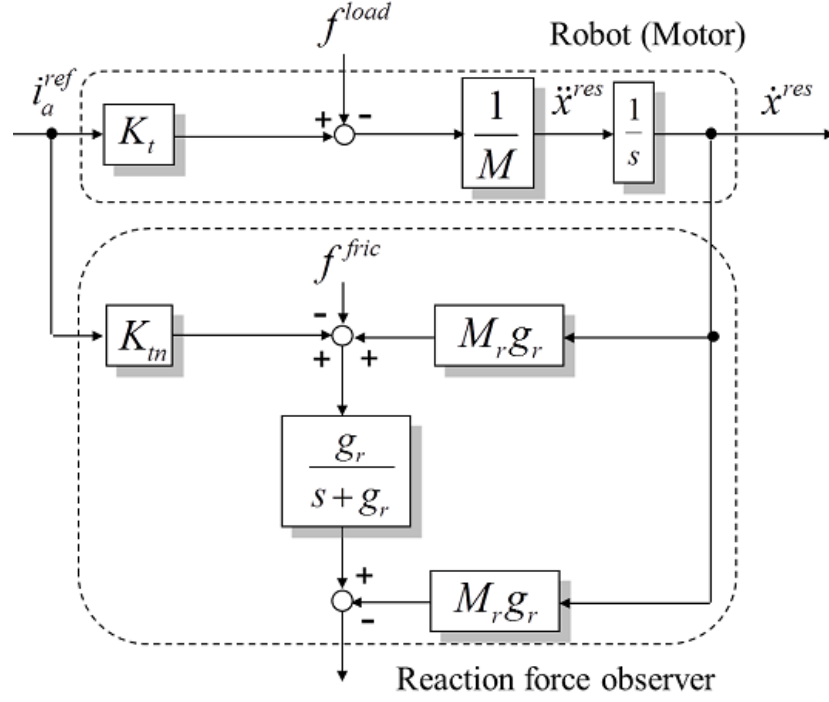


Fig. 2-4: Reaction force observer.

2.1.2 Reaction Force Observer

DOB is utilized as a force estimator by identifying the frictional force f^{fric} , the robot mass M and the thrust coefficient K_t . This observer is called reaction force observer (RFOB) [27]. Figure 2-4 shows the block diagram of RFOB. M_r is the identified mass and g_r is the cut-off frequency of LPF of RFOB. f^{ext} is estimated through LPF as shown in (2.3).

$$\hat{f}^{ext} = \frac{g_r}{s + g_r} f^{ext}. \quad (2.3)$$

Here, the bandwidth of the reaction force estimation is decided from g_r .

2.2 Control System

The output of motion control is the position and the force as explained in 2.1. For realizing various motions, the position and the force should be controlled ideally.

Table 2.1: Control stiffness

Target of control	Control stiffness
Position	∞
Compliance	Finite values
Force	0

However, the position control and the force control cannot be achieved simultaneously. If the position control is achieved completely, the force is indeterminate. If the force control is achieved completely, the position is indeterminate. This fact is represented by an index called control stiffness [26].

$$\frac{\partial f}{\partial x} = \kappa, \tag{2.4}$$

where x and f denote the position of a robot and the force exerted on a robot. Table 2.1 shows a relation between a target of motion and a required control stiffness. The ideal position control is achieved if κ is infinite, since ∂x approaches zero at infinite time. On the other hand, the ideal force control is achieved if κ is zero, since ∂f approaches zero at infinite time. The compliance control is represented as a combination of the position control and the force control.

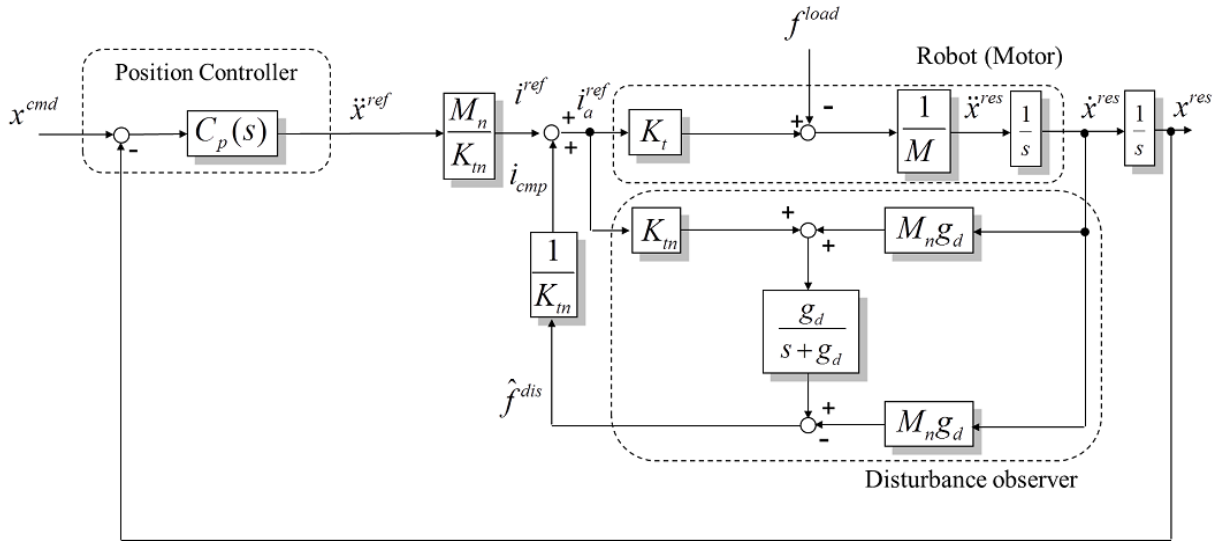


Fig. 2-5: Position control system.

2.2.1 Position Control

Figure 2-5 shows the position control system [26]. C_p is a position controller and x^{cmd} denotes the position command. In this dissertation, the position controller $C_p(s)$ denotes PD controller as (2.5)

$$C_p(s) = K_p + K_v s. \quad (2.5)$$

K_p is a position feedback gain and K_v is a velocity feedback gain.

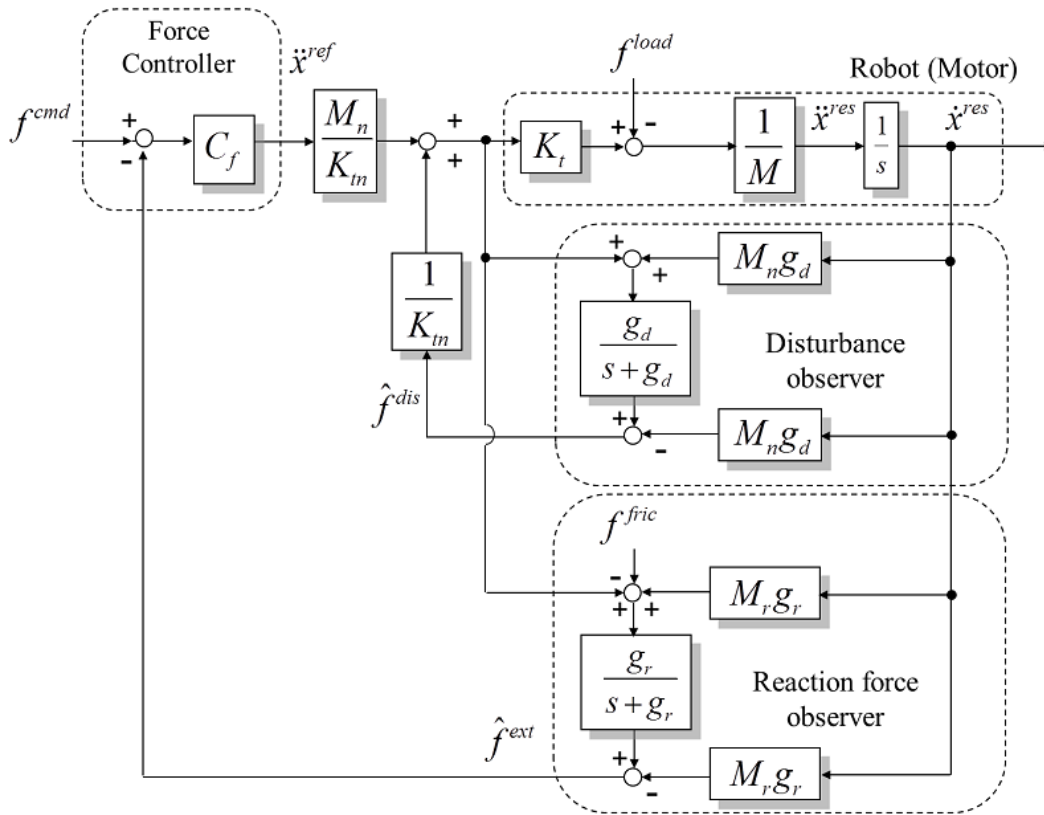


Fig. 2-6: Force control system.

2.2.2 Force Control

Figure 2-6 shows the force control system [28]. C_f is a force controller and f^{cmd} denotes the force command. In this dissertation, the force controller C_f denotes P controller as (2.6)

$$C_f = K_f. \quad (2.6)$$

K_f is a force feedback gain. PD control can be achieved in the force control system. However, P control is adopted here, since force information has some noise and the derivatives of the force are very noisy.

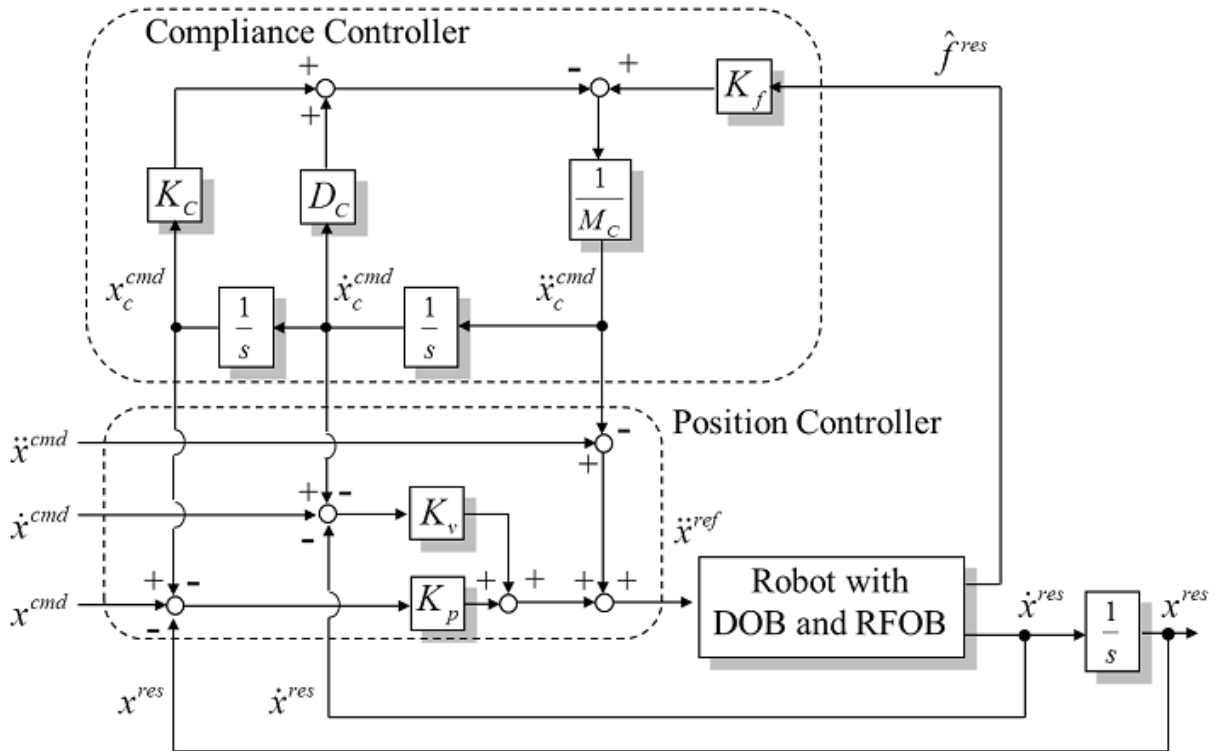


Fig. 2-7: Compliance control system based on position control.

2.2.3 Compliance Control

Figure 2-7 shows the position based compliance control system [29]. x_c^{cmd} , \dot{x}_c^{cmd} and \ddot{x}_c^{cmd} are the virtual position response, the virtual velocity response and the virtual acceleration response, respectively. The compliance from the external force is set from a force feedback gain K_f , a virtual mass M_c , a virtual damping D_c and a virtual stiffness K_c . If $\ddot{x}^{ref} = \ddot{x}^{res}$ is realized in Fig. 2-7, (2.7) is achieved.

$$x^{res} = x^{cmd} - \frac{K_f}{M_c s^2 + D_c s + K_c} \hat{f}^{res}. \quad (2.7)$$

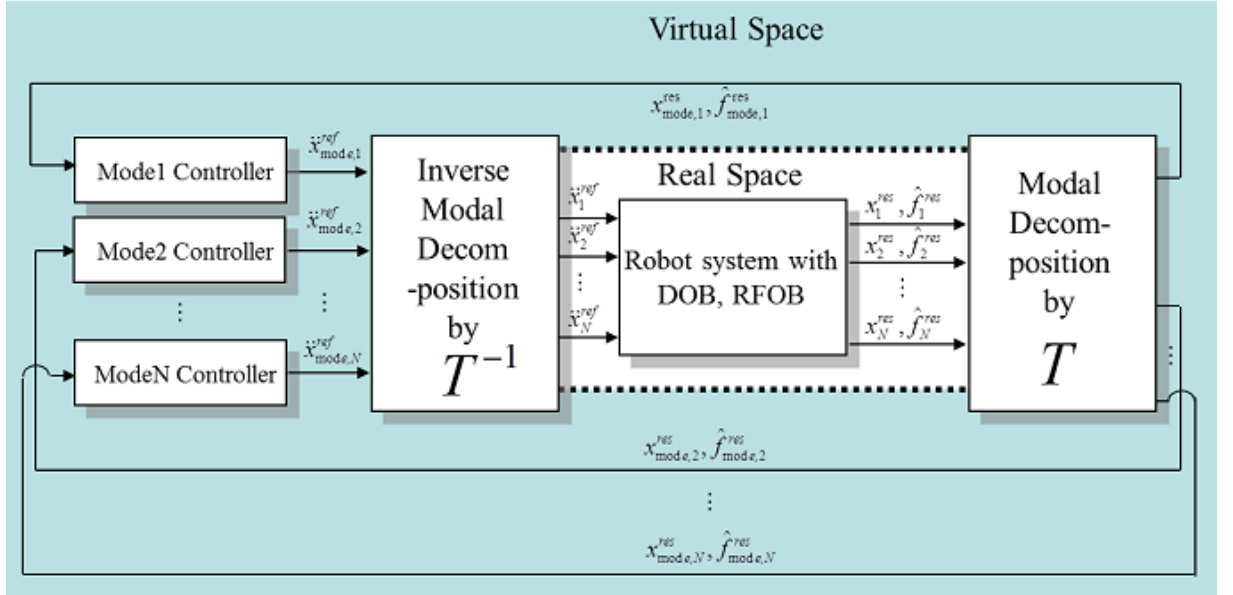


Fig. 2-8: Control system based on virtual space.

2.3 Control System Based on Virtual Space

A control space for multi degree of freedom robots can be constructed in a virtual space [30]. A virtual space does not depend on a real space but on the target of motion. Thus, by designing the virtual space, various kinds of motion are realized in multi degree of freedom robots.

2.3.1 Virtual Space

A control system based on a virtual space for N degree of freedom robots are shown in Fig. 2-8. Each robot is implemented with DOB and RFOB. The position and the force response of each robot in a real space are transformed to a virtual space by a modal transforming matrix $T \in \mathfrak{R}^{N \times N}$. Modes are corresponding to the state variables in the virtual space.

Controllers in the virtual space generate acceleration references. These values are transformed to the real space by a inverse transforming matrix $T^{-1} \in \mathfrak{R}^{N \times N}$.

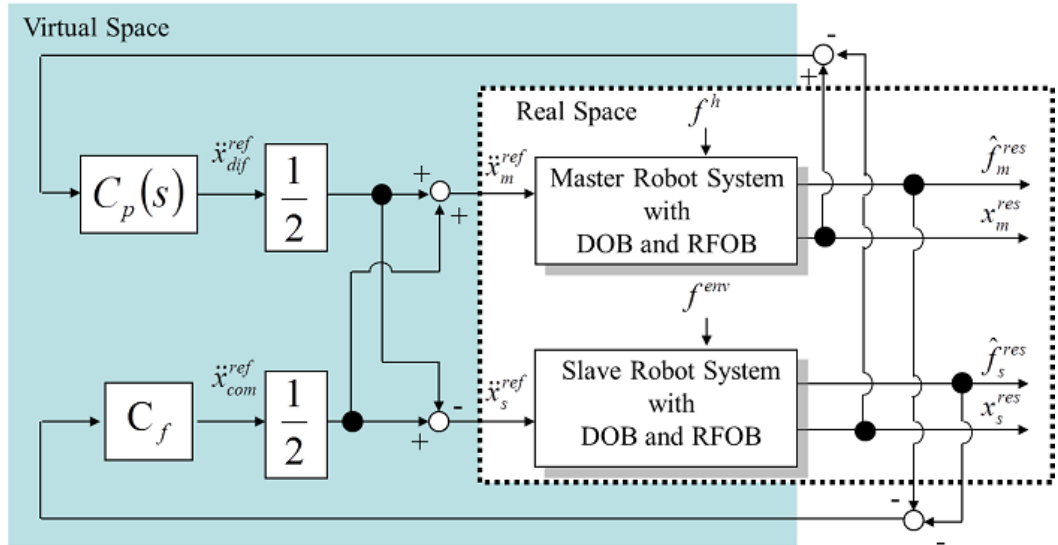


Fig. 2-9: Bilateral control system based on common mode and differential mode.

2.3.2 Bilateral Control Based on Differential Mode and Common Mode

A bilateral control system is an example of a control system based on a virtual space [31]. A bilateral control is a control system for the teleoperation system which is composed of a master robot and a slave robot. A human operator manipulates a master robot and a slave robot contacts with environment.

The bilateral control system has two objectives. One is the position tracking between the master robot and the slave robot. The other is realization of the law of action and reaction between the master robot and the slave robot.

The bilateral control system based on the differential mode and the common mode attains those objectives. Figure 2-9 shows the control system. Here, x_m^{res} , x_s^{res} , f_m^{res} and f_s^{res} are the position response of the master robot, the position response of the slave robot, the force response of the master robot and the force response of the slave robot, respectively. $C_p(s) = K_p + K_v s$ is a position controller and $C_f = K_f$ is a force controller. DOB and RFOB are implemented to the master robot and the slave robot.

In Fig. 2-9, the force controller is implemented to the common mode and the position controller is implemented to the differential mode. The force in the common mode (f_{com}) and the position in the

differential mode (x_{dif}) are defined in (2.8)–(2.9).

$$f_{com} = f_m + f_s, \quad (2.8)$$

$$x_{dif} = x_m - x_s. \quad (2.9)$$

The acceleration references of the common mode and the differential mode are set in (2.10)–(2.11).

$$\ddot{x}_{com}^{ref} = C_f \left(f_{com}^{cmd} - f_{com}^{res} \right), \quad (2.10)$$

$$\ddot{x}_{dif}^{ref} = C_p(s) \left(x_{dif}^{cmd} - x_{dif}^{res} \right). \quad (2.11)$$

The position tracking and the law of action and reaction between the master robot and the slave robot are realized by setting x_{dif}^{cmd} to 0 and f_{com}^{cmd} to 0.

Acceleration references in the virtual space (2.10)–(2.11) are transformed to the real space as shown in (2.12)–(2.13).

$$\ddot{x}_m^{ref} = \frac{1}{2}\ddot{x}_{com}^{ref} + \frac{1}{2}\ddot{x}_{dif}^{ref}, \quad (2.12)$$

$$\ddot{x}_s^{ref} = \frac{1}{2}\ddot{x}_{com}^{ref} - \frac{1}{2}\ddot{x}_{dif}^{ref}. \quad (2.13)$$

2.4 Summary

In this chapter fundamental technologies of motion control are described. The acceleration control system is introduced. Then, DOB for realizing the robust acceleration control system is explained. After that, each control system is shown. Finally, control systems based on virtual spaces are shown for multi degree of freedom robots.

Chapter 3

Robot Hand Using Flexible Actuator

3.1 Background and Outline

Robot hands have been utilized as mechanical interfaces in haptics [32, 33]. For abstraction and reproduction of haptic information, robot hands are utilized as recorders and displays [34].

For transmitting the position and the force from actuators to fingertips of robot hands, wire mechanisms have been researched [35–40]. The merit of wire mechanisms is a flexibility of the allocation of actuators and fingertips of robot hands. On the other hand, the demerit of wire mechanisms is that it does not transmit the position and the force from actuators to fingertips of robot hands accurately from frictions of pulleys. The transmittable frequency bandwidth is low from its flexibility. In addition, the pulling motion is capable but the pushing motion is incapable.

Robot hands which integrate small motors have been developed [41–43]. By integrating small motors, the size of robot hands can be reduced to same with human hands. Moreover, the degree of freedom is same with human hands. But, by using small motors, the force caused from the robot hand is limited. The other way for connecting actuators to fingertips of robot hands is rod mechanisms. Rod mechanisms are utilized in forceps robots [44]. The advantage of rod mechanisms is precise transfer characteristics of the position and the force. However, the disadvantage of rod mechanisms is that it restricts the allocation of actuators and fingertips of robot hands. For increasing the degree of freedom, the mass of the robot hand will increase.

Thus, the thrust wire mechanism has been developed for flexibly allocating actuators and fingertips of robot hands [45, 46]. The thrust wire enables not only the pull motion but also the push motion. The

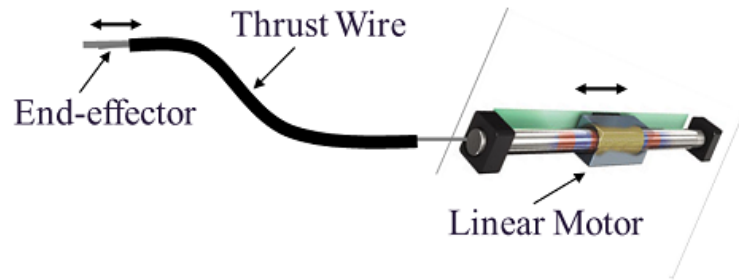


Fig. 3-1: Flexible actuator.

thrust wire transmits the position and the force from linear motors to end-effectors, and this mechanism is called as the flexible actuator.

For applying the flexible actuator to bilateral teleoperation systems, the position and the force pass bands of the flexible actuator are needed to be wider than the bandwidth from 0 to 10 Hz. The bandwidth from 0 to 10 Hz is the bandwidth of the human manipulation [47]. For transmitting more vivid force sensation, the position and the force pass bands of the thrust wire are desired to be wider than the bandwidth from 0 Hz to 10 Hz. This is because high frequency forces up to 1 kHz are important for the human perception.

This chapter shows verification results for the position and the force transfer characteristics of the thrust wire. Section 3.2 explains the developed flexible actuator. Section 3.3 shows the verification result of the position and the force transmission characteristics. From the position and the force pass bands of the thrust wire, the flexible actuator is evaluated whether it can be applied to teleoperation systems. 3.4 shows the experimental results of the bilateral teleoperation system with the flexible actuator. Finally, this chapter is summarized in section 3.5.

3.2 Flexible Actuator

3.2.1 Outline of Flexible Actuator

Figur 3-1 shows the outline of the flexible actuator. The thrust wire transmits the position and the force from linear motors to end-effectors. The thrust wire is designed based on releases which are utilized as transmission mechanisms to press a shutter button of a camera from a remote place.

The flexible actuator is considered to be valid for robot hands for haptic systems. As usages of the

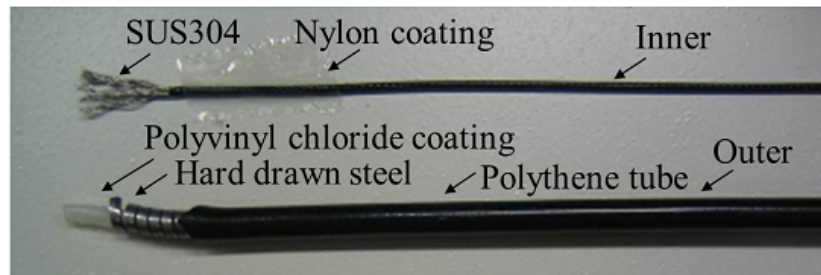


Fig. 3-2: Structure of thrust wire.

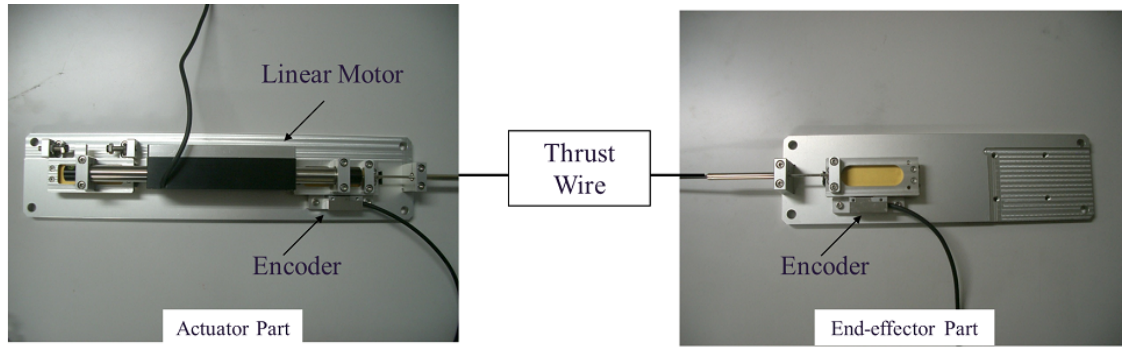
Table 3.1: Specifications of thrust wire

Inner wire	Length	1550.0	mm
	Diameter	$\phi 1.2$	mm
Outer tube	Length	1460.0	mm
	Outer diameter	$\phi 3.6$	mm
	Inner diameter	$\phi 1.3$	mm

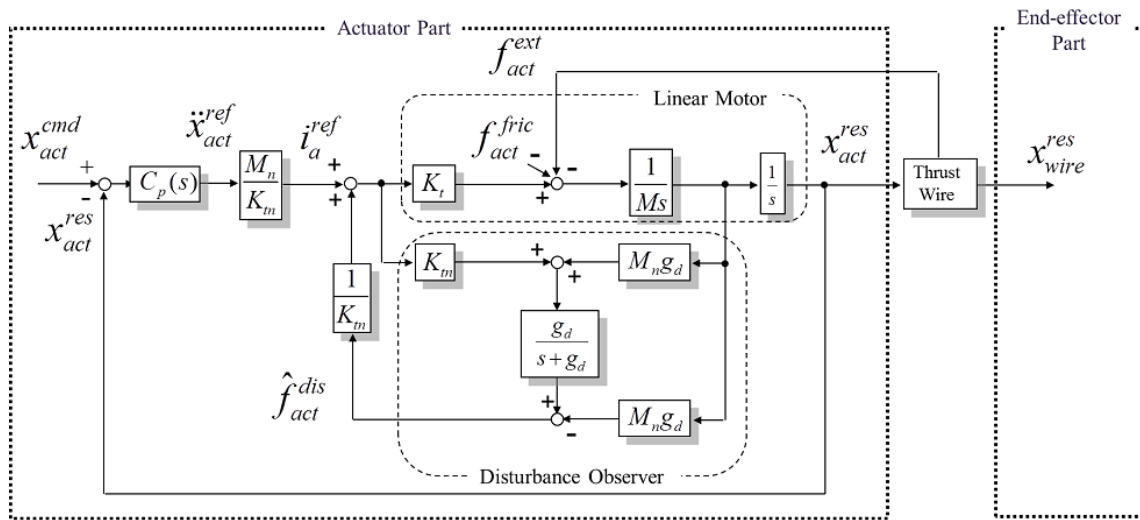
flexible actuator, telesurgeries, remote manipulations in atomic power plants and haptic communication systems are considered.

3.2.2 Thrust Wire

Figure 3-2 shows the structure of the thrust wire. Specifications of the thrust wire are shown in Table 3.1. The thrust wire is composed of the outer tube and the inner stranded wire. The inner wire is made of SUS304 which is coated by Nylon and Inner wire is stranded in order to strike a balance between rigidity and flexibility. On the other hand, the outer tube has three layer structures, which consist of the polyvinyl chloride coating, the hard drawn steel wire and the polythene tube. There is a little friction between the inner wire and the outer tube. This is because that the pair of the nylon coating and the polyvinyl chloride coating constrains the affection of frictions. The usage of the outer tube for the passage of the inner wire enables not only the pull motion but also the push motion.



(a) Experimental system



(b) Control system

Fig. 3-3: Verification system for position transfer characteristic.

3.3 Verification of Flexible Actuator

From the position and the force pass bands of the thrust wire, the flexible actuator is evaluated whether it is valuable to be applied to bilateral teleoperation systems.

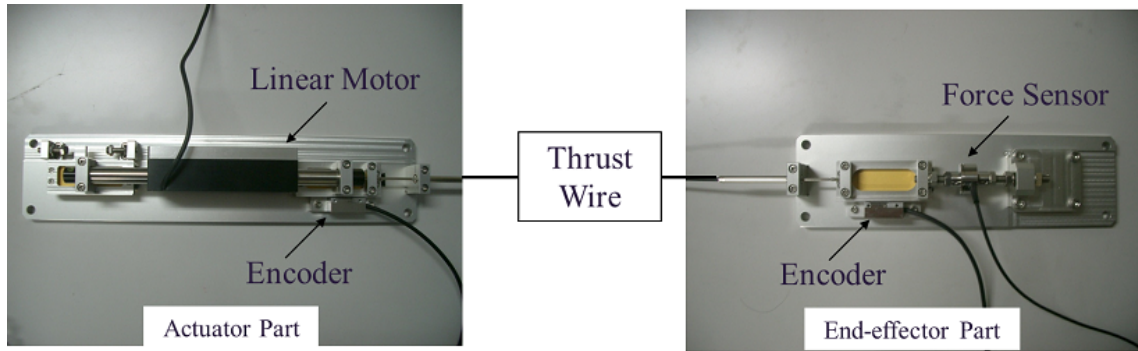
3.3.1 Verification System

Verification System for Position Transfer Characteristic

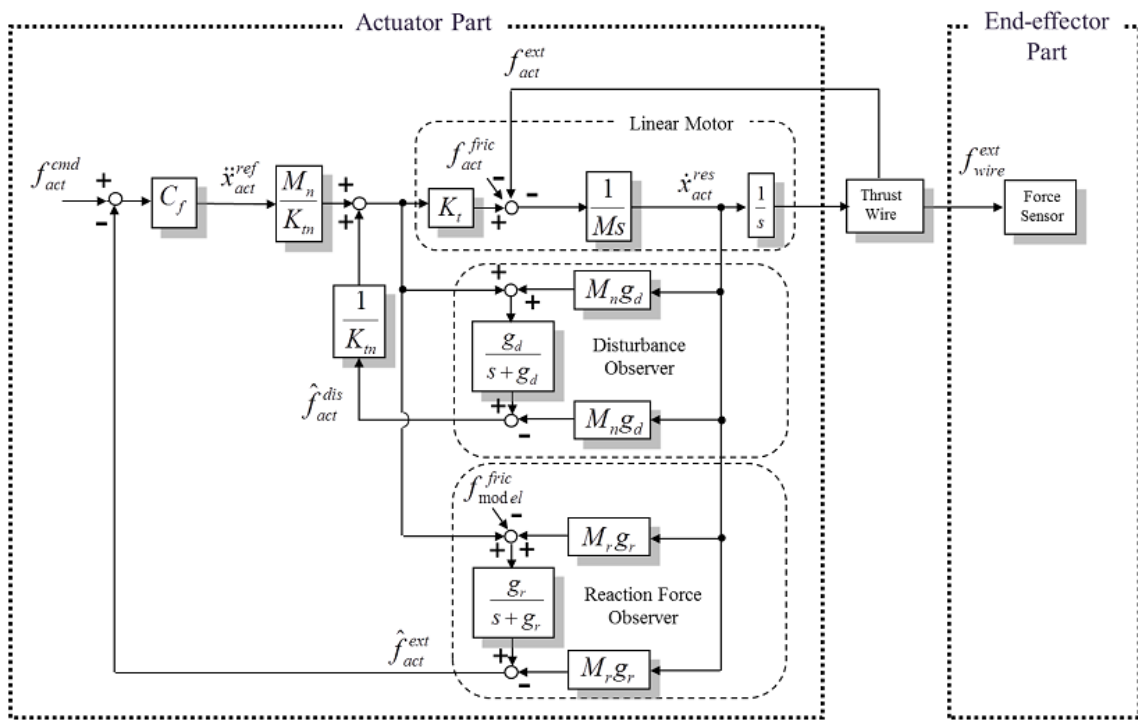
The verification system for the position transfer characteristic is shown in Fig. 3-3. As shown in Fig. 3-3 (a), the experimental system is composed of the actuator part and the end-effector part. In the

actuator part, a linear motor and a position encoder are equipped. The end-effector part has a position encoder.

The control system for the verification of the position transfer characteristic is shown in Fig. 3-3 (b). This control system is selected for realizing the position control in the wide bandwidth robustly. This kind of the robust control system is important for the motor which is equipped with the thrust wire. DOB is utilized for suppressing the disturbance [26]. g_d is a cut-off frequency of disturbance observer. x_{act}^{cmd} , x_{act}^{res} , \dot{x}_{act}^{res} and x_{wire}^{res} are the position command of the linear motor, the position response of the linear motor, the velocity response of the linear motor and the position response of the thrust wire, respectively. The acceleration reference \ddot{x}_{act}^{ref} is utilized for realizing the position command x_{act}^{cmd} and the velocity command \dot{x}_{act}^{cmd} . i_a^{ref} is the current reference, f_{act}^{ext} is the external force from the thrust wire and f_{act}^{fric} is the frictional force of the linear motor. M and K_t are the mass and the force coefficient of the linear motor. Note that the subscript n means the nominal value. $C_p = K_p + sK_v$ is a position controller. K_p is a proportional gain, and K_v is a derivative gain.



(a) Experimental system



(b) Control system

Fig. 3-4: Verification system for force transfer characteristic.

Verification System for Force Transfer Characteristic

The verification system for the force transfer characteristic is shown in Fig. 3-4. As shown in Fig. 3-4 (a), this experimental system is also composed of the actuator part and the end-effector part. In the actuator part, a linear motor and a position encoder are equipped. The end-effector part has a position encoder and a force sensor. This force sensor is fixed to the base plate.

The control system for the verification of the force transfer characteristic is shown in Fig. 3-4 (b). DOB is utilized for suppressing the disturbance and RFOB is utilized for estimating the external force to the linear motor [28]. g_r and M_r is a cut-off frequency and the model mass of RFOB. f_{act}^{cmd} , f_{act}^{ext} , f_{wire}^{ext} and f_{model}^{fric} are the force command of the linear motor, the external force to the linear motor, the external force to the thrust wire and the frictional force model of RFOB. The acceleration reference \ddot{x}_{act}^{ref} is utilized for realizing the force command f_{act}^{cmd} . The external force to the thrust wire is measured by the force sensor. $C_f = K_f$ is a force controller. K_f is a proportional gain for force controller.

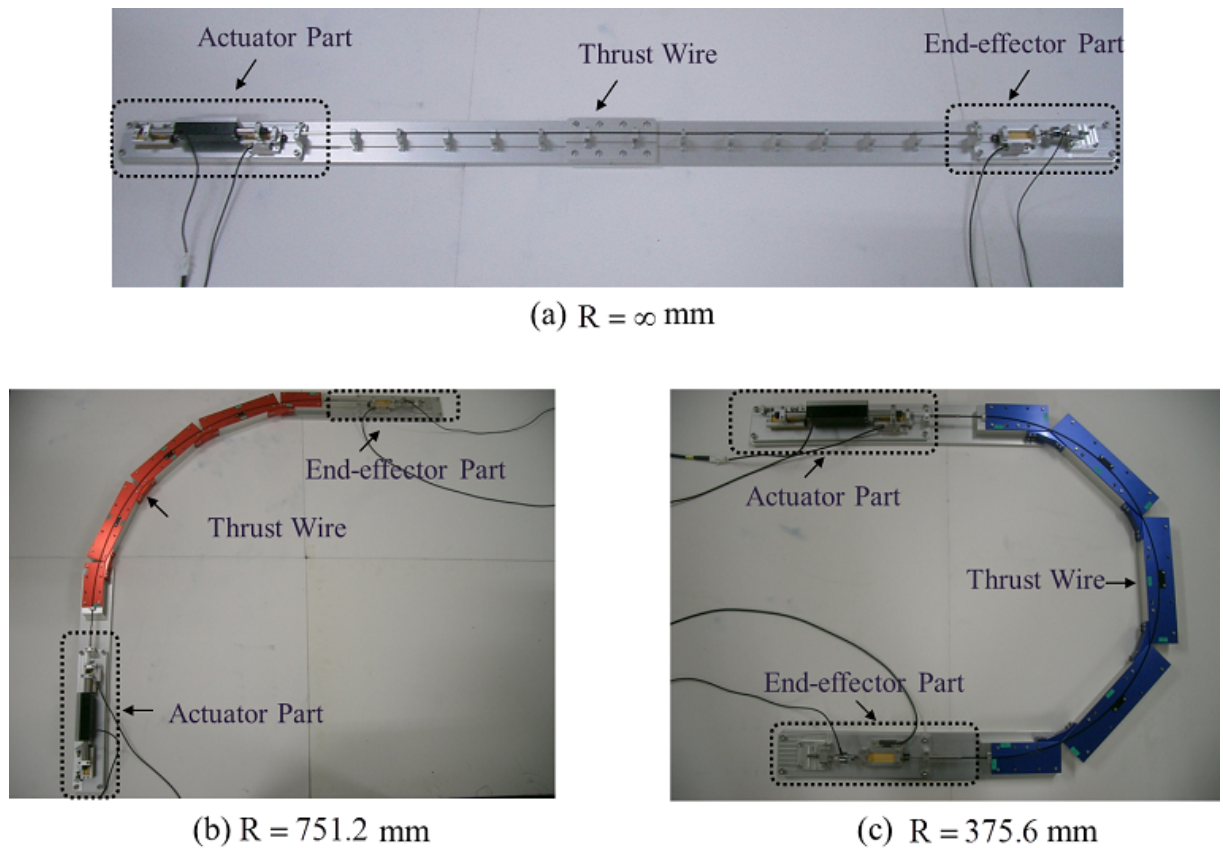


Fig. 3-5: Allocation of actuator part and end-effector part.

3.3.2 Verification Result

Experiments for verifications were conducted in 3 kinds of allocation of the thrust wire as shown in Fig. 3-5. In each case, the actuator part and the end-effector part are set straight line, bended 90 degree and bended 180 degree, respectively. Bend radiuses are ∞ mm, 751.2mm and 375.6mm, respectively. Table 3.2 shows control parameters for experiments for verifications. These parameters were decided from the performance of the verification systems. Since the position control and the force control were performed to the linear motor, the effect of the thrust wire was not considered. In the experiments for verifications, sinusoidal functions with various frequencies were added as the position command and the force command.

As a result, the position transfer characteristic is obtained as a Bode diagram of the transfer function

Table 3.2: Control parameters

Nominal mass	M_n	0.5	kg
Position feedback gain	K_p	1600	
Velocity feedback gain	K_v	80	
Force feedback gain	K_f	2	
Cut-off frequency of DOB, RFOB	g_d, g_r	500	rad/s

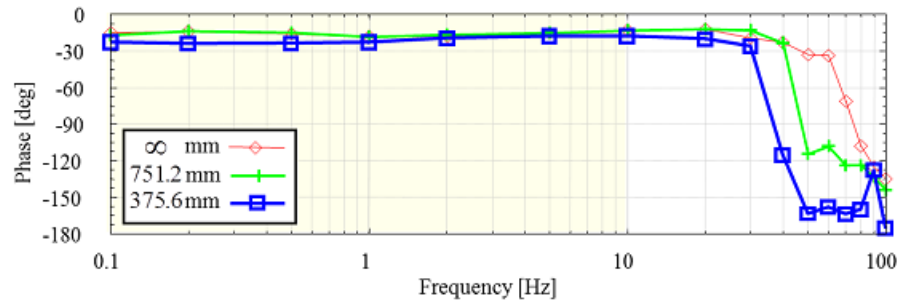
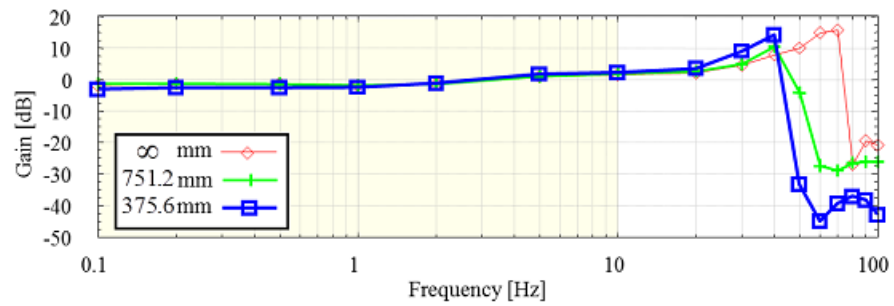


Fig. 3-6: Position transfer characteristic.

$\frac{x_{wire}^{res}}{x_{act}^{res}}$ as shown in Fig. 3-6. In addition, the force transfer characteristic is obtained as a Bode diagram of the transfer function $\frac{f_{wire}^{ext}}{f_{act}^{ext}}$ as shown in Fig. 3-7. In Fig. 3-6 and Fig. 3-7, the legend symbols ∞ mm, 751.2mm and 375.6mm are the experimental results when the bend radius is ∞ mm, 751.2mm and 375.6mm, respectively. Figures 3-6 (a) and 3-7 (a) show gain characteristics. Figures 3-6 (b) and 3-7 (b) show phase characteristics. In the ideal transfer characteristic, gain characteristics should be 0 dB, and phase characteristics should be 0 deg. Shaded areas show the bandwidth from 0.1 to 10 Hz. For applying the flexible actuator to bilateral teleoperation systems, the ideal transfer characteristic is needed

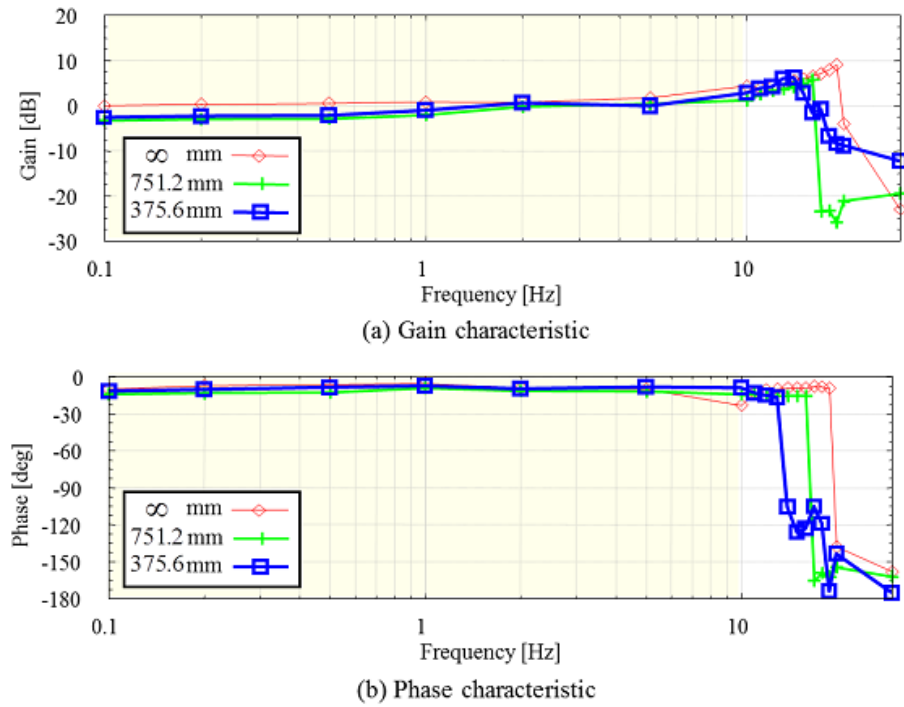


Fig. 3-7: Force transfer characteristic.

to be realized in shaded areas. The bandwidth from 0 to 10 Hz is the bandwidth of human manipulation.

From Fig. 3-6, the position pass band is decreasing when the bend radius becomes small from ∞ mm to 375.6mm. As gain characteristics are decreasing from 0 dB, phase characteristics are also decreasing. When the bend radius is decreased from ∞ mm to 375.6mm, the ideal transfer characteristic is almost realized from 0.1 to 40 Hz. From Fig. 3-7, when the bend radius decreased from ∞ mm to 375.6mm, gain characteristics of transfer function $\frac{f_{wire}^{ext}}{f_{act}^{ext}}$ decreases 3 dB at the 0.1 Hz – 2.0 Hz frequency bandwidth. This is because the frictional force of the thrust wire is increasing. The force pass band is decreasing when the bend radius becomes small from ∞ mm to 375.6mm. As gain characteristics are decreasing from 0 dB, phase characteristics are also decreasing. When the bend radius decreased from ∞ mm to 375.6mm, the ideal transfer characteristics are almost realized from 0.1 to 17 Hz.

It is shown that, when the bend radius becomes small from ∞ mm to 375.6mm., the ideal transfer characteristic is almost realized from 0.1 to 40 Hz in the position transmission and 0.1 to 17 Hz in the force transmission. Thus, the position and the force pass bands of the thrust wire are wider than 0.1 to 10 Hz. Therefore, the flexible actuator is considered to be valuable to be applied to teleoperation systems.

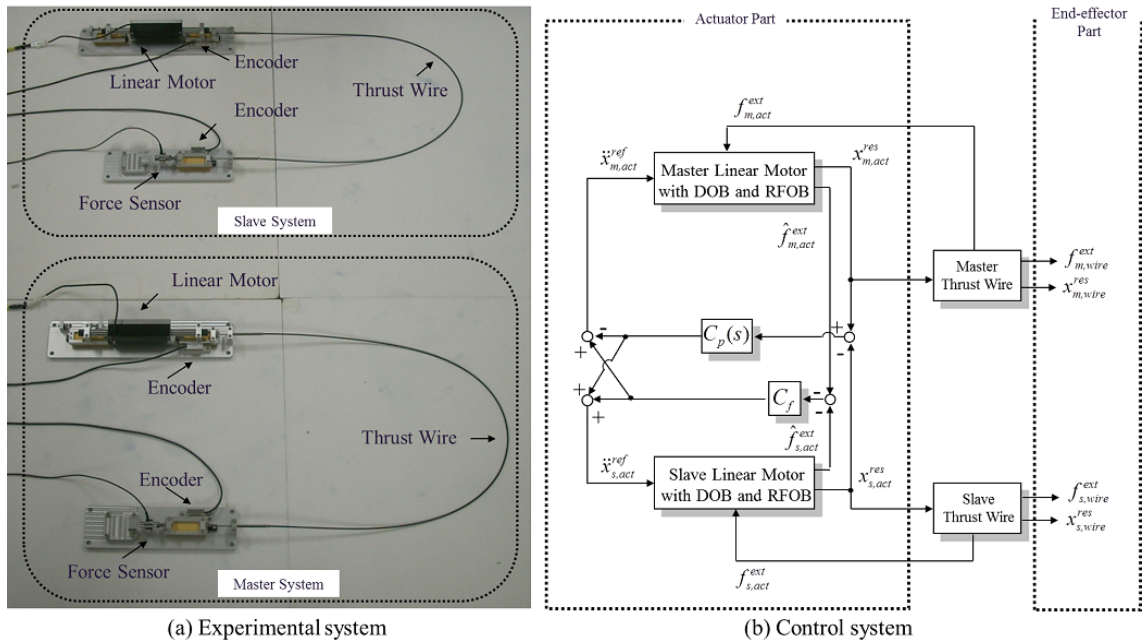


Fig. 3-8: A bilateral teleoperation system with flexible actuator.

3.4 Application to Bilateral Teleoperation System

For clarifying the effect of the flexible actuator, the bilateral teleoperation system with the flexible actuator which does not include communication channel is utilized. Then, the position and the force pass bands of the bilateral teleoperation system with the flexible actuator are verified.

3.4.1 Bilateral Teleoperation System with Flexible Actuator

Figure 3-8 shows the bilateral teleoperation system with the flexible actuator. The experimental system is shown in Fig. 3-8 (a). This bilateral teleoperation system is composed of a master system and a slave system. Each system has the actuator part and the end-effector part. From Fig. 3-8 (a), it is shown that the actuator part and the end-effector part are set flexibly by utilizing the flexible actuator. The actuator part has a position encoder and a linear motor. End-effector part is equipped with a position encoder and a force sensor. In this experiment, the force sensor is not fixed to the base plate. Human operator manipulates the master system of the end-effector part. The end-effector part of the slave system contacts environment.

The control system is shown in Fig. 3-8 (b). As an application to the bilateral teleoperation system, the bilateral control is performed between the linear motor of the master system and the linear motor of the slave system. 4-channel bilateral control is utilized as the bilateral control method [44]. DOB is utilized for suppressing the disturbance and RFOB is utilized for estimating the external force to the linear motor. This control system is selected for realizing the bilateral control between the master linear motor and the slave linear motor in the wide bandwidth robustly. This kind of robust control system is important for the motors which are equipped with the thrust wire. x_{act}^{res} , x_{wire}^{res} , f_{act}^{ext} , f_{wire}^{ext} and \ddot{x}_{act}^{ref} are the position response of the linear motor, the position response of the thrust wire, the external force to the linear motor, the external force to the thrust wire and the acceleration reference to the linear motor, respectively. The external force to the thrust wire is measured by the force sensor of the end-effector part. The subscript m means the master system and s means the slave system. $C_p = K_p + sK_v$ is a position controller, and $C_f = K_f$ is a force controller. For clarifying the effect from the flexible actuator, this bilateral control system does not include the communication channel. Thus, the master system and the slave system are controlled by one computer.

3.4.2 Experimental Result

In the experiments, two cases of experiments were conducted. One experiment was that the slave system contacted with a soft object which is sponge. The other experiment was that the slave system contacted with a hard object which is iron. Control parameters shown in Table 3.2 were utilized in this experiment. These parameters were decided from the performance of the experimental system. Since this bilateral control was performed to linear motors, the effect of the thrust wire was not considered. The experimental results in time domain were transformed to those in frequency domain by using discrete Fourier transform. The measurement time was 10 s, and the position and the force were measured at sampling frequency of 1 kHz.

Frequency spectra of the position and the force responses are shown in Fig. 3-9. The legend symbol master is the spectrum of the position response of the thrust wire $x_{m,wire}^{ext}$ or the external force to the thrust wire $f_{m,wire}^{ext}$ in the master system. The legend symbol slave is the spectrum of the position response of the thrust wire $x_{s,wire}^{res}$ or the external force to the thrust wire $f_{s,wire}^{res}$ in the slave system. The position response is measured by the position encoder of the end-effector part. The external force is measured by the force sensor of the end-effector part. In the ideal condition, the spectrum of the master system and the spectrum of the slave system are the same shape. Shaded areas show the bandwidth from 0 to 10 Hz. The

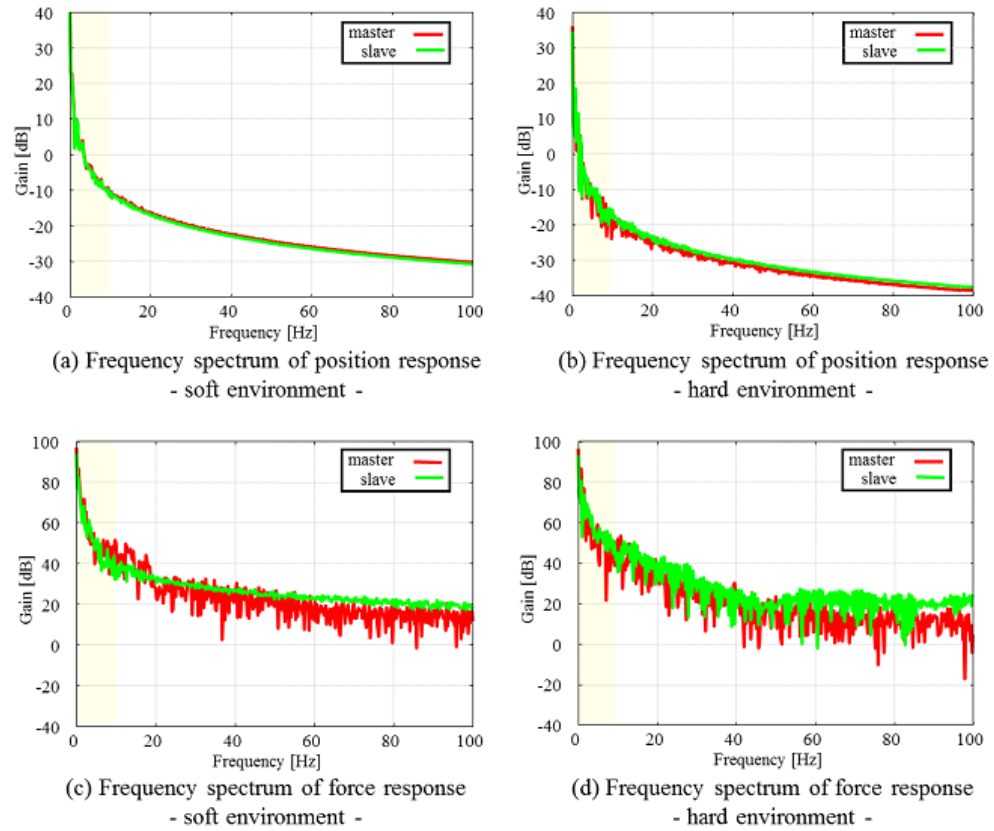


Fig. 3-9: Frequency spectra.

bandwidth from 0 to 10 Hz is the bandwidth of human manipulation. Thus, when the ideal condition is realized in this bandwidth, the human manipulation is transmitted by the bilateral teleoperation system. For the human perception, the ideal condition is desired to be realized more than the bandwidth of 0 to 10 Hz. From Fig. 3-9 (a) and Fig. 3-9 (b), two spectra of the position response are almost equal between the master and the slave system. In Fig. 3-9 (c) and Fig. 3-9 (d), it is shown that two spectra of the external force are also almost equal from the bandwidth of 0 to 20 Hz. At high frequency bandwidth, two spectra of external force are not equal.

Therefore, human manipulations are transmitted by the bilateral teleoperation system with the flexible actuator.

3.5 Summary

This chapter verified the position and the force transfer characteristics of the thrust wire. From the verification result, the flexible actuator was considered to be applied to teleoperation systems.. Moreover, as one of the application of the flexible actuator, the experimental results of the bilateral teleoperation system with the flexible actuator were shown. It was shown that the flexible actuator has the merits of both wire mechanisms and rod mechanisms when the flexible actuator was applied to the bilateral teleoperation system.

Chapter 4

Reproduction of Environment Based on Frequency Characteristic

4.1 Background and Outline

Some researches have been conducted for reproduction of ‘haptic information’ especially about virtual environment [48]. In the field of creating virtual environment, creating a virtual wall that behaves passively has been an active research area. The limiting factors for stably generating the stiffness has been analyzed by [49].

On the other hand, the way to abstract and reproduce ‘haptic information’ is also important for reproduction of real environment. An algorithm for estimating the non-linear environmental impedances is proposed by [50]. The force sensation recorder system which was able to abstract and reproduce from real environment was introduced [17]. They set environment as constructed with the stiffness and the damper which has the non-linear effect.

Frequency characteristics are not considered mainly in those methods. However, frequency characteristics are important in the field of auditory sensing and optical sensation. Human beings’ ear senses the sound which is Fourier transformed. Human beings’ eye senses the image based on the magnitude of red, green and blue [4]. Abstraction and processing of image information is conducted based on this characteristic [51]. In the field of haptics, frequency characteristics are important based on the structure of finger tactile receptors [5]. Human beings has two types of tactile receptors in the point of the response speed. One type feels the fast motion; the other type feels the slow motion. Therefore, frequency characteristics are important for ‘haptic information’.

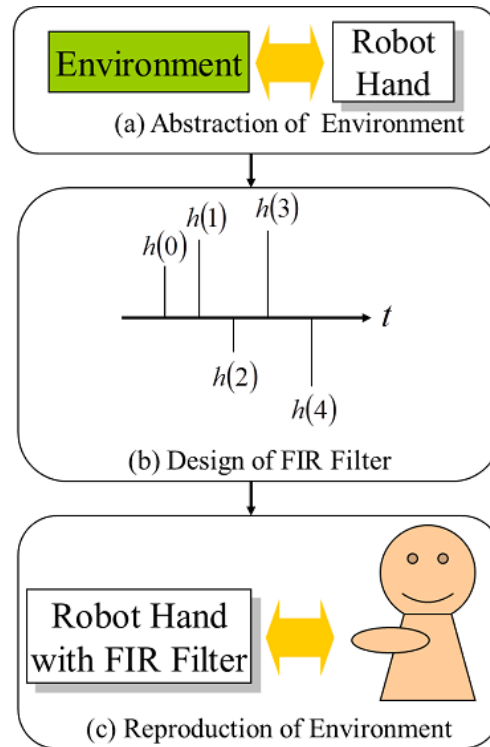


Fig. 4-1: The process of abstraction and reproduction of environment.

In this chapter, a method for abstraction and reproduction of environment based on frequency characteristics are explained. Figure 4-1 shows the process of abstraction and reproduction of environment. Firstly, the robot hand adds the force to environment as shown in Fig. 4-1(a). The force response and the position response of environment are transformed from time domain to frequency domain. Thus, the frequency characteristic of environment is abstracted. Secondly, FIR filter is designed to reproduce the frequency characteristic of environment as shown in Fig. 4-1(b). Finally, as shown in Fig. 4-1(c), FIR filter is implemented to the control system of the robot hand to reproduce environment.

The composition of this chapter is described as follows. An method for abstraction of environment based on frequency characteristics is shown in section 4.2. In section 4.3, a method for reproduction of environment using FIR filter is explained. The validity of the proposed methods are shown by experimental results in section 4.4. Finally, this chapter is summarized in section 4.5.

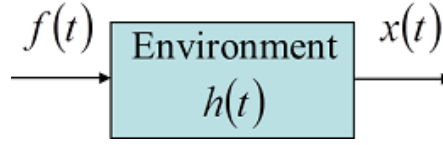


Fig. 4-2: Modeling of environment.

4.2 Abstraction of Environment Based on Frequency Characteristic

In this section, a method for abstraction of environment based on frequency characteristics is proposed. Firstly, environment is modeled. Then, the control system for abstraction of environment is designed.

4.2.1 Modeling of Environment

Environment is modeled as Fig. 4-2. This environment assumes that the input is the force $f(t)$, and that the output is the position $p(t)$. The impulse response of environment is supposed to $h(t)$. And, environment is approximated as linear and time invariant. Here, t means time [s].

Then, the transfer function from the force to the position of environment is calculated as (4.1)–(4.3).

$$\Phi_{ff} = F(\omega) F(-\omega), \quad (4.1)$$

$$\Phi_{xf} = X(\omega) F(-\omega), \quad (4.2)$$

$$H(\omega) = \frac{\Phi_{xf}(\omega)}{\Phi_{ff}(\omega)} = \frac{X(\omega)}{F(\omega)}, \quad (4.3)$$

where ω is the angular frequency, Φ_{ff} is the power spectrum of the force, Φ_{xf} is the cross spectrum of the position and the force. $F(\omega)$, $X(\omega)$ and $H(\omega)$ are the fourie transformed value of $f(t)$, $x(t)$ and $h(t)$. $H(\omega)$ is the transfer function of environment.

When environment is expressed with the constant stiffness k_e [N/m] and the damper d_e [(N×s)/m], the absolute value of the inverse transfer function $H(\omega)$ becomes as Fig. 4-3. As well as the constant stiffness and the damper, various kinds of frequency characteristics are expressed by utilizing the transfer function of environment.

4.2.2 Control System

The control system for abstraction of environment is shown in Fig. 4-4. DOB is utilized for the acceleration control. The force response is estimated by RFOB for sensing the wide band force response.

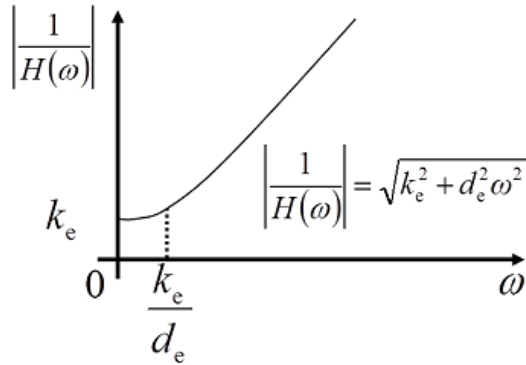


Fig. 4-3: Example of frequency characteristic of environment.

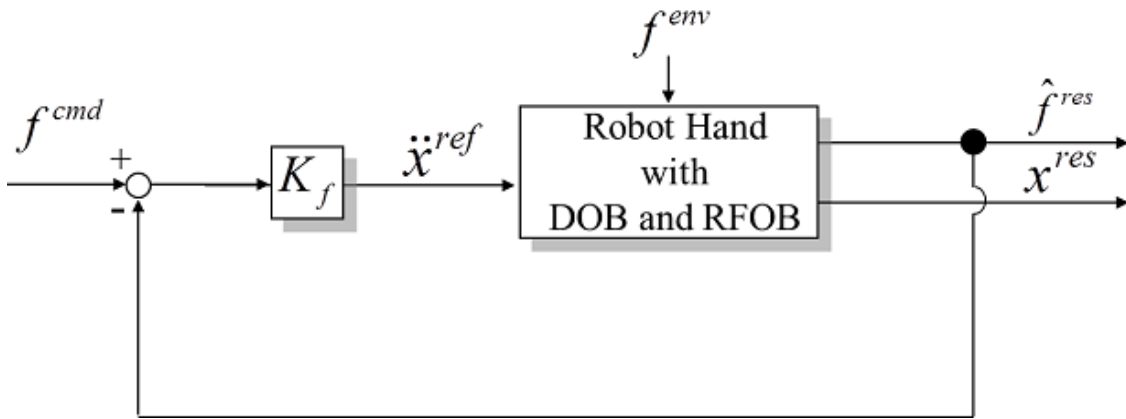


Fig. 4-4: Control system for abstraction of environment.

The force control is performed to the robot for adding the force to environment. K_f in Fig. 4-4 shows a feedback gain in the force control system.

4.3 Reproduction of Environment Using FIR Filter

In this section, a method for reproduction of environment using FIR filter is proposed. FIR filter is utilized for realizing desired frequency characteristics. Then, the control system for reproduction of environment is shown.

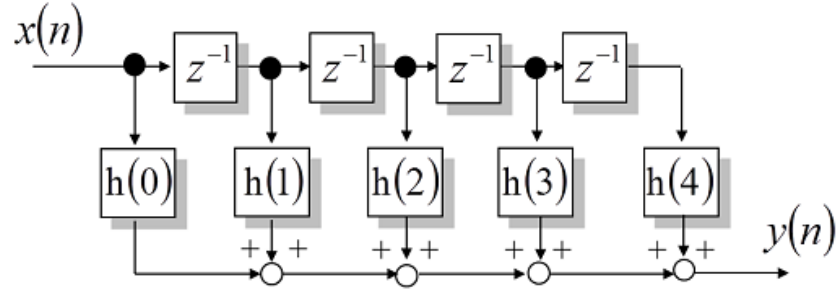


Fig. 4-5: 4th order FIR filter.

4.3.1 Design of FIR Filter for Reproduction of Environment

In this subsection, FIR Filter is introduced and the design method of FIR filter for reproducing the environmental frequency characteristics is explained. FIR filter is designed based on the frequency sampling method [52, 53]. Here, the window function is utilized to reduce the modeling error of the high frequency area.

FIR Filter

FIR filter is a type of a digital filter. It has a finite response to an impulse. 4th order FIR filter is expressed as Fig. 4-5. $x(n)$ is the input to the FIR filter, $y(n)$ is the output from FIR filter and z is the operator of Z transform. The output of FIR filter in Fig. 4-5 becomes as (4.4).

$$y(n) = \sum_{k=0}^4 h(k) x(n-k). \quad (4.4)$$

The desired finite impulse response can be set by designing $h(0)$ to $h(4)$, respectively. The transfer function of FIR filter $H(j\omega)$ is calculated as (4.5).

$$H(j\omega) = \sum_{k=0}^4 h(k) \exp(-jk\omega), \quad (4.5)$$

where ω is the angular frequency. From (4.5), it is shown that the transfer function of FIR filter is designed by tuning $h(0)$ to $h(4)$.

Frequency Sampling Method

This method composed of two steps. Step one is **1. sampling of desired frequency**. Step two is **2. inverse discrete transform to sampled value**.

1. Sampling of Desired Frequency

The abstracted environmental frequency characteristic $H^{ref}(\omega)$ is sampled every $\Delta\omega = \frac{2\pi}{NT}$ [rad/s]. N is a number of the sampled value. T_s is a sampling time of FIR filter. Then, the sampled value $H(k)$ ($k = 0, 1, \dots, N-1$) is derived as (4.6).

$$H(k) = H^{ref}\left(\frac{2\pi k}{NT_s}\right). \quad (4.6)$$

$(k = 0, 1, \dots, N-1)$

After that, the phase delay is added to the sample value $H(k)$ as shown in (4.7).

$$H'(k) = \begin{cases} H(k) \exp\left(-j\left(\frac{N-1}{2}\right)\frac{2\pi k}{N}\right), \\ \left(k = 0, \dots, \frac{N-1}{2}\right) \\ H(k) \exp\left(j\left(\frac{N-1}{2}\right)\frac{2\pi}{N}(N-k)\right), \\ \left(k = \frac{N-1}{2} + 1, \dots, N-1\right) \end{cases} \quad (4.7)$$

2. Inverse Discrete Transform to Sampled Value

N points Inverse Discrete Transform (IDFT) are conducted to $H'(k)$.

$$h(n) = \frac{1}{N} \sum_{k=0}^{N-1} H'(k) \exp\left(\frac{j2\pi kn}{N}\right). \quad (4.8)$$

$(n = 0, 1, \dots, N-1)$

$h(n)$ ($n = 0, 1, \dots, N-1$) becomes the finite impulse response of FIR filter.

Window Function

A window function $w(n)$ is multiplied to the calculated finite impulse response of FIR filter $h(n)$ ($n = 0, 1, \dots, N-1$).

$$h'(n) = h(n)w(n). \quad (4.9)$$

$(n = 0, 1, \dots, N-1)$

Blackman window which has a large dynamic range is utilized as the window function. The window function is utilized to reduce the modeling error of the high frequency area. By following above steps, the finite impulse response of FIR filter which reproduces the desired frequency characteristic is derived as shown in (4.9).

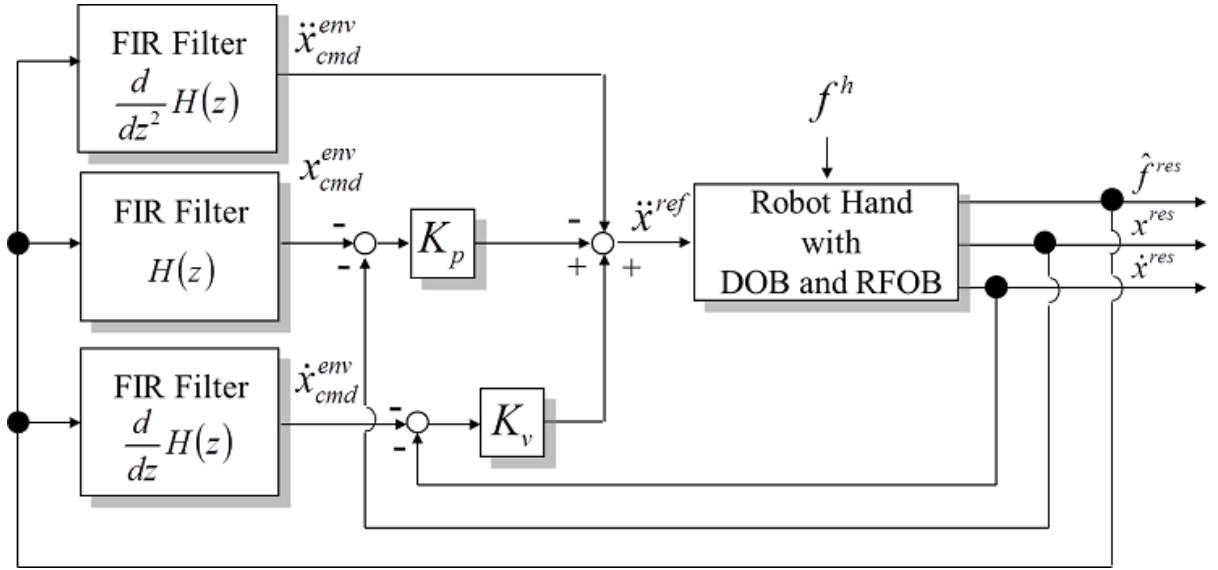


Fig. 4-6: Control system for reproduction of environment.

4.3.2 Control System

The control system for reproduction of environment is shown in Fig. 4-6. DOB and RFOB are implemented to the robot hand. FIR filter reproduces the environmental position command x_{res}^{env} depending on the human force input f^h to the robot hand. The position control is performed for tracking the reproduced environmental position command x_{cmd}^{env} . K_p and K_v in Fig. 4-6 show a position feedback gain and a velocity feedback gain in the position control system. By utilizing FIR filter, the desired environmental frequency characteristic is reproduced between the human force input f^h and the environmental position command x_{cmd}^{env} .

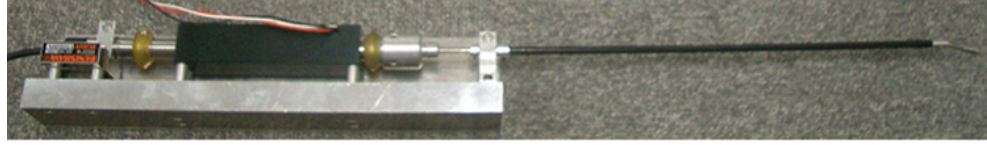
The control system in Fig. 4-6 generates not only the environmental position command x_{res}^{env} but also the environmental velocity command \dot{x}_{cmd}^{env} and the acceleration command \ddot{x}_{cmd}^{env} depending on the human force input. FIR filter for generating the environmental velocity command ($\frac{d}{dz}H(k)$) and the acceleration command ($\frac{d}{dz^2}H(k)$) are designed as shown in (4.10) and (4.11).

$$\begin{aligned} \frac{d}{dz}H(k) &= (j\omega) H^{ref} \left(\frac{2\pi k}{NT_s} \right), \\ (k &= 0, 1, \dots, N-1) \end{aligned} \quad (4.10)$$

$$\frac{d}{dz^2}(k) = (-\omega^2) H^{ref} \left(\frac{2\pi k}{NT_s} \right). \quad (4.11)$$

$(k = 0, 1, \dots, N - 1)$

These FIR filters are designed by multiplying $j\omega$ or $-\omega^2$ to the environmental transfer function $H^{ref}(j\omega)$. In Fig. 4-6, $\frac{d}{dz}H(k)$ and $\frac{d}{dz^2}(k)$ are implemented, respectively.



(a) System for abstraction of environment



(b) System for reproduction of environmental information

Fig. 4-7: Experimental system.

Table 4.1: Control parameters for abstraction of environment

Nominal mass	M_n	0.16	kg
Force feedback gain	K_f	44	
Cut-off frequency of DOB	g_{dis}	1200	rad/s
Cut-off frequency of RFOB	g_{reac}	1200	rad/s

4.4 Experiment

In this section, experimental results are shown to confirm the validity of the proposed method. Two kinds of experiments are done. One experiment is for abstraction of environment, the other is reproduction of environment.

4.4.1 Experimental System

Experiments was conducted using forceps robots as shown in Fig. 4-7. Figure 4-7(a) shows the robot for abstraction of environment. The end-effector is equipped for grasping environment. Figure 4-7(b) shows the robot for reproduction of environment. These two robots are comprised of one linear motor and one encoder. The resolution of encoder is $0.1 \mu\text{m}$. Parameters in experiments are listed in Table 4.1 and Table 4.2.

Table 4.2: Control parameters for reproduction of environment

Nominal mass	M_n	1.25	kg
Position feedback gain	K_p	10000	
Velocity feedback gain	K_v	200	
Cut-off frequency of DOB	g_{dis}	1000	rad/s

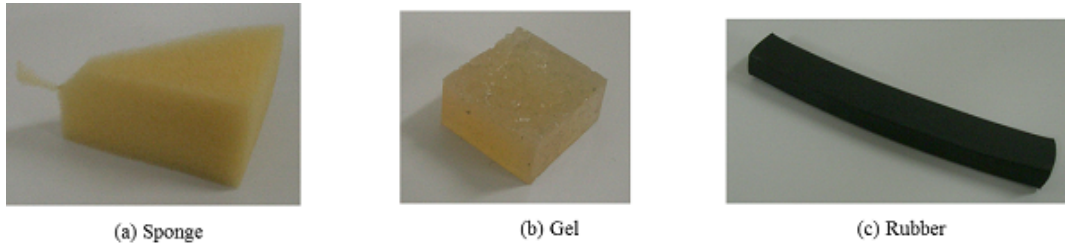


Fig. 4-8: Experimental materials.

4.4.2 Experimental Result

This subsection shows the experimental results.

Abstraction of Environment

The experiments were carried out with the sponge, te gel and the rubber as shown in Fig. 4-8. For adding an uniform force input to a certain frequency bandwidth, a bandwidth limited signal as shown in Fig. 4-9 is utilized as a force command f^{cmd} . Figure 4-9 (a) shows the time domain signal and Fig. 4-9 (b) shows the Fourier transformed signal. It is shown that the uniform force is added from 0 to 1 rad/s from Fig. 4-9.

In the experiment, the force input is set as (4.12).

$$f^{cmd} = 4 \frac{\sin(f_{band}t)}{(f_{band}t)}. \quad (4.12)$$

where, t is time[s], f_{band} is the bandwidth of the band limited signal. The band limited signal of (4.12) adds the uniform force from 0 to f_{band} rad/s. In the experiment, f_{band} is set to add the uniform force from 0 to 150 Hz.

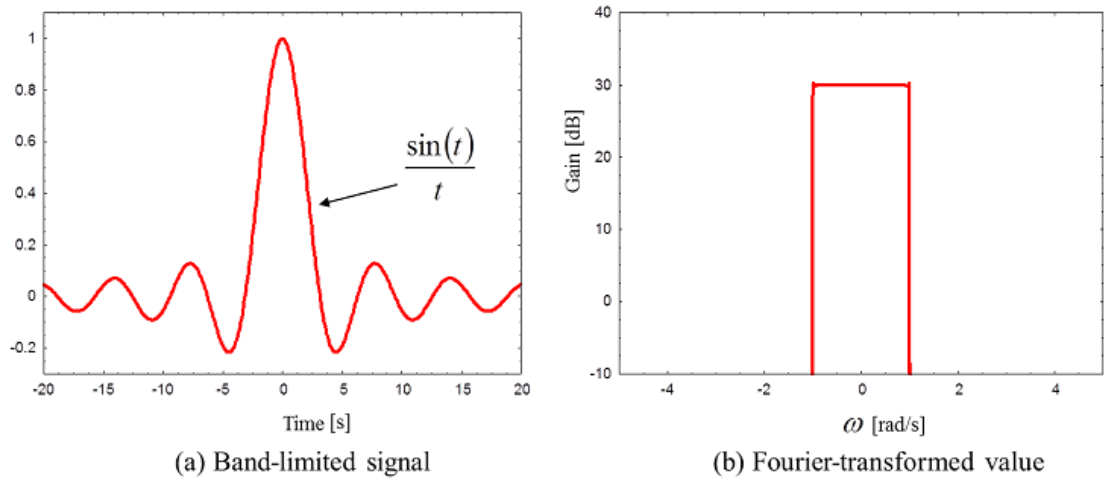


Fig. 4-9: Band-limited signal.

CHAPTER 4 REPRODUCTION OF ENVIRONMENT BASED ON FREQUENCY CHARACTERISTIC

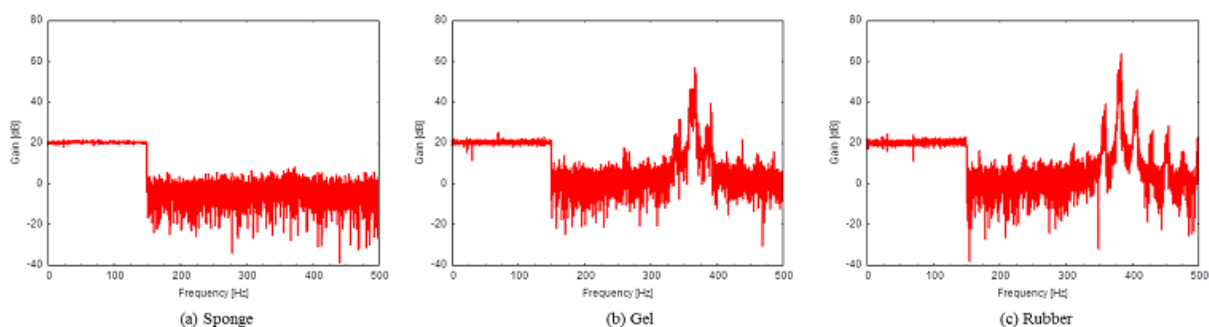


Fig. 4-10: Frequency spectrum of force response.

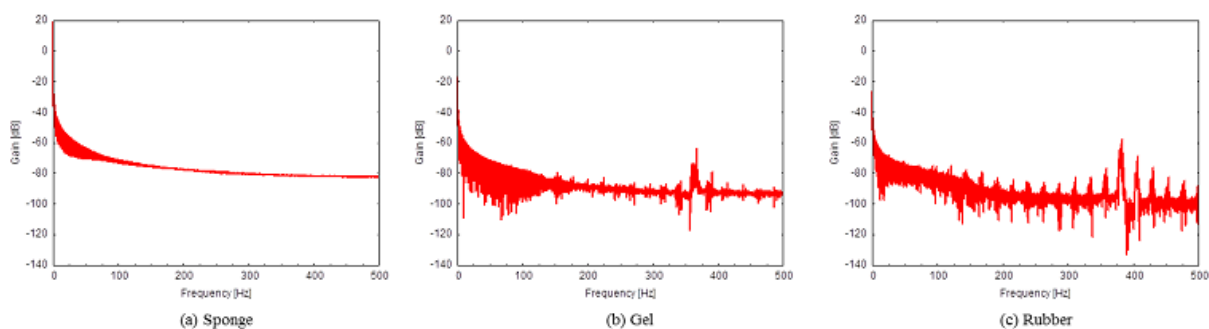


Fig. 4-11: Frequency spectrum of position response.

Figure 4-10–Fig. 4-12 shows the experimental results. Figure 4-10 and Fig. 4-11 are the Fourier transformed value of the position response and the force response. The vertical line shows gain[dB] and the horizontal line shows frequency[Hz]. From Fig. 4-10, it is shown that the uniform force is added from 0 to 150 Hz. The large gain in Fig. 4-10(b) and (c) are caused from the signal noise for sensing the force response. Figure 4-11 shows the spectrum of the position response for each environment.

Figure 4-12 shows the environmental impedances which are derived from Fig. 4-10 and Fig. 4-11. Environmental transfer functions are derived by reversing the spectrum of Fig. 4-12. Figure 4-12 shows that each environmental impedance becomes large in high frequency area. It is also shown that impedances of the sponge and the gel are linear to the frequency and the rubber is not. Therefore, frequency characteristics of environment are important to discriminate environmental impedances.

CHAPTER 4 REPRODUCTION OF ENVIRONMENT BASED ON FREQUENCY
CHARACTERISTIC

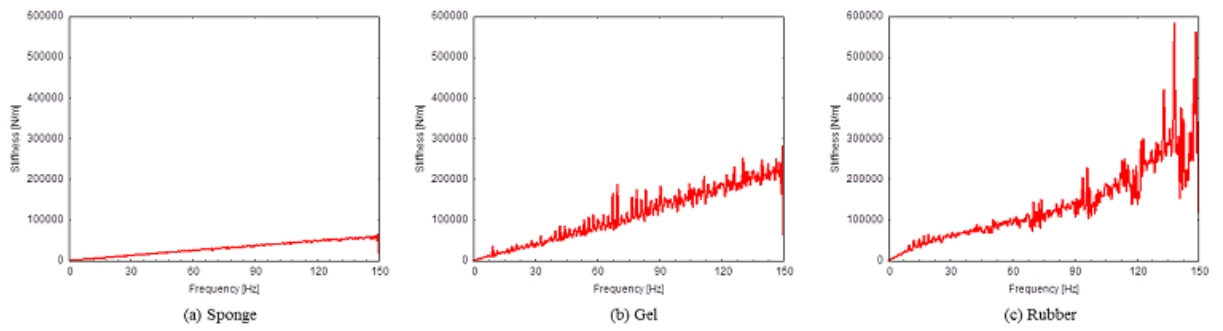


Fig. 4-12: Frequency spectrum of abstracted environment.

CHAPTER 4 REPRODUCTION OF ENVIRONMENT BASED ON FREQUENCY
CHARACTERISTIC

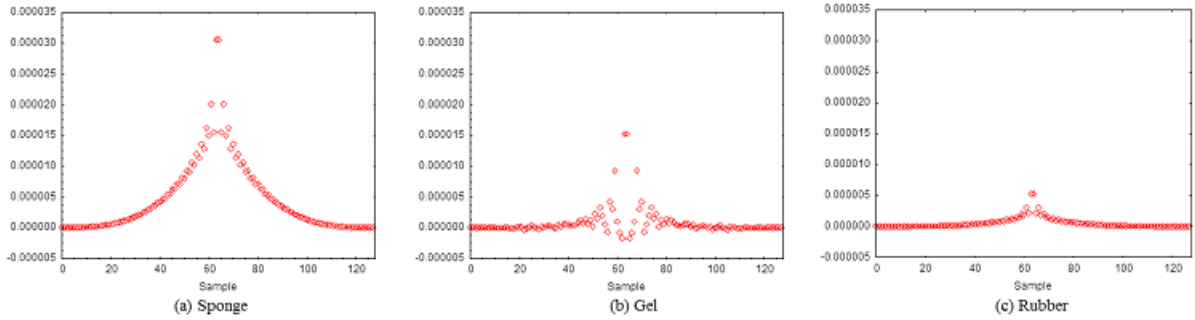


Fig. 4-13: Impulse response of FIR filter.

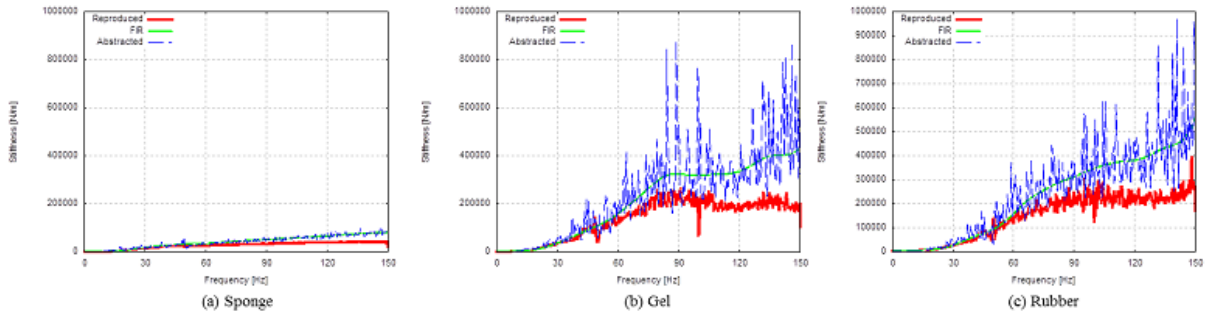


Fig. 4-14: Each frequency spectrum of environment.

Reproduction of Environment

For reproduction of environment, each parameter of FIR filter are designed by using frequency-sampling method. The order of the FIR filter is 127. The accuracy of environmental reproduction depends on the order of FIR filter. In this case, the accuracy of the frequency is about 8 Hz. The tactile receptor of human beings does not sense continuous frequency differences of the motion and sense the magnitude of the fast motion or the slow motion [5]. Thus, 8 Hz is enough as the accuracy of frequency. Finite response ($h(0) - h(127)$) of designed FIR filters are shown in Fig. 4-13.

Figure 4-14 shows the experimental results. In the experiment, the band limited signal is added as the force response. ‘Real’ shows abstracted environment, ‘Filter’ shows the inverse value of frequency characteristics which have been realized by FIR filter and ‘Environment’ shows reproduced environment. It is shown that frequency characteristics are same between abstracted environment and the inverse value

CHAPTER 4 REPRODUCTION OF ENVIRONMENT BASED ON FREQUENCY CHARACTERISTIC

of frequency characteristics which have been realized by FIR filter. It is also shown that reproduced environment is same with abstracted environment as follows. 0 to 90 Hz in the case of the sponge, 0 to 60 Hz in the case of the gel and 0 to 60 Hz in the case of the rubber. Then, three cases of environment such as the sponge, the gel and the rubber are reproduced. Therefore, it is shown that environment is reproduced by using the proposed control system.

4.5 Summary

In this chapter, a method for abstraction of environment based on frequency characteristics has been proposed. The force response and the position response of environment were transformed from time domain to frequency domain. Then, frequency characteristics of environment were abstracted. A method for reproduction of environment using FIR filter was also proposed. Desired frequency characteristics were approximated by using FIR filter. The validity of the proposed methods has been shown by experimental results. This method is valuable for abstraction and reproduction of real environment based on frequency characteristics.

Chapter 5

Haptic Motion Display System Based on Directionality

5.1 Background and Outline

Human environment has many unknown elements compared to industrial plants. Thus, the human recognition is important for robots working in human environment. The human recognition includes the recognition of the human face [54], the recognition of the human speech [55] and the recognition of the human intention [56,57]. With the application of the human recognition, a cooperation of human beings and robots is realized [58]. Robots are able to cooperate with human beings physically by detecting or predicting the human motion [59]. To the next step to human beings and robots interaction, robots which learn the human haptic motion [60] and robots which display the human haptic motion are researched.

In the previous researches about learning and displaying of the human haptic motion, the human haptic motion is measured in visual information [61]. Pavlovic proposed a method of teaching manipulating motions to robots. However, not only position information but also force information are important for measuring the human haptic motion such as handling objects. The reaction force from environment is utilized for acquiring human assembly motions [62]. In the proposed method, an instructor teaches a motion to robots by a force input. Then, robots display the motion to a learner by force information. However, especially the human action force in force information is important for measuring the human haptic motion.

For measuring the human action force, bilateral teleoperations are good candidates [63]. A bilateral teleoperation system is composed of a master system and a slave system. These master-slave systems

are bilateral controlled [64–66]. During bilateral teleoperations, the master system is manipulated by a human operator, and the slave system contacts with environment. Then, the master system measures the reaction force from the human operator, and the slave system measures the environmental position response. Therefore, by using the bilateral teleoperation system, the human action force and the environmental position response are measured [67].

After measuring the human action force and the position response, those data should be analyzed for abstracting motion. The concept of mode is useful for abstracting motions. As an example of mode, environmental mode has been researched for expressing the complicated environmental surface [68, 69]. Biped robots walk on the unevenness terrain recognizes the roughness based on environmental mode. End-effectors sense the contact information based on environmental mode. Function mode has been defined to realize various kinds of functions including the grasping function and the manipulating function [70]. Function mode has been designed based on the targeted function of a system. In this chapter, human motion is abstracted by mode. This mode is defined as action mode corresponding to environmental mode and function mode. Figure 5-1 shows environmental mode, function mode and action mode. Environmental mode is expressing environmental fragments. From Fig. 5-1 (a), when three end-effectors are contacting environment, environmental mode is expressing environmental fragments such as up and down, right and left and non-linear. Function mode is expressing functionalities of multi robot systems. From Fig. 5-1 (b), when two robots are grasping and manipulating objects, function mode is expressing functionalities such as the grasping function and the manipulating function. From Fig. 5-1 (c), action is divided to human actions and environmental actions from the point of the human action force and the environmental position response. Action indexes are assigned to each human action mode and environmental action mode.

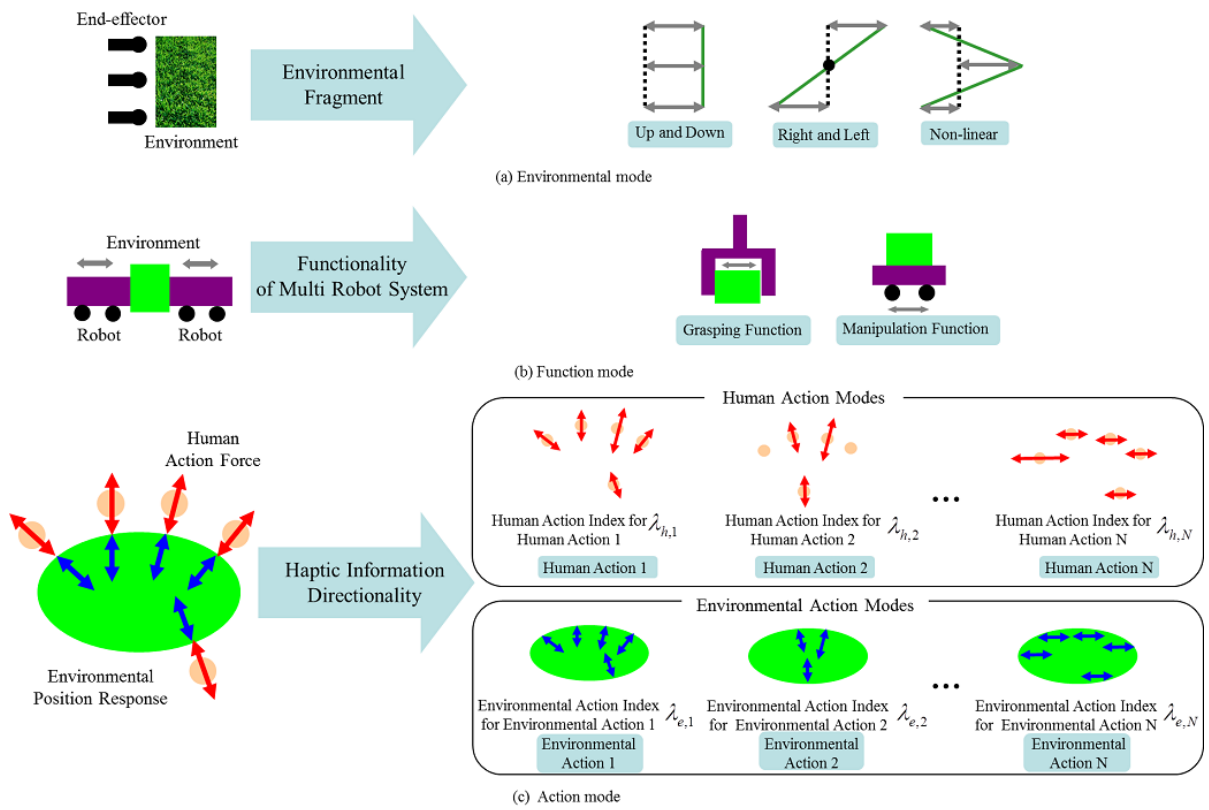


Fig. 5-1: Outline of each mode.

This chapter proposes a motion abstraction method and a motion display method based on action mode. The process for the motion measurement, the abstraction and the display is shown in Fig. 5-2. First in Fig. 5-2 (a), a bilateral control system [17] is implemented to the master robot hand and the slave robot hand. ‘Instructor’ does a motion by using the master robot hand. During a motion, ‘human action force’ and ‘environmental position response’ of Fig. 5-2 (a) are measured. Next in Fig. 5-2 (b), measured ‘human action force’ and ‘environmental position response’ are analyzed for abstracting the motion. Then, the measured motion is abstracted as human action mode and environmental action mode. Finally, in Fig. 5-2 (c), the haptic motion display system is implemented to the robot hand. In Fig. 5-2 (c), ‘robot hand position response’ is caused from the result of ‘human action force’. ‘Learner’ recognizes the motion directionality of ‘Instructor’ by adding the action force.

The composition of this chapter is described as follows. Section 5.2 explains about the motion abstraction method. Then, action mode and action indexes are defined. The motion display system based on force information is explained in section 5.3. The motion display system based on position and force information is explained in section 5.4. Finally, this chapter is summarized in section 5.5.

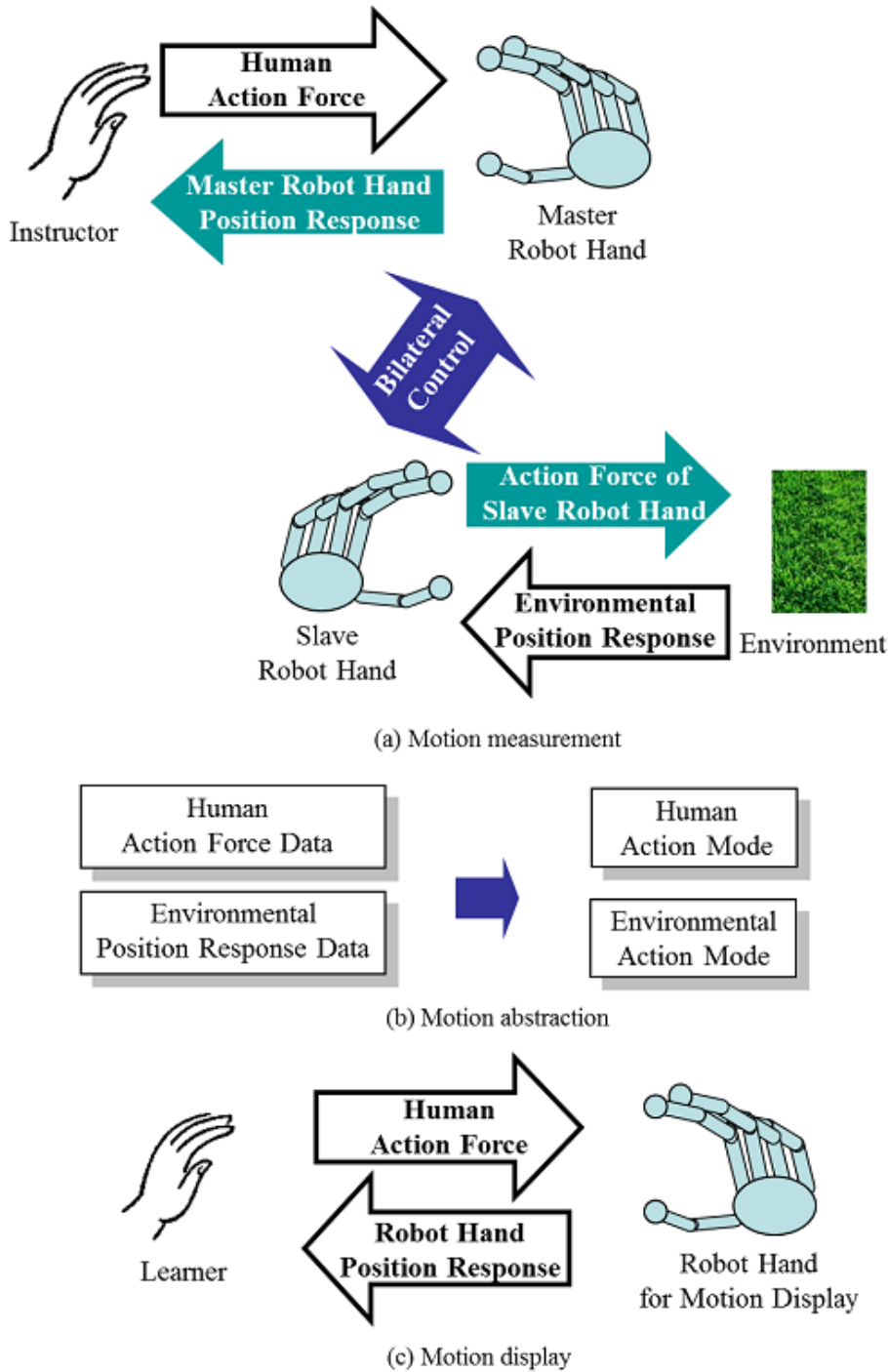


Fig. 5-2: Process for motion measurement, abstraction and display.

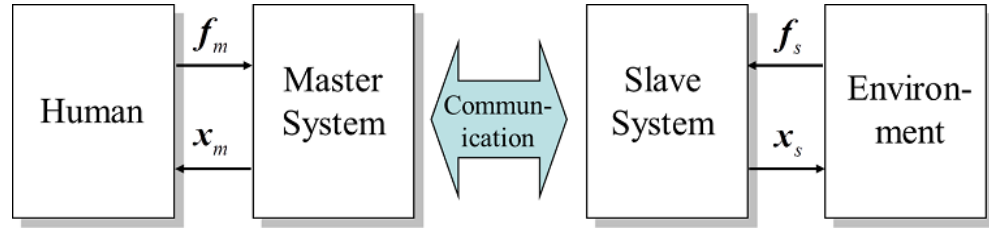


Fig. 5-3: Master-slave system.

5.2 Abstraction of Human Motion

This section proposes the motion abstraction method based on action mode and action indexes. Firstly, a master-slave system and those control system are explained. This system is utilized to sense the human action force and the environmental position response. Then, action mode and action indexes are explained.

5.2.1 Master-Slave System

In this subsection, the bilateral controlled master-slave system is explained. Figure 5-3 shows an information flow of the master-slave system. Human operator adds the action force f_h to the master system, and the reaction force from environment f_e is added to the slave system. Communication is conducted between the master system and the slave system for sharing x_m , x_s , f_h and f_e .

5.2.2 Control System

Figure 5-4 shows the bilateral control system for the master system and the slave system. The bilateral control system is implemented in the differential mode and the common mode. f_h , f_e , x_m and x_s are the action force from the human operator, the reaction force from environment, the position response of the master robot and the position response of the slave robot, respectively. Moreover, \ddot{x}_{dif}^{ref} , \ddot{x}_{com}^{ref} , \ddot{x}_m^{ref} and \ddot{x}_s^{ref} are the acceleration reference of the differential mode, the acceleration reference of the common mode, the acceleration reference of the master robot and the acceleration reference of the slave robot, respectively. By implementing this control system, the slaw of action and reaction between the human force f_h and the environmental reaction force f_e and the position tracking of the master system x_m and the slave system x_s are realized.

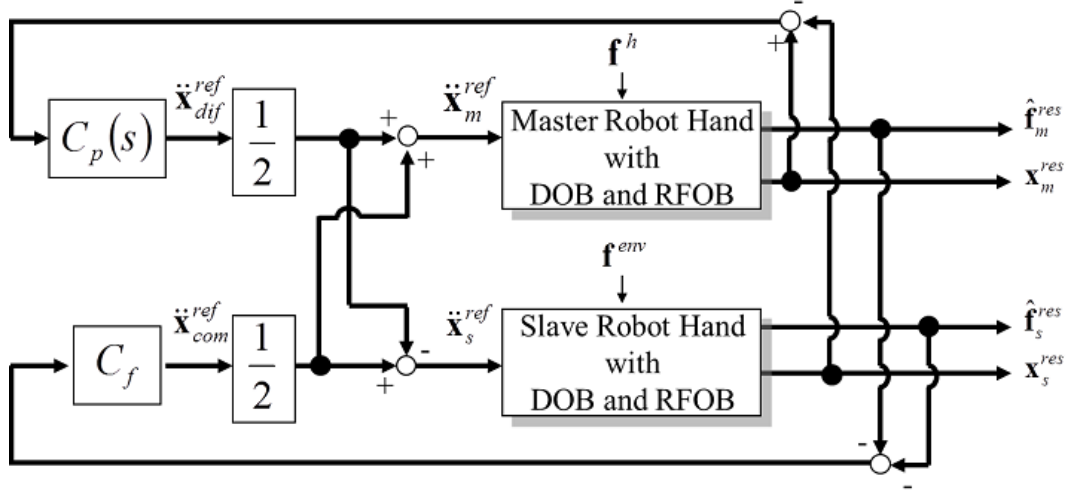


Fig. 5-4: Bilateral control system based on common mode and differential mode.

5.2.3 Action Mode and Action Index

Firstly, for calculating action mode and action indexes, the human action force data $\mathbf{f}_{m,i}$ and the environmental position response data $\mathbf{x}_{s,i}$ are set as follows.

$$\mathbf{f}_{m,i} = \begin{bmatrix} f_{m,i}[1] & \cdots & f_{m,i}[M] \end{bmatrix}^T, \quad (5.1)$$

$$\mathbf{x}_{s,i} = \begin{bmatrix} x_{s,i}[1] & \cdots & x_{s,i}[M] \end{bmatrix}^T. \quad (5.2)$$

where $i = 1, \dots, N$, $d = 1, \dots, M$, and N is a degree of freedom of the robot hand, M shows the number of the data saved in chronologic order, and the superscript T means the transpose of a matrix. $f_{m,i}[d]$ is i th part of d th reaction force data of the master robot hand, and $x_{s,i}[d]$ is i th part of d th position response data of the slave robot hand.

Secondly, the correlation matrices $\mathbf{R}_h \in \mathfrak{R}^{N \times N}$ and $\mathbf{R}_e \in \mathfrak{R}^{N \times N}$ are calculated as follows.

$$\mathbf{R}_h = \begin{bmatrix} \mathbf{f}_{m,1}^T \cdot \mathbf{f}_{m,1} & \cdots & \mathbf{f}_{m,1}^T \cdot \mathbf{f}_{m,N} \\ \vdots & \ddots & \vdots \\ \mathbf{f}_{m,N}^T \cdot \mathbf{f}_{m,1} & \cdots & \mathbf{f}_{m,N}^T \cdot \mathbf{f}_{m,N} \end{bmatrix}, \quad (5.3)$$

$$\mathbf{R}_e = \begin{bmatrix} \mathbf{x}_{s,1}^T \cdot \mathbf{x}_{s,1} & \cdots & \mathbf{x}_{s,1}^T \cdot \mathbf{x}_{s,N} \\ \vdots & \ddots & \vdots \\ \mathbf{x}_{s,N}^T \cdot \mathbf{x}_{s,1} & \cdots & \mathbf{x}_{s,N}^T \cdot \mathbf{x}_{s,N} \end{bmatrix}. \quad (5.4)$$

Components of the correlation matrices \mathbf{R}_h and \mathbf{R}_e are calculated by inner products of each human action force data $\mathbf{f}_{m,i}$ and environmental position response data $\mathbf{x}_{s,i}$, respectively. The correlation matrices \mathbf{R}_h and \mathbf{R}_e show statistical relationships of each human action force data $\mathbf{f}_{m,i}$ and environmental position response data $\mathbf{x}_{s,i}$.

Thirdly, transformation matrices $\mathbf{T}_h \in \mathfrak{R}^{N \times N}$ and $\mathbf{T}_e \in \mathfrak{R}^{N \times N}$ are calculated by diagonalizing the correlation matrices \mathbf{R}_h and \mathbf{R}_e as shown in (5.5) – (5.8), respectively. Calculations of transformation matrices \mathbf{T}_h and \mathbf{T}_e from correlation matrices \mathbf{R}_h and \mathbf{R}_e are realized by Jacobi method [71].

$$\mathbf{T}_h^{-1} \mathbf{R}_h \mathbf{T}_h = \text{diag} \left\{ \lambda_{h,1}, \lambda_{h,2}, \dots, \lambda_{h,N} \right\}, \quad (5.5)$$

$$\mathbf{T}_h = [\mathbf{t}_{h,1}, \mathbf{t}_{h,2}, \dots, \mathbf{t}_{h,N}], \quad (5.6)$$

where $i = 1, \dots, N$, and $\lambda_{h,i}$ is the i th eigenvalue, and $\mathbf{t}_{h,i} \in \mathfrak{R}^N$ is its corresponding eigenvector.

$$\mathbf{T}_e^{-1} \mathbf{R}_e \mathbf{T}_e = \text{diag} \left\{ \lambda_{e,1}, \lambda_{e,2}, \dots, \lambda_{e,N} \right\}, \quad (5.7)$$

$$\mathbf{T}_e = [\mathbf{t}_{e,1}, \mathbf{t}_{e,2}, \dots, \mathbf{t}_{e,N}], \quad (5.8)$$

where $i = 1, \dots, N$, and $\lambda_{e,i}$ is the i th eigenvalue, and $\mathbf{t}_{e,i} \in \mathfrak{R}^N$ is its corresponding eigenvector.

Since the correlation matrices \mathbf{R}_h and \mathbf{R}_e are real symmetric matrices, following two points are realized [72]. One point is that transformation matrices \mathbf{T}_h , \mathbf{T}_e and eigenvalues $\lambda_{h,i}$, $\lambda_{e,i}$ are calculated in any human action force data $\mathbf{f}_{m,i}$ and any environmental position response data $\mathbf{x}_{s,i}$. The other point is that transformation matrices \mathbf{T}_h and \mathbf{T}_e are orthonormal matrices. Thus, inverse matrices \mathbf{T}_h^{-1} and \mathbf{T}_e^{-1} are equal to transposed matrices of \mathbf{T}_h^T and \mathbf{T}_e^T .

Then, human action mode and human action indexes are calculated as

$$\mathbf{t}_{h,1}, \mathbf{t}_{h,2}, \dots, \mathbf{t}_{h,N}, \quad (5.9)$$

$$\lambda_{h,1}, \lambda_{h,2}, \dots, \lambda_{h,N}. \quad (5.10)$$

Environmental action mode and environmental action indexes are calculated as

$$\mathbf{t}_{e,1}, \mathbf{t}_{e,2}, \dots, \mathbf{t}_{e,N}, \quad (5.11)$$

$$\lambda_{e,1}, \lambda_{e,2}, \dots, \lambda_{e,N}. \quad (5.12)$$

For expressing the directionality, each eigenvector of transformation matrices T_h and T_e are utilized. Eigenvalues are utilized for showing the total input to each action mode in the measured haptic motion.

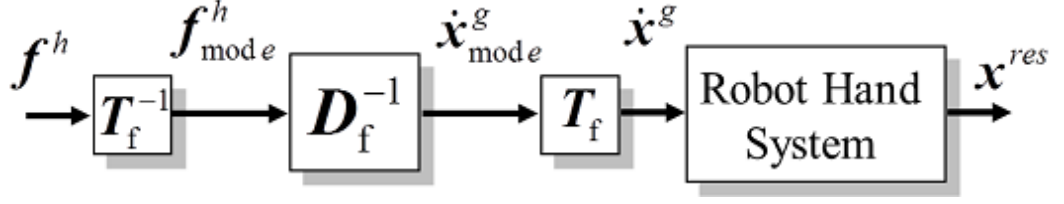


Fig. 5-5: Motion display system based on force information.

5.3 Motion Display System Based on Force Information

This section proposes the motion display system based on force information. Firstly, the outline of this motion display system is explained. Then, the control system is shown. After that, experimental results are shown.

5.3.1 Outline of Motion Display System Based on Force Information

Figure 5-5 shows the proposed motion display system. where f^h , T_f^{-1} , f_{mode}^h , D_f and \dot{x}_{mode}^g are the human action force, the transformation matrix to action mode, the human action force in action mode, the virtual damping matrix which is designed from action ratios, the velocity command for the motion display system and the position response of robots, respectively. (5.13) shows the virtual damping matrix.

$$D_f = \begin{bmatrix} d_1 & 0 & \cdots & 0 \\ 0 & d_2 & & \vdots \\ \vdots & & \ddots & 0 \\ 0 & \cdots & 0 & d_N \end{bmatrix}. \quad (5.13)$$

Here, action ratios ε_i are defined as (5.14).

$$\varepsilon_i = \frac{\lambda_{f,i}}{\lambda_{f,max}}, \quad (5.14)$$

where i is $1, \dots, N$. $\lambda_{f,max}$ is the maximum value of human action indexes. Action ratios range from 0 to 1. The value of action ratios shows the importance of the corresponding action mode. The virtual damping matrix D_f is designed to induce the action mode which has the large action ratio. Moreover, the action mode which has the small action ratio is suppressed.

5.3.2 Control System

Figure 5-6 shows the control system for the motion display system which is explained in 5.3.1. DOB

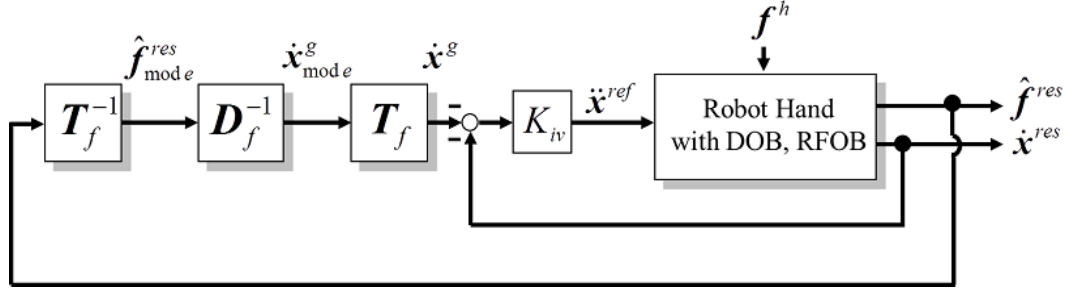


Fig. 5-6: Control system of motion display system based on force information.

is implemented to the robot hand for realizing the robust acceleration control. RFOB is utilized to sense the human action force \hat{f}^{res} . In Fig. 5-6, \ddot{x}^{ref} shows the acceleration reference of the robot and K_{iv} shows the velocity feedback gain. Here, virtual damping matrix is designed as (5.15).

$$d_i = \frac{d_g}{\varepsilon_i}, \quad (5.15)$$

where i is $1, \dots, N$ and d_g shows the nominal damper.

As action ratio ε_i ranges from 0 to 1, the action mode which has the largest action ratio has the nominal damper d_g . In the other action modes, the virtual damper increases from the nominal damper d_g .

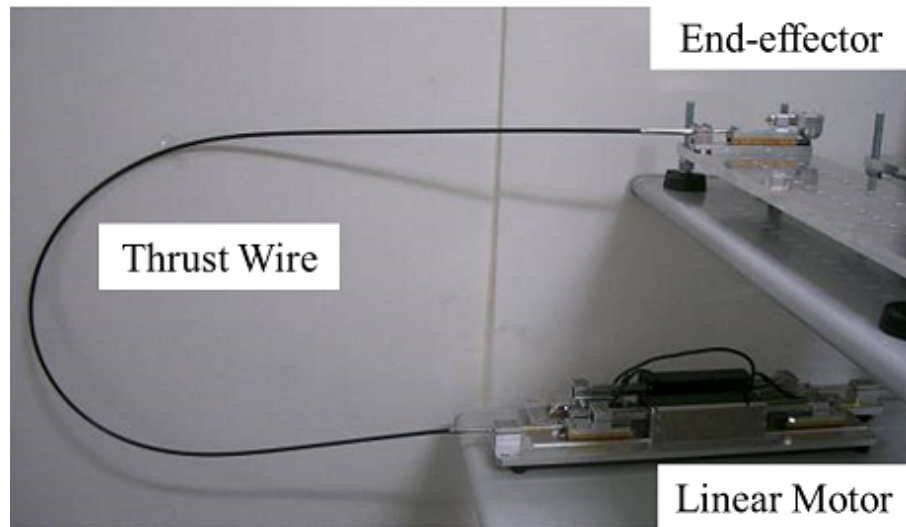


Fig. 5-7: Flexible actuator.

5.3.3 Experiment

Experimental System

Figure 5-7 shows the flexible actuator which is utilized in this experiment. As explained in chapter 3, the flexible actuator is composed of the linear motor, the thrust wire and the end-effector. The thrust wire works to transmit the force from the linear motor to the end-effector.

Figure 5-8 shows the experimental system. The experimental system composed of the robot hand for the master system and the robot hand for the slave system. Each robot hand is controlled from separated computers and each of them are communicated in real time by RT-Socket [73]. Control parameters for experiments are shown in Table 5.1.

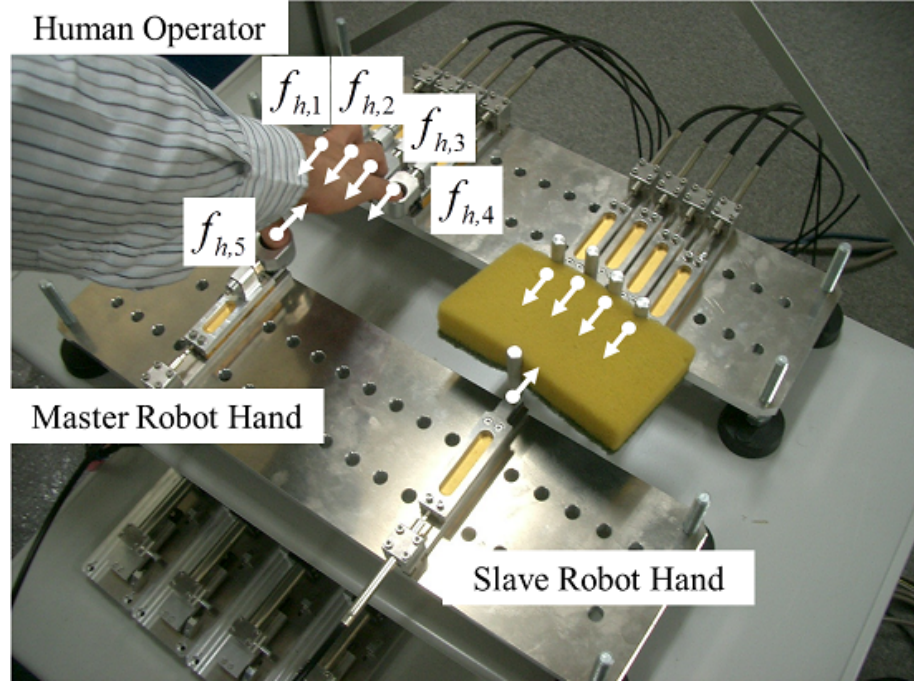


Fig. 5-8: Experimental system.

Table 5.1: Control parameters

Nominal mass	M_n	0.5	kg
Position feedback gain	K_p	1600	
Velocity feedback gain (bilateral control)	K_v	80	
Force feedback gain	K_f	2	
Velocity feedback gain (motion guide)	K_{iv}	500	
Base damper	d_g	80	
Cut-off frequency of DOB, RFOB	g_{dis}, g_{reac}	500	rad/s

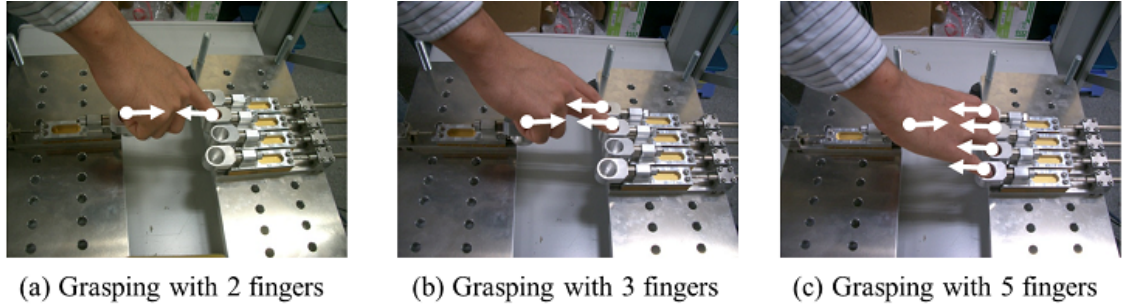


Fig. 5-9: Experimental cases.

Experimental Result

Experiments for the motion measurement, the motion abstraction and the motion display have been conducted. In the experiments for the motion measurement, three cases of motions as shown in Fig. 5-9 were conducted. Case 1 is corresponding to the grasping motion with two fingers as shown in Fig. 5-9(a). Case 2 is corresponding to the grasping motion with three fingers as shown in Fig. 5-9(b). Case 3 is corresponding to the grasping motion with five fingers as shown in Fig. 5-9(c).

In the experiment for the motion display, it is supposed that following kinds of the force are added to the master robot hand.

$$\begin{bmatrix} f_{mode,1}^h \\ f_{mode,2}^h \\ f_{mode,3}^h \\ f_{mode,4}^h \\ f_{mode,5}^h \end{bmatrix} = \begin{bmatrix} \sin\left(\frac{2\pi t}{5}\right) \\ \sin\left(\frac{2\pi t}{5}\right) \\ \sin\left(\frac{2\pi t}{5}\right) \\ \sin\left(\frac{2\pi t}{5}\right) \\ \sin\left(\frac{2\pi t}{5}\right) \end{bmatrix}. \quad (5.16)$$

Here, t means a time [s].

Figure 5-10–Fig. 5-12 show the experimental results. Figure 5-10(a) – (c) show the force response of the master robot in the experiment for the motion abstraction. From Fig. 5-10(a), it is shown that $f_{m,2}^{res}$ and $f_{m,5}^{res}$ sense the reaction force. In case 1, the grasping motion is conducted by $f_{m,2}^{res}$ and $f_{m,5}^{res}$ as shown in Fig. 5-9(a). From Fig. 5-10(b) and (c), the reaction force is sensed from the robot hands which are utilized for the grasping motion.

Figure 5-11(a) – (c) show the action mode which has the largest action ratio. These values are calculated by analyzing the experimental results of Fig. 5-10. In Fig. 5-11, each circle is corresponding to the robot hand of Fig. 5-9. The direction and the length Fig. 5-11 are corresponding to the eigen vector of each action mode. From Fig. 5-11, it is shown that action mode which has the largest action ratio is corresponding to each grasping motion. Therefore, it is shown that the human motion is abstracted by utilizing the proposed motion abstraction method.

Figure 5-12(a) – (c) shows the velocity response of action mode for experiments of the motion display. Each line is showing the corresponding action ratios. From Fig. 5-12, it is shown that large velocity response is caused from the action mode which has large action ratio. By utilizing the proposed motion display system, the action mode which has the large action ratio is induced and the action mode which has the small action ratio is restricted.

Therefore, the proposed motion abstraction and motion display system are verified from experimental results. These methods are valid to visualize the intention of the human action.

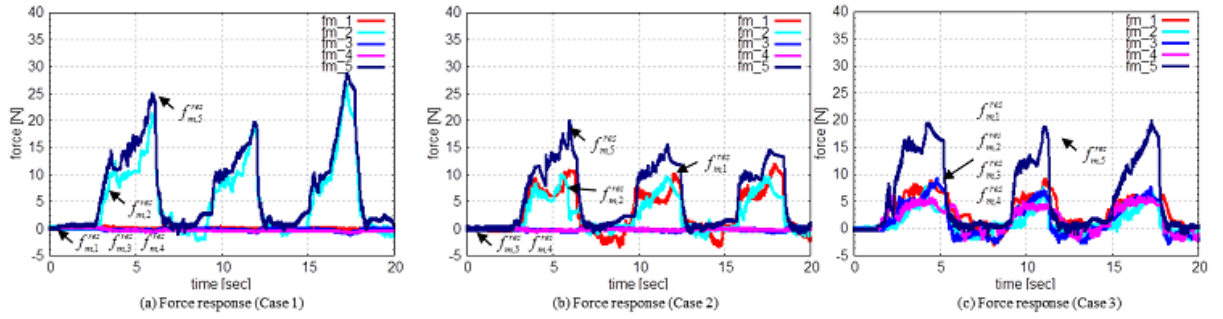


Fig. 5-10: Experimental results for motion measurement.

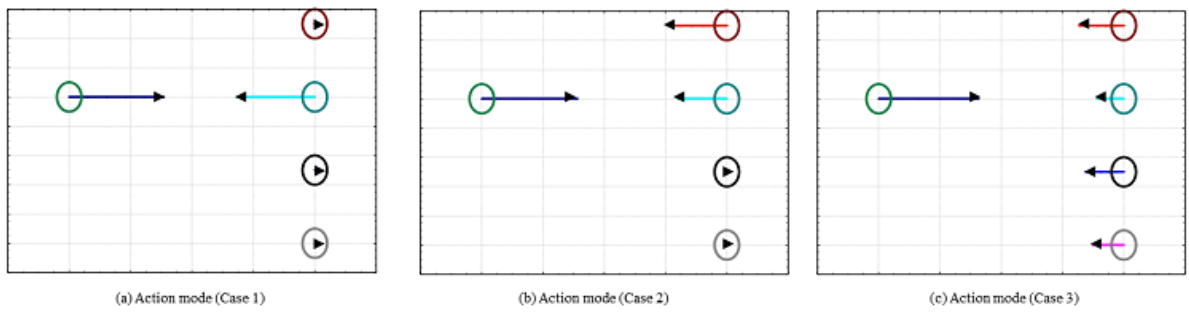


Fig. 5-11: Abstracted action modes.

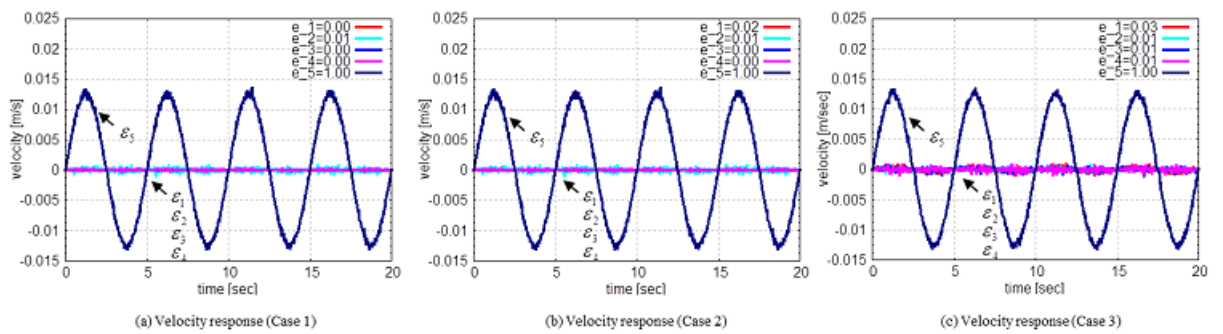


Fig. 5-12: Experimental results for motion display.

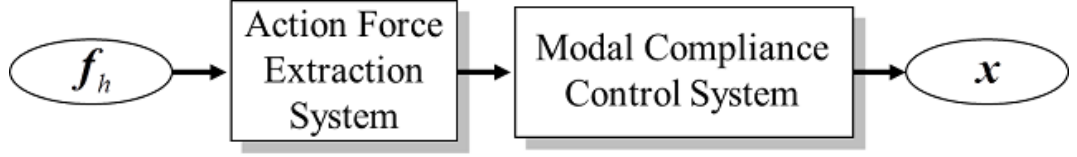


Fig. 5-13: Motion display system based on position and force information.

5.4 Motion Display System Based on Position and Force Information

This section proposes the motion display system based on position and force information. Firstly, the outline of this motion display system is explained. Then, the control system is shown. After that, experimental results are shown.

5.4.1 Outline of Motion Display System Based on Position and Force Information

Figure 5-13 shows the proposed motion display system. This motion display system is composed of two systems. One system is for the action force extraction. In this system, the human action force is spatially filtered. So, the human action force of the desired direction is extracted in this system.

The other system is the modal compliance control system. A targeted compliance is realized between the extracted action force and the position response. The compliance is decided based on action indexes.

5.4.2 Control System

The haptic motion display system is realizing the position response directionality depending on the human action force directionality. The relationship of the position response directionality and the human action force directionality are realized by environmental action indexes and human action indexes.

Control System for Motion Display

Figure 5-14 shows the control system for the haptic motion display. DOB is implemented to the robot hand. The human action force f^h is estimated by using RFOB as \hat{f}^{res} . In Fig. 5-14, the estimated reaction force \hat{f}^{res} is transformed to human action mode by T_h^{-1} . The modal compliance controller calculates the position command x_e^c , the velocity command \dot{x}_e^c and the acceleration command \ddot{x}_e^c as follows.

$$M_c \ddot{x}_e^c + D_c \dot{x}_e^c + K_c x_e^c = -CK_f \hat{f}_h^{res}, \quad (5.17)$$

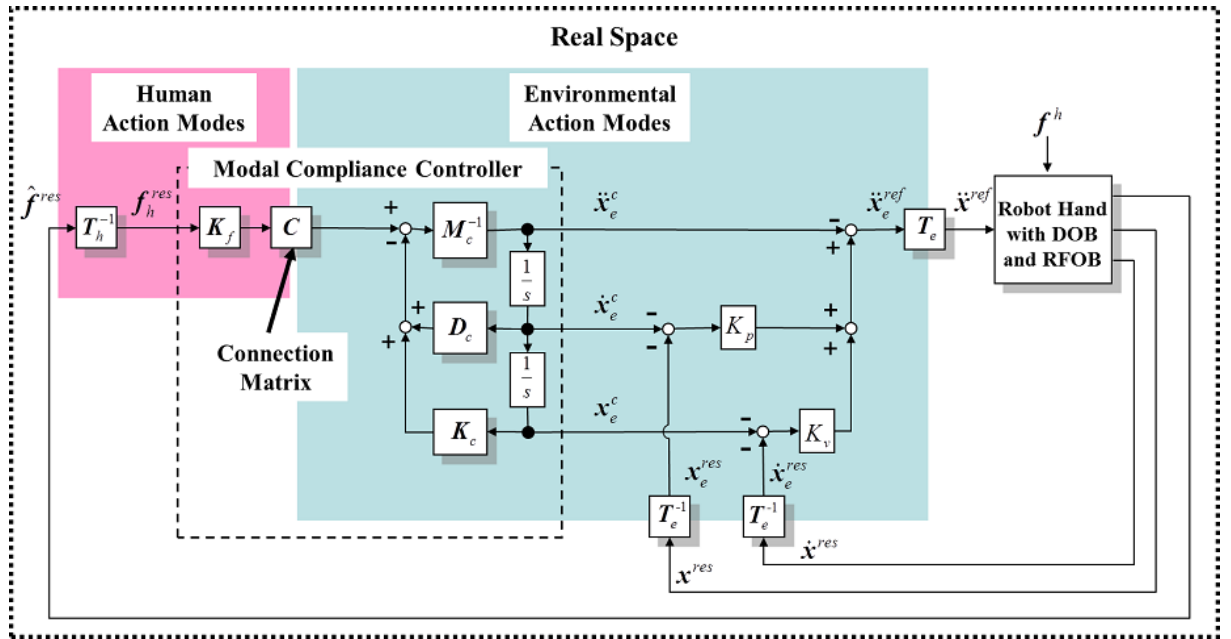


Fig. 5-14: Control system of motion display system based on position and force information.

where C is a connection matrix, and K_f , K_c , M_c and D_c are matrices of the modal compliance controller. C , K_f , K_c , M_c and D_c are designed from the desired stiffness between the force response of the human action mode f_h^{res} and the position response of environmental action mode x_e^{res} . The design method of C , K_f , K_c , M_c and D_c are explained in next subsection 5.4.3. Then, the position control is performed in environmental action mode. K_p and K_v are a proportional gain and a derivative gain. The acceleration reference of the robot hand \ddot{x}_e^{ref} is calculated by transforming the acceleration reference of the environmental action mode \ddot{x}_e^{ref} .

5.4.3 Design of Modal Compliance Controller

In the modal compliance controller, the desired stiffness between \mathbf{f}_h^{res} and \mathbf{x}_e^{res} is designed as

$$\frac{f_{h,i}^{res}}{x_{e,j}^{res}} = \frac{1}{\lambda_{h,i}} \sqrt{\frac{\lambda_{h,i}}{\lambda_{e,j}}}, \quad (5.18)$$

$$\lambda_{h,max} = \max \{ \lambda_{h,i} \}, \quad (5.19)$$

where $i = 1, \dots, N$, and $j = 1, \dots, N$. The desired stiffness is set as the amplitude of the human action index $\frac{\lambda_{h,i}}{\lambda_{h,max}}$ and the ratio of action indexes $\sqrt{\frac{\lambda_{h,i}}{\lambda_{e,j}}}$. $\frac{\lambda_{h,i}}{\lambda_{h,max}}$ is set for realizing the strong relationship between the human action mode which has the large human action indexes and environmental action mode. $\sqrt{\frac{\lambda_{h,i}}{\lambda_{e,j}}}$ is designed for making the stiffness as the ratio of the total human action force and the total environmental position response in the measured haptic motion. From the point of the implementation, when $\sqrt{\frac{\lambda_{h,i}}{\lambda_{e,j}}}$ is larger than K_p , both $\lambda_{h,i}$ and $\lambda_{e,j}$ are tuned to make $\sqrt{\frac{\lambda_{h,i}}{\lambda_{e,j}}}$ equal to K_p . Therefore, the range of the modal stiffness is 0 to K_p .

For realizing the desired stiffness, the connection matrix \mathbf{C} and matrices of the modal compliance controller \mathbf{K}_f , \mathbf{K}_c , \mathbf{M}_c , \mathbf{D}_c are set as

$$\mathbf{C} = \begin{bmatrix} \frac{\lambda_{h,1}}{\lambda_{h,max}} & \dots & \frac{\lambda_{h,1}}{\lambda_{h,max}} \\ \vdots & \ddots & \vdots \\ \frac{\lambda_{h,N}}{\lambda_{h,max}} & \dots & \frac{\lambda_{h,N}}{\lambda_{h,max}} \end{bmatrix}, \quad (5.20)$$

$$\mathbf{K}_f = \text{diag} \left\{ \frac{1}{\sqrt{\lambda_{h,1}}}, \frac{1}{\sqrt{\lambda_{h,2}}}, \dots, \frac{1}{\sqrt{\lambda_{h,N}}} \right\}, \quad (5.21)$$

$$\mathbf{K}_c = \text{diag} \left\{ \frac{1}{\sqrt{\lambda_{e,1}}}, \frac{1}{\sqrt{\lambda_{e,2}}}, \dots, \frac{1}{\sqrt{\lambda_{e,N}}} \right\}, \quad (5.22)$$

$$\mathbf{M}_c = \text{diag} \left\{ \frac{M_n}{K_p \sqrt{\lambda_{e,1}}}, \frac{M_n}{K_p \sqrt{\lambda_{e,2}}}, \dots, \frac{M_n}{K_p \sqrt{\lambda_{e,N}}} \right\}, \quad (5.23)$$

$$\mathbf{D}_c = \text{diag} \left\{ 2\sqrt{\frac{M_n}{K_p \lambda_{e,1}}}, 2\sqrt{\frac{M_n}{K_p \lambda_{e,2}}}, \dots, 2\sqrt{\frac{M_n}{K_p \lambda_{e,n}}} \right\}, \quad (5.24)$$

where M_n is a nominal mass of DOB.

When the ideal acceleration control is realized by DOB, (5.29) is yielded from (5.17) and (5.20) – (5.24) as follows.

Firstly, the acceleration reference of the modal compliance controller is calculated as (5.25).

$$\ddot{\mathbf{x}}_e^{ref} = K_p (-\mathbf{x}_e^{res} - \mathbf{x}_e^c) + K_v (-\dot{\mathbf{x}}_e^{res} - \dot{\mathbf{x}}_e^c) + (-\ddot{\mathbf{x}}_e^c). \quad (5.25)$$

When the ideal acceleration control is realized by DOB, i. e. $\ddot{\mathbf{x}}_e^{ref} = \ddot{\mathbf{x}}_e^{res}$, (5.26) is derived from (5.17) and (5.25).

$$M_c \ddot{\mathbf{x}}_e^{res} + D_c \dot{\mathbf{x}}_e^{res} + K_c \mathbf{x}_e^{res} = -CK_f \mathbf{F}_h^{res}. \quad (5.26)$$

Then, (5.26) is transformed to (5.27).

$$\mathbf{x}_e^{res} = \begin{bmatrix} \frac{1}{M_{c,1}s^2 + D_{c,1}s + K_{c,1}} & 0 & \cdots & 0 \\ 0 & \frac{1}{M_{c,2}s^2 + D_{c,2}s + K_{c,2}} & & \vdots \\ \vdots & & \ddots & 0 \\ 0 & \cdots & 0 & \frac{1}{M_{c,N}s^2 + D_{c,N}s + K_{c,N}} \end{bmatrix} CK_f \mathbf{f}_h^{res}. \quad (5.27)$$

Here, $CK_f \mathbf{f}_h^{res}$ is culated as (5.28).

$$CK_f \mathbf{f}_h^{res} = \begin{bmatrix} \frac{1}{\sqrt{\lambda_{x,1}}} \frac{\lambda_{f,1}}{\lambda_{f,max}} & 0 & \cdots & 0 \\ 0 & \frac{1}{\sqrt{\lambda_{x,2}}} \frac{\lambda_{f,2}}{\lambda_{f,max}} & & \vdots \\ \vdots & & \ddots & 0 \\ 0 & \cdots & 0 & \frac{1}{\sqrt{\lambda_{x,N}}} \frac{\lambda_{f,N}}{\lambda_{f,max}} \end{bmatrix} \mathbf{f}_h^{res}. \quad (5.28)$$

$$\mathbf{x}_e^{res} = - \begin{bmatrix} \frac{\lambda_{h,1}}{\lambda_{h,max}} \frac{1}{\sqrt{\frac{\lambda_{h,1}}{\lambda_{e,1}} \frac{M_n}{K_p}} \left(s^2 + 2\sqrt{\frac{K_p}{M_n}} s + \frac{K_p}{M_n} \right)} \\ \vdots \\ \frac{\lambda_{h,N}}{\lambda_{h,max}} \frac{1}{\sqrt{\frac{\lambda_{h,1}}{\lambda_{e,N}} \frac{M_n}{K_p}} \left(s^2 + 2\sqrt{\frac{K_p}{M_n}} s + \frac{K_p}{M_n} \right)} \\ \dots \\ \frac{\lambda_{h,1}}{\lambda_{h,max}} \frac{1}{\sqrt{\frac{\lambda_{h,N}}{\lambda_{e,1}} \frac{M_n}{K_p}} \left(s^2 + 2\sqrt{\frac{K_p}{M_n}} s + \frac{K_p}{M_n} \right)} \\ \vdots \\ \dots \\ \frac{\lambda_{h,N}}{\lambda_{h,max}} \frac{1}{\sqrt{\frac{\lambda_{h,N}}{\lambda_{e,N}} \frac{M_n}{K_p}} \left(s^2 + 2\sqrt{\frac{K_p}{M_n}} s + \frac{K_p}{M_n} \right)} \end{bmatrix} \mathbf{f}_h^{res}. \quad (5.29)$$

(5.29) is calculated from (5.27) and (5.28). Eq. (5.29) shows Laplace transformed dynamics between the force response of human action mode \mathbf{f}_h^{res} and the position response of environmental action mode \mathbf{x}_e^{res} . And, it is shown that all natural frequencies in transfer function from \mathbf{f}_h^{res} to \mathbf{x}_e^{res} are set as $\sqrt{\frac{K_p}{M_n}}$. Moreover, the damping coefficient is set to 1. When s is set to 0, stiffness between \mathbf{f}_h^{res} and \mathbf{x}_e^{res} is set to the desired stiffness which is shown in (5.18).

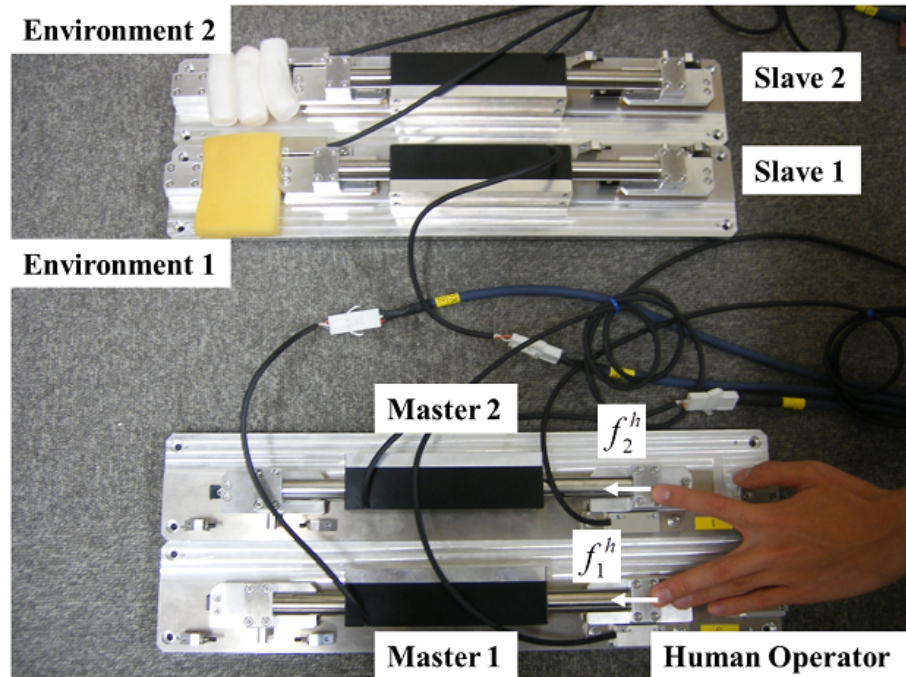


Fig. 5-15: Experimental system.

5.4.4 Experiment

Experimental System

Experiments were conducted to verify the motion abstraction methods based on human action mode and environmental action mode. The haptic motion display system is also verified by adding various types of the human action force. In these experiments, the verification was conducted by the artificially added external force.

The experimental system is shown in Fig. 5-15. For verifying the designed haptic motion display system, only the two degree of freedom was utilized in the master system and the slave system. Two slave systems contact with different environment. One environment is the sponge, the other environment is the foam polystyrene. These two environments are set for simulating the real environment. When all human hands touch the objects in the real environment, each hand does not feel totally same stiffness. Each system is composed of a linear motor and an encoder. The rated thrust force and the maximum rated thrust force of the linear motors are 20 N and 78 N, respectively. The resolution of encoders is 0.1 μm . Control parameters used in the experiments are shown in Table 5.2. These parameters are decided

Table 5.2: Control parameters

Nominal mass	M_n	0.5	kg
Position feedback gain	K_p	2500	
Velocity feedback gain	K_v	100	
Force feedback gain	K_f	2	
Cut-off frequency of DOB, RFOB	g_d, g_r	500	rad/s

from the performance of the experimental system.

Experiments were composed of experiments for the motion measurement, the motion abstraction and the motion display. In the experiments for the motion measurement, the bilateral control system [17] is utilized. Following three kinds of the action force were supposed to be added to the master system in the experiments for the motion measurement.

Case 1 $f_1^{hum} = 10, f_2^{hum} = 5,$

Case 2 $f_1^{hum} = 5, f_2^{hum} = 5,$

Case 3 $f_1^{hum} = 5, f_2^{hum} = 10.$

These external forces are realized by the current reference values to the linear motors of two master systems. After experiments for the motion measurement, human action mode, environmental action mode and action indexes of each action mode were calculated. In the experiments for the motion display, abstracted action mode and action indexes were implemented in the motion display system. Only the master system was utilized in the experiments for the motion display. Eq. (5.30) and (5.31) show the action force which was supposed to be added to the master system.

$$f_1^{hum} = a \cos(bt), \quad (5.30)$$

$$f_2^{hum} = a \sin(bt), \quad (5.31)$$

where $t[s]$ is time. The action force f_1^{hum} and f_2^{hum} are designed for adding all ratios of the action force (f_1^{hum} and f_2^{hum}) at the constant amplitude. This is the reason that only two degree of freedoms of the master system and the slave system were utilized. These action forces were realized by setting the reaction force to the system as shown in (5.30) and (5.31). In the experiments for motion display, a and b in (5.30) and (5.31) were set as 5 and $\frac{2}{5}\pi$ just arbitrary values.

Experimental Result

Figure 5-16 – Fig. 5-18 show the experimental results. Figure 5-16 shows the experimental results for the motion measurement. Figure 5-16 (a) – (c) show the force response of each master system and slave system. It is shown that the force responses are measured as the aimed action force. Figure 5-16 (d) – (f) show the position response of each master system and slave system. From Fig. 5-16, it is shown that the position response is caused depending on the the action force and the environmental position response.

Figure 5-17 shows abstracted action modes. In Fig. 5-17, human action mode and environmental action mode are shown. The human action mode which has the largest human action index is shown in the bold line. The environmental action mode which has the largest environmental action index is shown in the bold line. In Fig. 5-17 (a) – (c), the human action modes which have the largest human action index are $t_{h,1}$, $t_{h,2}$ and $t_{h,2}$, respectively. Those human action modes are decided by the ratio of the action force f_1^{hum} and f_2^{hum} . The environmental action modes which have the largest environmental action index are $t_{e,1}$, $t_{e,1}$ and $t_{e,2}$, respectively. Those environmental action modes are decided by the ratio of the environmental position response $x_{s,1}^{res}$ and $x_{s,2}^{res}$. Those environmental action modes are not equal to the human action modes. This is because that each stiffness of environment is different. Thus, it is shown that human action mode is expressing the human action force directionality and environmental action mode is expressing the environmental position response directionality.

Figure 5-18 (a) – (c) show the force response in human action mode and the position response in environmental action mode. The human action mode which has the largest human action index is shown in bold line. The environmental action mode which has the largest environmental action index is shown in bold line. In Fig. 5-18 (a) – (c), 'l.h' is showing a human action index, and 'l.e' is showing an environmental action index. From Fig. 5-18 (a) – (c), it is shown that the position response of environmental action mode is caused depending on the force response of human action mode which have the large human action index. In addition, it is also shown that the amplitude of the position response of environmental action mode is depending on the amplitude of environmental action indexe.

Figure 5-18 (d) – (f) show the stiffness response. For calculating the stiffness responses, the force response of the human action mode which has the largest human action index are divided by the position response of environmental action mode. In Fig. 5-18 (d) – (f), 'sqrt(l.h/l.e)' is showing the ratio of action indexes $\sqrt{\frac{\lambda_h}{\lambda_e}}$. The ratio is showing the designed stiffness between the force response of the human action mode which has the largest human action index and the position response of environmental action mode.

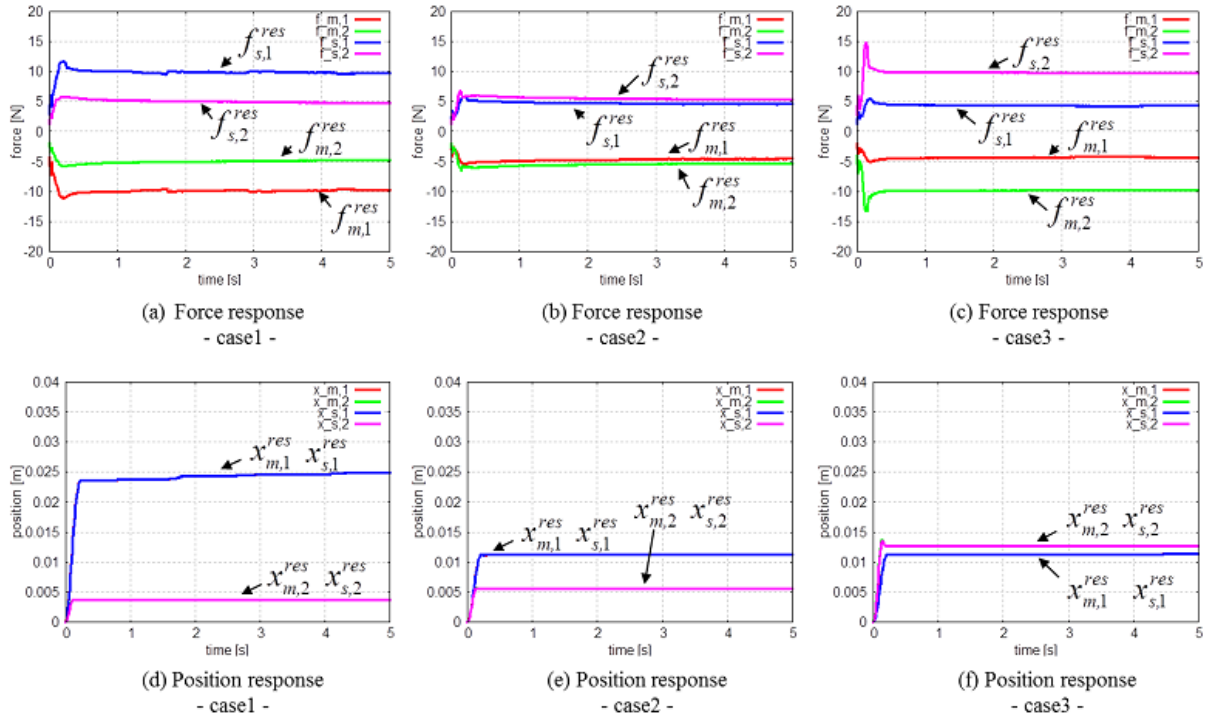


Fig. 5-16: Experimental results for motion measurement.

Dot lines of Fig. 5-18 (d) – (f) are showing these designed stiffness. From Fig. 5-18 (d) – (f), it is shown that the stiffness is realized as the designed values. In addition, these designed values are decided from the ratio of action indexes of each action mode.

Therefore, it is shown that the designed haptic motion display system is realizing the position response directionality depending on the human action force directionality. In addition, the relationship of the human action force directionality and the position response directionality are decided based on human action indexes and environmental action indexes.

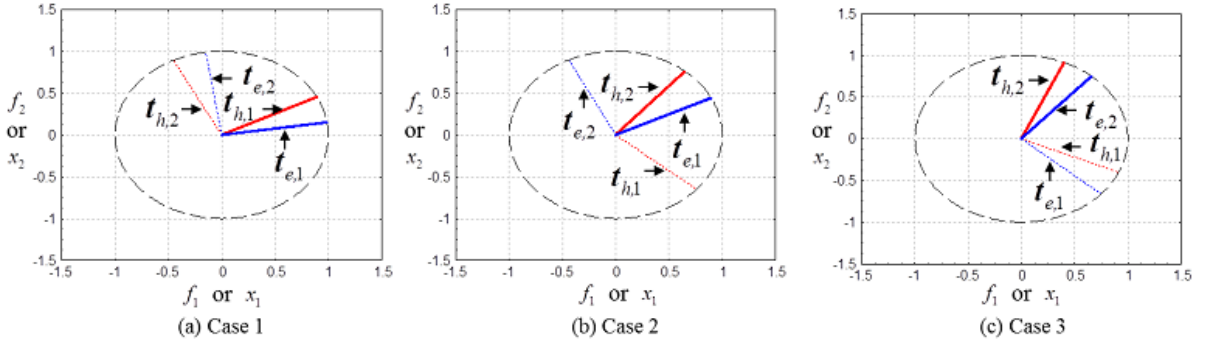


Fig. 5-17: Abstracted action modes.

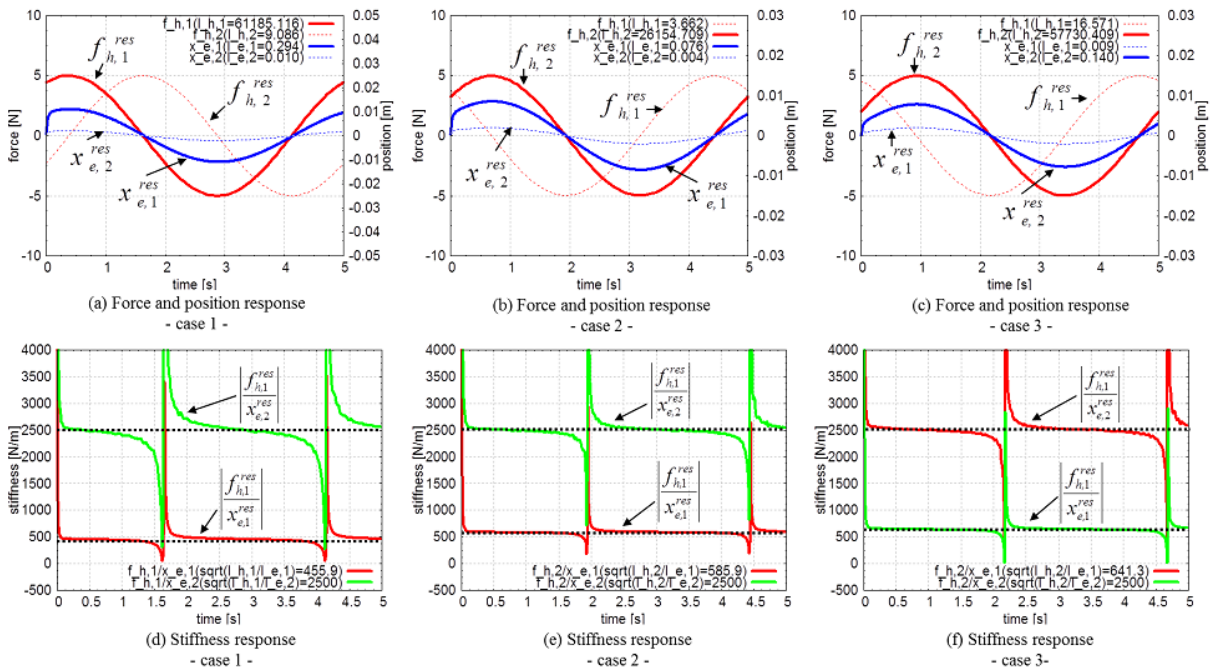


Fig. 5-18: Experimental results for motion display.

5.5 Summary

This chapter has defined human action mode and environmental action mode. A measured haptic motion is divided to each human action and environmental action by human action mode and environmental action mode. Furthermore, two types of haptic motion display system have been designed. One is based on human action mode. The other is based on human action mode and environmental action mode. The validity of the proposed methods was shown from the experimental results.

Chapter 6

Motion Control System with Time Delay

6.1 Background and Outline

Time delay in control systems seriously deteriorates the stability and the performance of the control system and many works have been addressed [74]. The time delay problem used to be dealt with mainly in process or plant engineering in the early phase of time delay system researches. In recent years, the time delay problem in network based control systems (NBCs) or networked control systems (NCSs) has been drawing much attentions [75,76]. Time delay is time varying and unpredictable in network systems. Moreover, there are also other communication constraints like packet dropouts, limited bandwidth, and so on. This kind of situations becomes more seriously, if space communication is considered [77].

As a time delay compensation method, Smith predictor is a famous and useful approach [78, 79]. It predicts the delayed output of the system by using the controlled system model and the time delay model. Then, the time delay effect in the control system is compensated by using the predicted delayed output. PID controller and Model predictive(MPC) is also a useful method and used for various researches [80, 81].

A time delay compensation method based on network disturbance (ND) concept and CDOB has been studied [82, 83]. The major advantage of this method is the time delay model is not required, thus it can be implemented easily in most cases where time delay is unknown. However, the disadvantage is that CDOB is not so robust to the system model error, the disturbance and time-varying delay. Recently, CDOB which is robust against the model error and the disturbance is proposed [84, 85]. This improved CDOB utilizes the compensation value from the delayed system input instead of the system output.

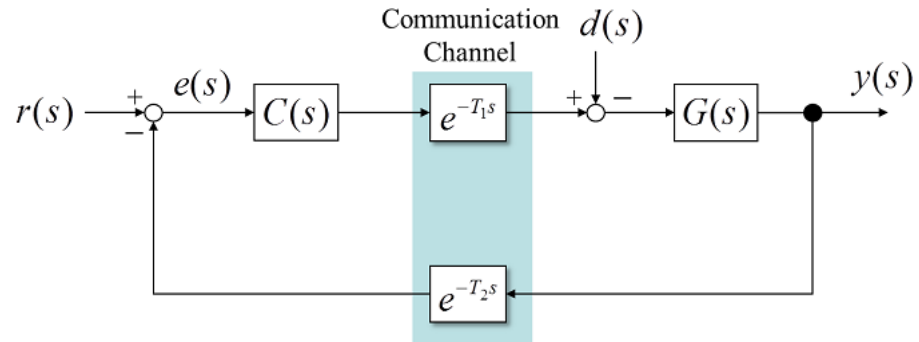


Fig. 6-1: Feedback control system with time delay.

For solving the problem to implement CDOB to NBCs or NCSs in which time delay is unstable, the robustness against time varying delay should be addressed.

In this chapter, considering unstable time delay, a structure of the time delay control system with CDOB is modified. As the nonlinear effect like communication packet dropouts or jitter can deteriorate the total control system, a case study is accomplished considering the allocation of the system model in CDOB. Then, the more robust CDOB structure against packet dropouts and jitter is abstracted. The validity of the modified structure is shown by experimental results.

The composition of this chapter is described as follows. In section 6.2, the time delay effect and the time delay compensation by CDOB are introduced. Allocations of the system model in CDOB are studied in section 6.3. The robustness of the modified CDOB structure against packet dropouts and jitter is confirmed by simulations. The validity of the modified structure is shown by experimental results 6.4. Finally, this chapter is summarized in section 6.5.

6.2 Time Delay Compensation

This section introduces the time delay effect and the time delay compensation by CDOB.

6.2.1 Time Delay Effect

A feedback control system with the input delay T_1 and the output delay T_2 is shown in Fig. 6-1. In the figure, $G(s)$ is the controlled system, $r(s)$ and $y(s)$ are the input and the output, respectively. The

closed-loop transfer function of Fig. 6-1 is described as follows.

$$G_{closed}(s) = \frac{C(s)G(s)e^{-T_1s}}{1 + C(s)G(s)e^{-Ts}}. \quad (6.1)$$

Here, the round trip time delay is $T = T_1 + T_2$. The time delay element is included in the denominator. It affects the performance and possibly causes the instability.

6.2.2 Time Delay Compensation by CDOB

This subsection introduces the time delay compensation by CDOB. Figure 6-2(b) shows the control system with the time delay compensation by CDOB. DOB is implemented to the controlled system to minimize the model error between the system model in CDOB ($\hat{G}(s)$) and the controlled system ($G(s)$). $L_d(s)$ in Fig. 6-2 shows the LPF in DOB. Figure 6-2(a) shows the control system with the time delay compensation by Smith predictor. \hat{T} means the round trip time delay ($T = T_1 + T_2$) model in Fig. 6-2(a). In Fig. 6-2(a), the time delay compensation value 'comp' is calculated by the system model ($\hat{G}(s)$) and the round trip time delay model (\hat{T}). On the other hand, CDOB calculates the compensation value 'comp' by the differentiation of the signal before and after going through the communication channel. Here, the one is 'comp1' and the other is 'comp2'. Thus, CDOB can calculate the compensation value which is equivalent to Smith predictor. Moreover, it does not need the round trip time delay model (\hat{T}).

Stability

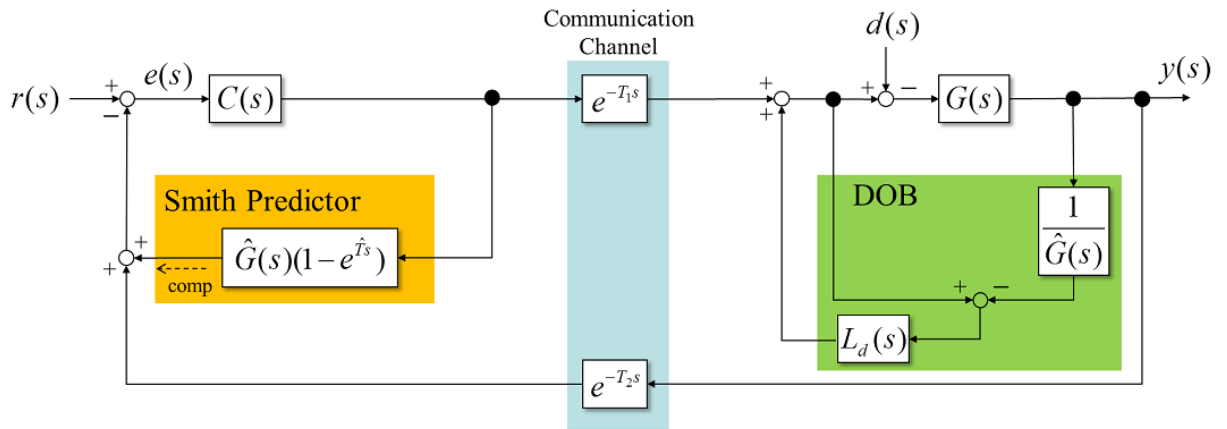
When the cut-off frequency of LPF in DOB approaches infinity, the closed transfer function in Fig. 6-2(b) is described as follows.

$$G_{closed}(s) = \frac{C(s)G(s)e^{-T_1s}}{1 + C(s)\hat{G}(s)}. \quad (6.2)$$

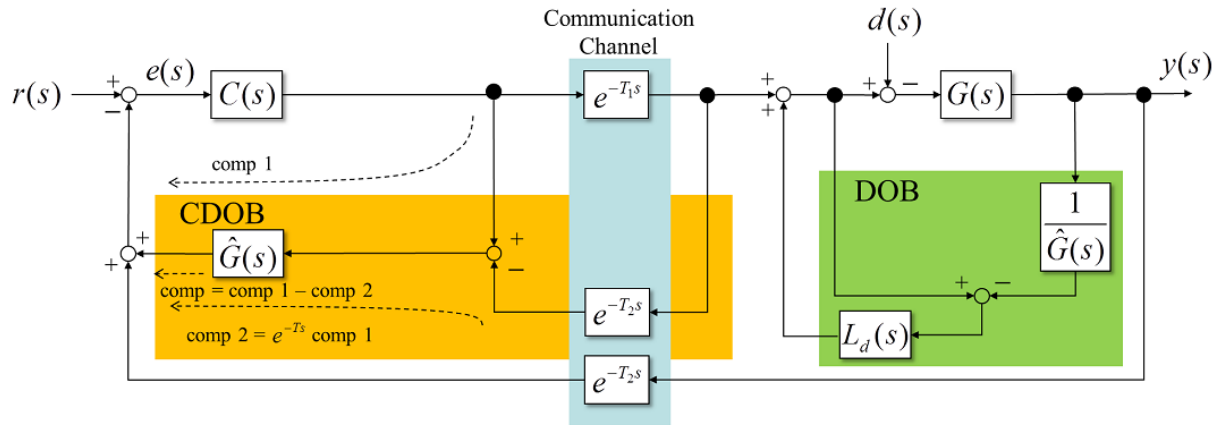
In (6.2), there is no time delay element in the denominator of the transfer function. Thus, this system is not destabilized from the time delay effect. Moreover, it is shown that the denominator of the transfer function is designed from the system model ($\hat{G}(s)$).

Steady-state Characteristic

When the controller ($C(s)$) is a PD controller and the control system ($G(s)$) and the system model ($\hat{G}(s)$) are an inertial system which is expressed as a double integrator, the control system of Fig. 6-2(b) is expressed as (6.3) to (6.5).



(a) Time delay compensation by Smith predictor



(b) Time delay compensation by CDOB

Fig. 6-2: Time delay compensation.

$$C(s) = M_n(K_v s + K_p), \tag{6.3}$$

$$G(s) = \frac{1}{M s^2}, \tag{6.4}$$

$$\hat{G}(s) = \frac{1}{M_n s^2}. \tag{6.5}$$

Then, the error $e(s)$ in Fig. 6-2(b) is expressed as (6.6).

$$e(s) = \left(1 - \frac{C(s)G(s)e^{-T_1s}}{1 + C(s)\hat{G}(s)}\right)r(s). \quad (6.6)$$

Thus, the steady-state error from the step input ($r(s) = \frac{1}{s}$) is calculated as follows from (6.3) to (6.6).

$$\lim_{s \rightarrow 0} e(s) \frac{1}{s} = 0. \quad (6.7)$$

It is shown that the steady-state error from the step input is zero. (6.7) is realized even if the model error exists between the controlled system ($G(s)$) and the system model ($\hat{G}(s)$). Thus, there is no steady-state error even if there exists the model error.

Table 6.1: Number of communication channel passage in each CDOB.

Type of CDOB	Number of communication channel passage
Type1	2
Type2	1
Type3	0

6.3 Time Delay Compensation Considering Unstable Time Delay

This section studies about allocations of the system model in CDOB. Candidates for the structure of CDOB is explained in 6.3.1. The robustness of the modified CDOB structure against packet dropouts and jitter is confirmed by simulations in subsection 6.3.2. Some discussions about candidates for the structure of CDOB is conducted in 6.3.3.

6.3.1 Candidate for the structure of CDOB

For analyzing the structure of CDOB, the time delay control system with CDOB in Fig. 6-3(a) are equivalently transformed as shown in Fig. 6-3(b). There are two flows in CDOB. The one calculates 'comp1' which does not go through the communication channel and the other calculates 'comp2' which goes through the communication channel. The flow which calculates 'comp1' can allocate the system model ($\hat{G}(s)$) in one place. On the other hand, the flow which calculates 'comp2' can allocate the system model ($\hat{G}(s)$) several places in relating to the position of the communication channel. As shown in Fig. 6-3(c), the system model can be allocated three places.

Here, if the system model ($\hat{G}(s)$) is allocated to Type 1, Type 2 and Type 3 in Fig. 6-3(c), respectively, the number of communication channel passages before reaching the system model ($\hat{G}(s)$) becomes as Table 6.1. As shown in Table 6.2, by utilizing type 3, the integral calculation is conducted before going through the communication channel. The integral calculation will be affected from the nonlinear effect like communication packet dropouts or jitter. So, type 3 has the possibility to reduce the nonlinear effect. In subsection 6.3.2, simulations re conducted to Type 1, Type 2 and Type 3 to confirm the type 3 is valid to reduce the nonlinear effect.

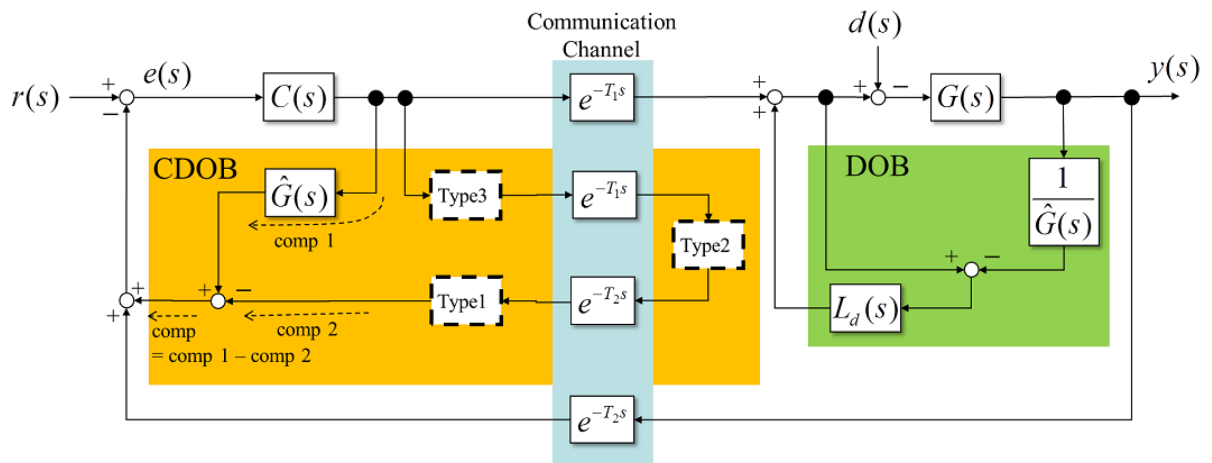
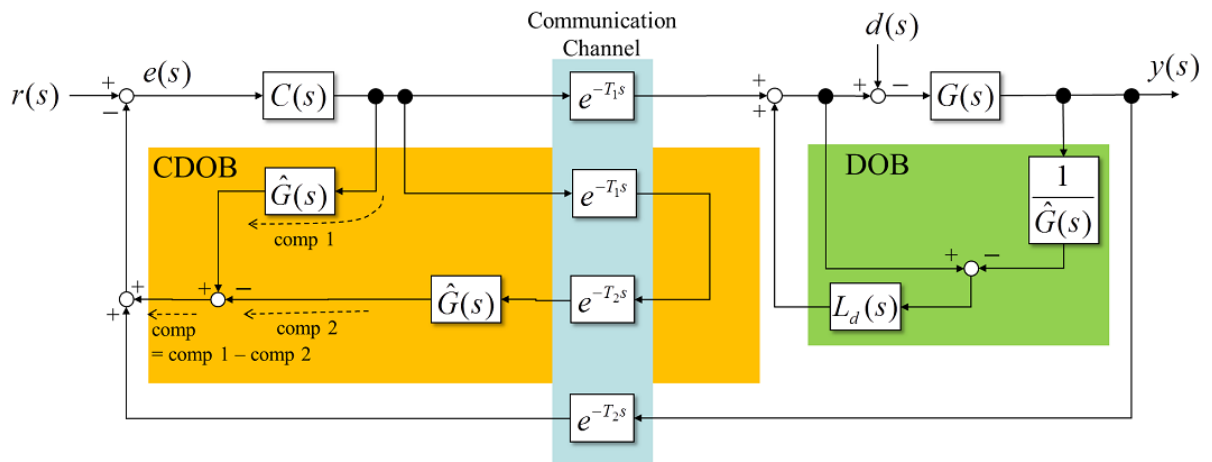
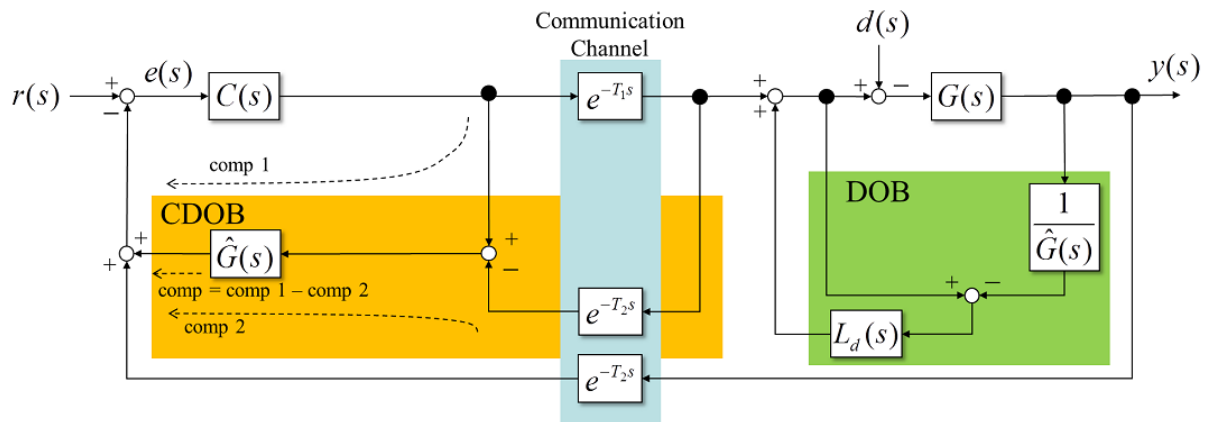


Fig. 6-3: Candidate for the structure of CDOB.

Table 6.2: Parameters for simulation and experiment.

Position feedback gain	K_P	900	
Velocity feedback gain	K_V	60	
Cut-off frequency of DOB	g_{dis}	500	rad/s
Mass	M	0.5	kg
Nominal mass	M_n	0.6	kg
Thrust coefficient	K_{tn}	32.5	N/A

6.3.2 Simulation

In this subsection, simulation results are shown to confirm the robustness of the modified CDOB structure against packet dropouts and jitter. The modified CDOB structure is corresponding to Fig. 6-3(c). Table 6.2 shows the parameter for simulations.

Following three kinds of communication conditions are considered in simulations.

Case 1 : Constant Delay

$$T_1 = T_2 = 200\text{ms}$$

Case 2 : Packet Dropouts

$T_1 = T_2 = 200\text{ms}$. Packet dropouts are occurred during 0.5 to 0.6s. Each part receives same data during that period.

Case 3 : Jitter

$T_1 = T_2 = 200\text{ms} \pm 30\text{ms}$. Here, T_1 is time delay from the controller ($C(s)$) to the controlled system ($G(s)$). T_2 is time delay from the controlled system ($G(s)$) to the controller ($C(s)$). The sampling period (T_s) is 0.001s and the communication period (T_c) is 0.001s. When the packet dropouts are occurred in case 2, the zero-order hold is conducted in the receiving side. In case 3, if the several packet data is received, the latest packet data is utilized.

CHAPTER 6 MOTION CONTROL SYSTEM WITH TIME DELAY

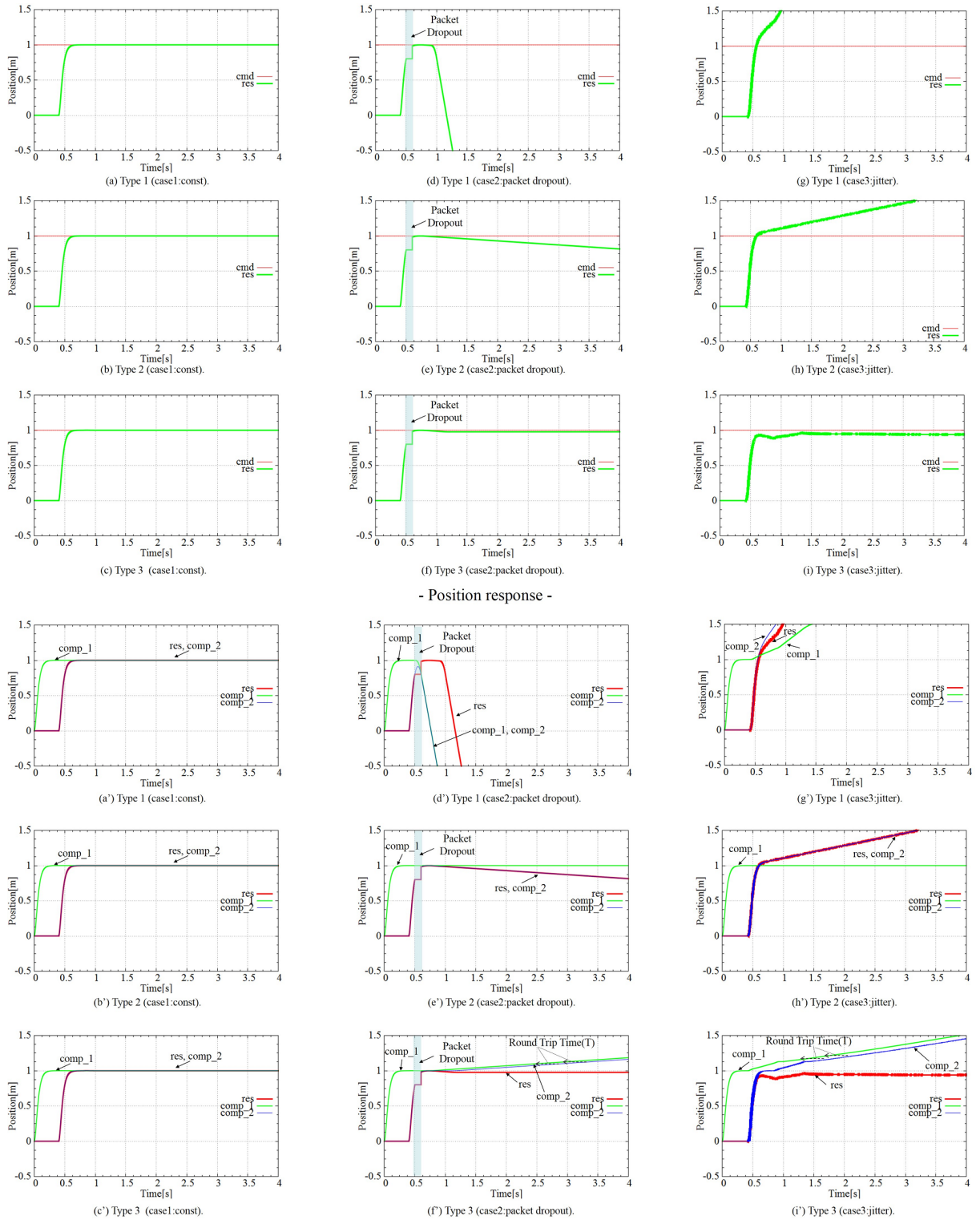


Fig. 6-4: Simulation result.

Figure 6-4 shows the simulation results. Figure 6-4(a)–(i) shows the position response of each case. 'cmd' shows the position command and 'res' shows the position response which is received in the controller. Simulation results for case 1(Constant Delay) are shown in Fig. 6-4(a)–(c). Even though there exist the model error between the mass of the controlled system (M) and the mass model (M_n) of the system model, there are no steady-state error in all cases. Simulation results for case 2(Packet Dropouts) are shown in Fig. 6-4(d)–(f). The position responses are same in all cases before the packet dropouts occurs. After the packet dropouts occurred, steady-state errors become large in the order of Type 1, Type 2 and Type 3. There are large steady-state errors in Type 1 and Type 2. On the other hand, the steady-state error is small in Type 3 and the position response tracks the position command in Type 3. Simulation results for case 3(Jitter) are shown in Fig. 6-4(g)–(i). Steady-state errors become large in the order of Type 1, Type 2 and Type 3. There are large steady-state errors in Type 1 and Type 2. On the other hand, the steady-state error is small in Type 3 and the position response tracks the position command in Type 3.

Figure 6-4(a')–(i') shows the compensation values such 'comp 1' and 'comp 2'. The compensation values for CDOB are calculated by the differentiation of 'comp 1' and 'comp 2'. The compensation values which are corresponding to simulation results for case 1(Constant Delay) are shown in Fig. 6-4(a')–(c'). In each case, after the position response ('res') converges to the position command, 'comp 1' and 'comp 2' converges to the constant value and the compensation value ('comp') becomes zero. The compensation values which are corresponding to simulation results for case 2(Packet Dropouts) are shown in Fig. 6-4(d')–(f'). 'comp1' and 'comp2' become the same value in Type 1 after the packet dropouts occurred. As shown in Fig. 6-2, there should be the round trip time delay ($T = T_1 + T_2$) between 'comp 1' and 'comp 2'. Thus, CDOB in Type 1 does not work. In type 2, the difference between 'comp1' and 'comp2' monotonically increases. So, CDOB in Type 2 also does not work. On the other hand, there is the round trip time delay ($T = T_1 + T_2$) between 'comp 1' and 'comp 2' in Type 3. Therefore, CDOB in Type 3 works. The compensation values which are corresponding to simulation results for case 3(Jitter) are shown in Fig. 6-4(g')–(i'). The difference between 'comp1' and 'comp2' monotonically increases in Type 1 and Type 2. On the other hand, there is the round trip time delay ($T = T_1 + T_2$) between 'comp 1' and 'comp 2' in Type 3. Therefore, CDOB in Type 3 works as same as Case 2.

6.3.3 Discussion

From simulation results in subsection 6.3.2, the steady-state errors decrease in the order of Type 3, Type 2 and Type 1. This subsection analyzes the mechanism of the simulation result. Figure 6-5(b) shows the discrete model of Fig. 6-3(c). The sampler S_{T_c} and the holder H_{T_s} are set before and after the communication channel. Those of them are also set in DOB as S_{T_s} and H_{T_s} . In Fig. 6-5(b), all of them except for the controlled system G , the disturbance d and the output y are handled as discrete models.

Figure 6-5(c) shows the analysis model of Fig. 6-5(b). Here, time delay effects are separated to two parts. One parts are the constant time delay effects such as $e^{-\bar{T}_1 s}$ and $e^{-\bar{T}_2 s}$. \bar{T}_1 and \bar{T}_2 mean constant time delay components of T_1 and T_2 . The other parts are the time varying delay effects as shown in (6.8) and (6.9).

$$n_1^i = e^{-\bar{T}_1 s} - e^{-T_1 s}, \quad (6.8)$$

$$n_2^i = e^{-\bar{T}_2 s} - e^{-T_2 s}. \quad (6.9)$$

Here, $i = 1, 2$. n_1^i and n_2^i are called network noise [86]. Network noise expresses the effect of packet dropouts and jitter.

In type 1, the transfer function from network noise (n) to the output (y) are calculated as shown in (6.10) to (6.15).

$$\frac{y}{n_1^1} = \frac{A_v H_{T_c}}{1 + A_v B_v S_{T_s}^2 H_{T_s}^2 e^{-(T_1+T_2)s}}, \quad (6.10)$$

$$\frac{y}{n_1^2} = \frac{\hat{G} A_v B_v H_{T_s}^2 e^{-(T_1+T_2)s}}{1 + A_v B_v S_{T_s}^2 H_{T_s}^2 e^{-(T_1+T_2)s}}, \quad (6.11)$$

$$\frac{y}{n_2^1} = \frac{\hat{G} A_v B_v S_{T_s} H_{T_s} e^{-T_1 s}}{1 + A_v B_{S_{T_s}}^2 H_{T_s}^2 e^{-(T_1+T_2)s}}, \quad (6.12)$$

$$\frac{y}{n_2^2} = \frac{A_v B_v S_{T_s} H_{T_s} e^{-T_1 s}}{1 + A_v B_v S_{T_s}^2 H_{T_s}^2 e^{-(T_1+T_2)s}}, \quad (6.13)$$

where A_v and B_v are defined as follows.

$$A_v = \frac{G \hat{G}}{\hat{G} - \hat{G} S_{T_s} H_{T_s} L_d + G S_{T_s} H_{T_s} L_d}, \quad (6.14)$$

$$B_v = \frac{C}{1 + \hat{G} C - \hat{G} C S_{T_s}^2 H_{T_s}^2 e^{-(T_1+T_2)s}}. \quad (6.15)$$

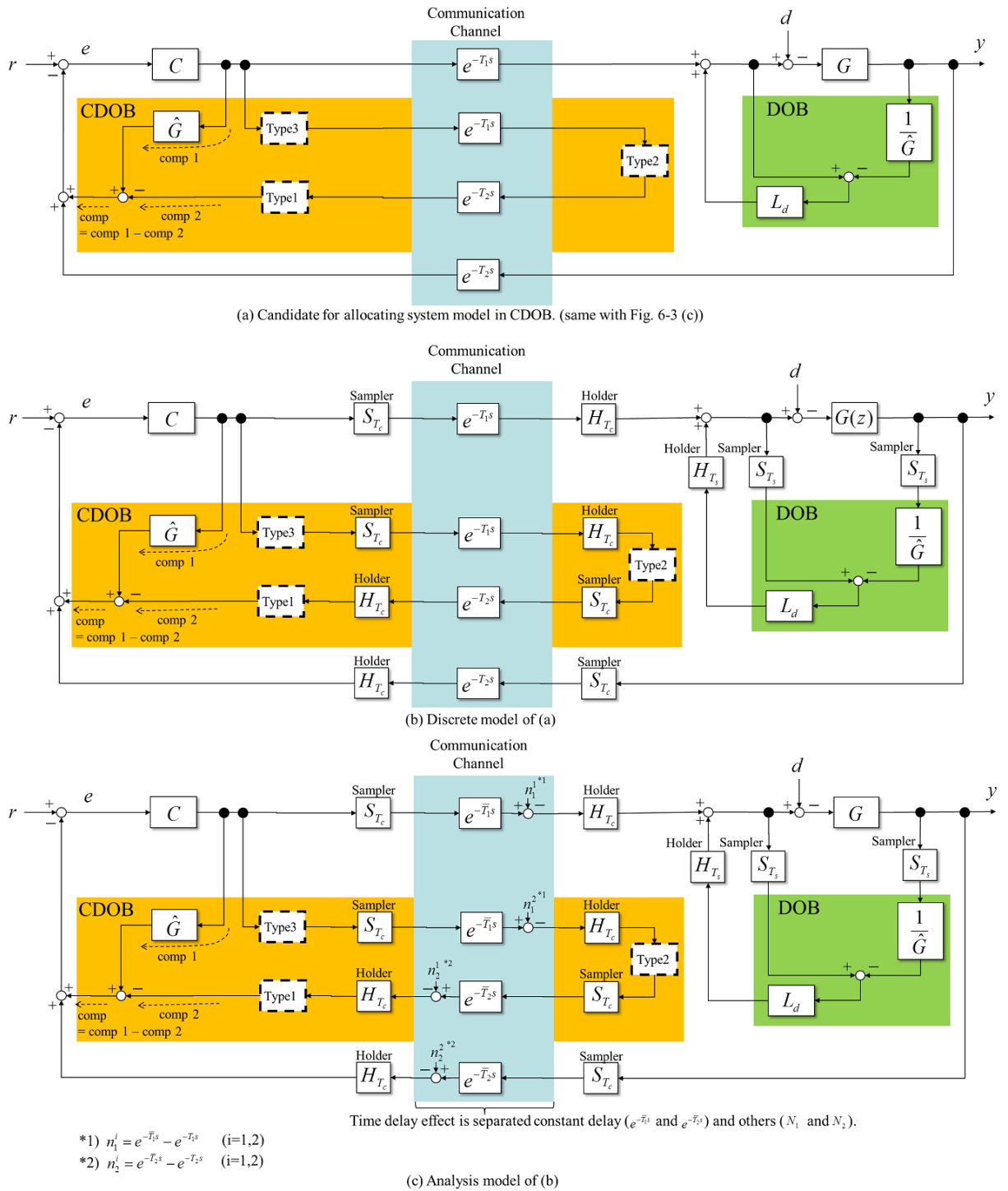


Fig. 6-5: Analysis model.

Laplace domain transfer functions of the sampler and the holder are represented as follows [87].

$$S_{T_c} = \frac{1}{T_c}, \quad (6.16)$$

$$H_{T_c} = \frac{1 - e^{-T_c s}}{s}, \quad (6.17)$$

$$S_{T_s} = \frac{1}{T_s}, \quad (6.18)$$

$$H_{T_s} = \frac{1 - e^{-T_s s}}{s}. \quad (6.19)$$

Here, T_c is the communication period and T_s is the sampling period for the control system.

The Z transformed controller (C), LPF (Ld) and the system model (\hat{G}) are set as follows.

$$C = K_p + K_v \frac{1 - z^{-1}}{T_s}, \quad (6.20)$$

$$Ld = \frac{g}{\frac{1 - z^{-1}}{T_s} + g}, \quad (6.21)$$

$$\hat{G} = \frac{1}{M_n \left(\frac{1 - z^{-1}}{T_s} \right)^2}. \quad (6.22)$$

Laplace transformation of Z operation is shown in (6.23).

$$z = e^{sT_s}. \quad (6.23)$$

Since the controlled system (G) works in continuous model, it is modeled as follows.

$$G = \frac{1}{M_n s^2}. \quad (6.24)$$

In type 2, the transfer function from network noise (n) to the output (y) are calculate as shown in (6.25) to (6.28).

$$\frac{y}{n_1} = \frac{A_v H_{T_c}}{1 + A_v B_v S_{T_s}^2 H_{T_s}^2 e^{-(T_1+T_2)s}}, \quad (6.25)$$

$$\frac{y}{n_1^2} = \frac{A_v B_v H_{T_s}^2 e^{-(T_1+T_2)s}}{1 + A_v B_v S_{T_s}^2 H_{T_s}^2 e^{-(T_1+T_2)s}}, \quad (6.26)$$

$$\frac{y}{n_2^1} = \frac{\hat{G} A_v B_v S_{T_s} H_{T_s} e^{-T_1 s}}{1 + A_v B_v S_{T_s}^2 H_{T_s}^2 e^{-(T_1+T_2)s}}, \quad (6.27)$$

$$\frac{y}{n_2^2} = \frac{A_v B_v S_{T_s} H_{T_s} e^{-T_1 s}}{1 + A_v B_v S_{T_s}^2 H_{T_s}^2 e^{-(T_1+T_2)s}}. \quad (6.28)$$

In type 3, the transfer function from network noise (n) to the output (y) are calculate as shown in (6.29) to (6.32).

$$\frac{y}{n_1^1} = \frac{A_v H_{T_c}}{1 + A_v B_v S_{T_s}^2 H_{T_s}^2 e^{-(T_1+T_2)s}}, \quad (6.29)$$

$$\frac{y}{n_1^2} = \frac{A_v B_v H_{T_s}^2 e^{-(T_1+T_2)s}}{1 + A_v B_v S_{T_s}^2 H_{T_s}^2 e^{-(T_1+T_2)s}}, \quad (6.30)$$

$$\frac{y}{n_2^1} = \frac{A_v B_v S_{T_s} H_{T_s} e^{-T_1 s}}{1 + A_v B_v S_{T_s}^2 H_{T_s}^2 e^{-(T_1+T_2)s}}, \quad (6.31)$$

$$\frac{y}{n_2^2} = \frac{A_v B_v S_{T_s} H_{T_s} e^{-T_1 s}}{1 + A_v B_v S_{T_s}^2 H_{T_s}^2 e^{-(T_1+T_2)s}}. \quad (6.32)$$

From (6.10) to (6.32), gain characteristics of the transfer function of network noise $n(s)$ to $y(s)$ are calculated as shown in Fig. 6-6. Here, each transfer function is calculate as shown in (6.33).

$$\frac{y}{n} = \frac{1}{4} \left(\frac{y}{n_1^1} + \frac{y}{n_1^2} + \frac{y}{n_2^1} + \frac{y}{n_2^2} \right). \quad (6.33)$$

From Fig. 6-6, it is shown that gain characteristics are small in the order of Type 3, Type 2 and Type 1. It coincides with the simulation results. Thus, it is confirmed that decreasing the number of communication channel passages is valid to mitigate the effect of network noise like packet dropouts and jitter. Therefore, Type 3 has the robustness against packet dropouts and jitter.

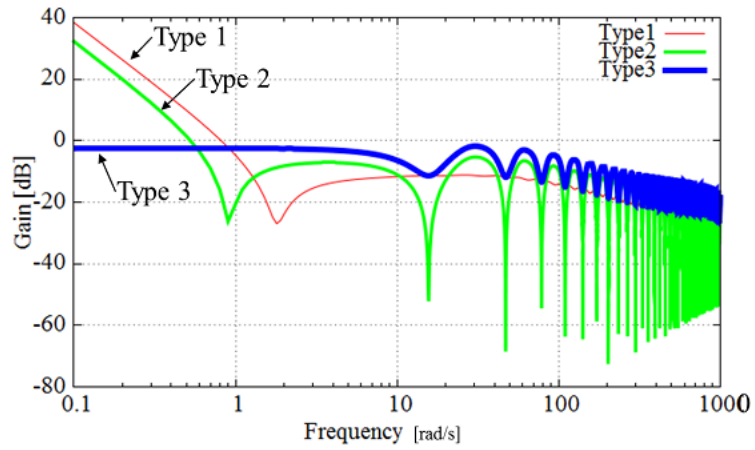


Fig. 6-6: Gain characteristic of transfer function of network noise n to y .

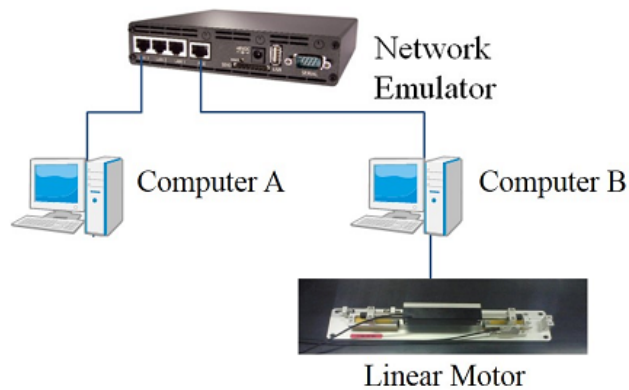


Fig. 6-7: Experimental system.

6.4 Experiment

In this section, experimental results are shown to confirm the validity of the modified structure.

6.4.1 Experimental System

In the experiment, the network emulator is utilized to emulate network conditions which are same to the simulations in subsection 6.3.2. The experimental system is shown in Fig. 6-7. The controller is implemented to 'Computer A' and the current command to the linear motor is transmitted from 'Computer B'. The communication is conducted between 'Computer A' and 'Computer B' by network emulator. The linear motor is equipped with the encoder to sense the position response. Parameters for the experiment are shown in Table 6.2.

Following three kinds of network conditions are considered in experiment. These are same with the simulations which are shown in subsection 6.3.2.

Case 1 : Constant Delay

$$T_1 = T_2 = 200\text{ms}$$

Case 2 : Packet Dropouts

$T_1 = T_2 = 200\text{ms}$. Packet dropouts are occurred during 0.5s to 0.6s. Each part receives same data during that period.

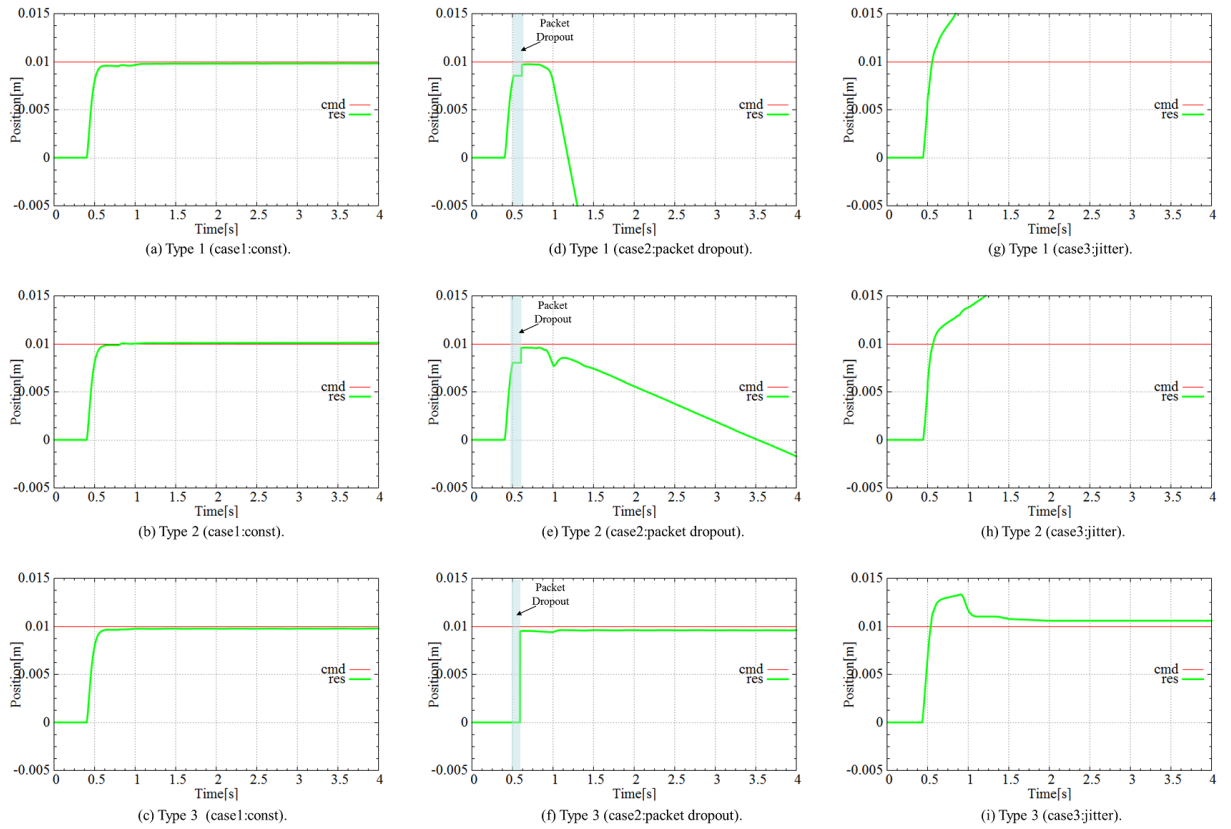


Fig. 6-8: Experimental results.

Case 3 : Jitter

$T_1 = T_2 = 200\text{ms} \pm 30\text{ms}$. Here, T_1 is time delay from the 'Computer A' to the 'Computer B'. T_2 is time delay from the 'Computer B' to the 'Computer A'. The sampling period (T_s) is 0.001s and the communication period (T_c) is 0.001s. When the packet dropouts are occurred in case 2, the zero-order hold is conducted in the receiving side. In case 3, if the several packet data is received, the latest packet data is utilized.

6.4.2 Experimental Result

Figure 6-8 shows the experimental results. Figure 6-8 shows the position response of each case. 'cmd' shows the position command and 'res' shows the position response which is received in 'Computer A'. Experimental results for case 1(Constant Delay) are shown in Fig. 6-8(a)–(c). Even though there exists

the model error between the mass of the controlled system (M) and the mass model (M_n) of the system model, there are no steady-state error in all cases. Experimental results for case 2(Packet Dropouts) are shown in Fig. 6-8(d)–(f). The position response is same in all cases before the packet dropouts occurs. After the packet dropouts, steady-state errors become large in the order of Type 1, Type 2 and Type 3. There are large steady-state errors in Type 1 and Type 2. On the other hand, the steady-state error is small in Type 3 and the position response tracks the position command in Type 3. Experimental results for case 3(Jitter) are shown in Fig. 6-8(g)–(i). Steady-state errors become large in the order of Type 1, Type 2 and Type 3. There are large steady-state errors in Type 1 and Type 2. On the other hand, the steady-state error is small in Type 3 and the position response tracks the position command in Type 3. Therefore, it is confirmed that Type 3 has the robustness against packet dropouts and jitter.

6.5 Summary

In this chapter, considering unstable time delay, the structure of CDOB has been modified. As the nonlinear effect like communication packet dropouts or jitter can deteriorate the total control system, a case study has been accomplished considering locations of the system model in the CDOB. Then, the more robust CDOB structure against packet dropouts and jitter has been designed. The validity of the modified structure has been shown by experimental results.

Chapter 7

Bilateral Teleoperation System with Time Delay

7.1 Background and Outline

Recent advances in control theories opened the way towards extensions of human manipulation capabilities [88]. Benefiting from the advantages of communication technologies and bilateral control theories [89], a operation over a remote environment (i.e. teleoperation) becomes one of the most prominent research topics. Bilateral teleoprations systems enable human being to feel a tactile sensation of environment at a remote sight through a master robot and a slave robot. Human beings can manipulate a slave robot in sky [90], space [91], water, nuclear plants and so on, as if they are in the remote place. Recently, applications of these technology are expanded to medical fields [92], communication fields [93] and industry fields [94].

There are some performance indices in bilateral control systems [95–97]. One of the performance indices of bilateral control systems is “transparency” [13]. High transparency means that the force control and the position control are realized perfectly both in a master robot and a slave robot. Transmission characteristics of force and position information between a master robot and a slave robot are confirmed by using hybrid matrices [65]. Furthermore, there are two evaluation indices for bilateral control systems based on transparency, which are “reproducibility “ and “operationality ” [44]. Reproducibility shows how precisely environmental impedances are reproduced in the master side. Operationality shows how smoothly the operator manipulates the master robot.

In real teleoperations, human operator manipulates a master robot while watching video images which

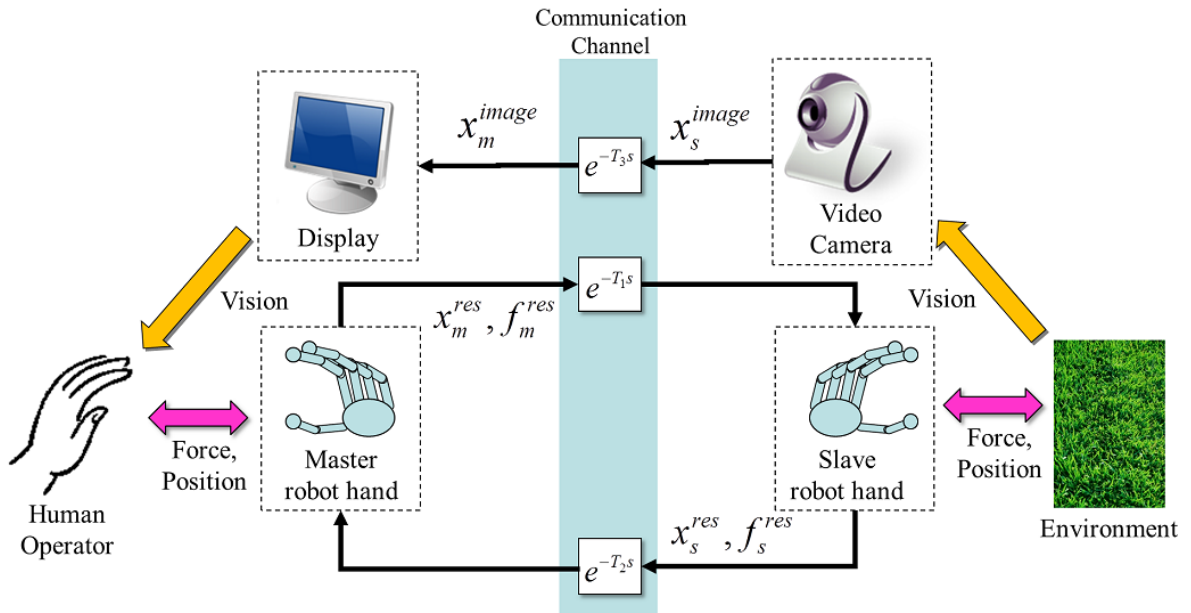


Fig. 7-1: Overview of teleoperation system with haptic and visual sense feedback.

are sent from remote environment [98, 99]. Figure 7-1 shows the overview of teleoperation systems with haptic and visual sense feedback. Two robots are considered in bilateral control systems, a master robot which is manipulated by human operators and a slave robot which contacts remote environment. Human operator watches a video image of remote environment. T_1 and T_2 denote time delay of a haptic information (position and force) between the master robot and the slave robot. T_3 denotes time delay of a video image from the slave robot to the master robot.

If the ideal bilateral control is realized in this teleoperation system, human operators can sense environmental impedances. Haptic information will prevent from breaking remote environment and human operators can achieve more dexterous tasks. However, the presence of time delay between a master robot and a slave robot makes the design of this system challengeable. Firstly, time delay seriously deteriorates the performance and possibly makes the bilateral control system unstable [100]. Secondly, the synchronization with haptic and visual sense should be considered.

The passivity based approach is very common to stabilize the two-channel bilateral control system [25]. This scheme restricts output flows smaller than input flows by using wave variables [101]. Time delay compensation method is also useful to treat the time delay system without restricting output flows

[74]. Smith predictor is often utilized to compensate communication time delay with a time delay model [78]. But, time delay in the communication system is varying and unpredictable. A disturbance observer is utilized to deal with time delay systems. CDOB has been proposed to compensate the time delay effect without a time delay model [102]. The effectiveness of the time delay compensation by CDOB to the acceleration based four-channel bilateral control system is confirmed experimentally so far. However, the force control is not stabilized. To stabilize the force control in the bilateral control system, the high frequency domain damping [103] and the delayed force feedback structure have been proposed.

To overcome the destabilization from time delay, model-free time delay compensator has been proposed. The proposed compensator does not utilize the time delay model and the plant model, but the position control and the force control are stabilized.

For synchronizing haptic and visual sense, the bilateral control system which utilizes round-trip time delayed information has been proposed. By utilizing the proposed method, reproducibility is well improved and the gain of the environmental impedance is reproduced in the all frequency area.

Furthermore, to attain almost same performance with no time delay system, the allocations of HPF are studied. HPF is implemented to remove the undesirable operational force in the low frequency area. By allocating HPF correctly, operability is improved with keeping the stability and reproducibility.

The composition of this chapter is described as follows. In section 7.2, the time delay problem in the bilateral control system is introduced. The time delay compensations with model-based compensator are shown in 7.3. The one is CDOB and the other is the delayed force feedback structure. By utilizing the latter method, the position control and the force control of the bilateral control system are stabilized. But, this method needs time delay information. Thus, model-free time delay compensator is proposed in 7.4. The proposed compensator does not utilize the time delay model and the plant model, but the position control and the force control of the bilateral control system are stabilized. In section 7.5, a bilateral control system to synchronize haptic and visual sense is proposed. By utilizing the proposed method, reproducibility is also improved and the gain of the environmental impedance is reproduced in the all frequency area. In section 7.6, allocations of HPF are studied to attain the almost same performance with no time delay system. By allocating HPF correctly, operability is improved with keeping the stability and reproducibility. Finally, this chapter is summarized in section 7.7.

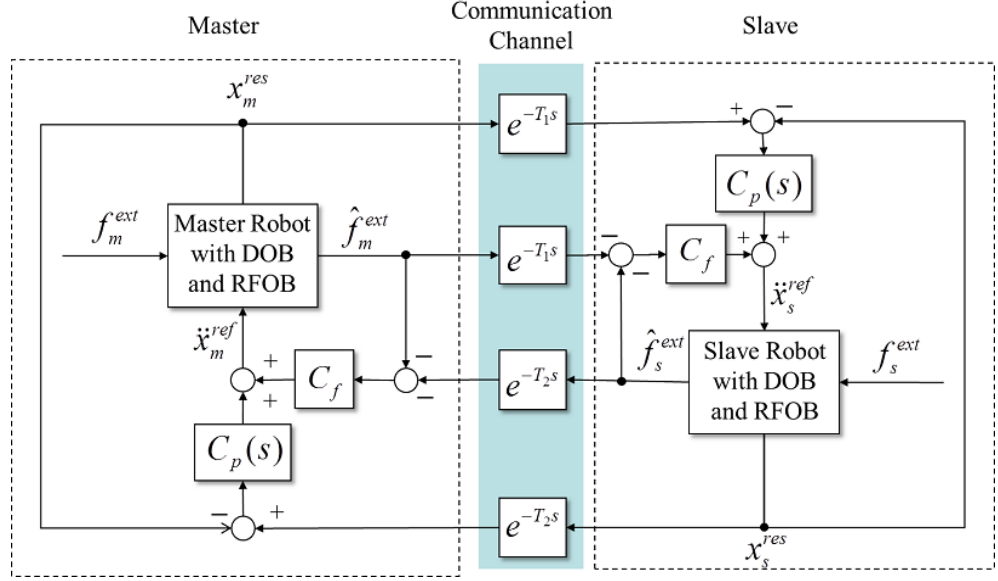


Fig. 7-2: Four-channel bilateral control system with time delay.

7.2 Time Delay Problem

Figure 7-2 shows the acceleration based four-channel bilateral control system with time delay. DOB and RFOB are implemented in the master robot and the slave robot for the robust acceleration control. In Figure 7-2, x_m^{res} , x_s^{res} , \hat{f}_m^{ext} and \hat{f}_s^{ext} are the position response of the master robot, the position response of the slave robot, the reaction force added to the master robot and the reaction force added to the slave robot, respectively. The reaction force added to each robot \hat{f}_m^{ext} and \hat{f}_s^{ext} are estimated using not force sensors but RFOB. T_1 denotes time delay from the master robot to the slave robot and T_2 denotes time delay from the slave robot to the master robot. C_p is a position controller and C_f is a fore controller. time delay T_1 and T_2 destabilize the control system and deteriorate the performance. As performance indexes for bilateral control systems, "reproducibility" (P_r) and "operationality" (P_o) are useful [44]. These indexes are understood intuitively. Reproducibility shows how precisely the environmental impedance is reproduced in the master side. Operationality shows how smoothly the operator manipulates the master robot. Thus, perfect transparency is realized when P_r becomes 1 and P_o becomes 0. Figure 7-3 shows reproducibility and operationality of the four-channel bilateral control system. Here, $T = T_1 = T_2$. The four-channel bilateral control system has the good performance in the case of no time delay. Reproducibility is 1 in the all frequency area and operationality is small in the low

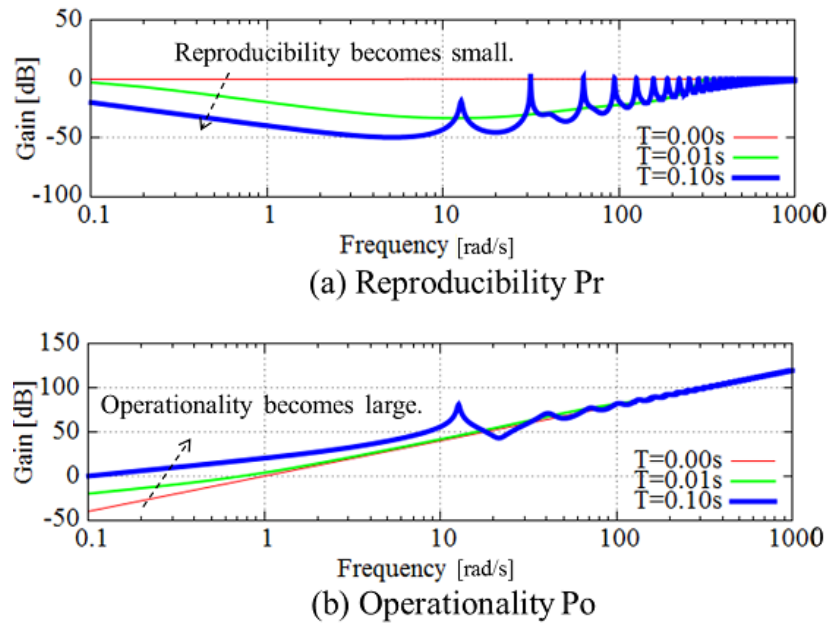


Fig. 7-3: Performance deterioration from time delay.

frequency area, However, reproducibility becomes small and operationality becomes large as time delay is increasing. Thus, the performance is deteriorated by time delay.

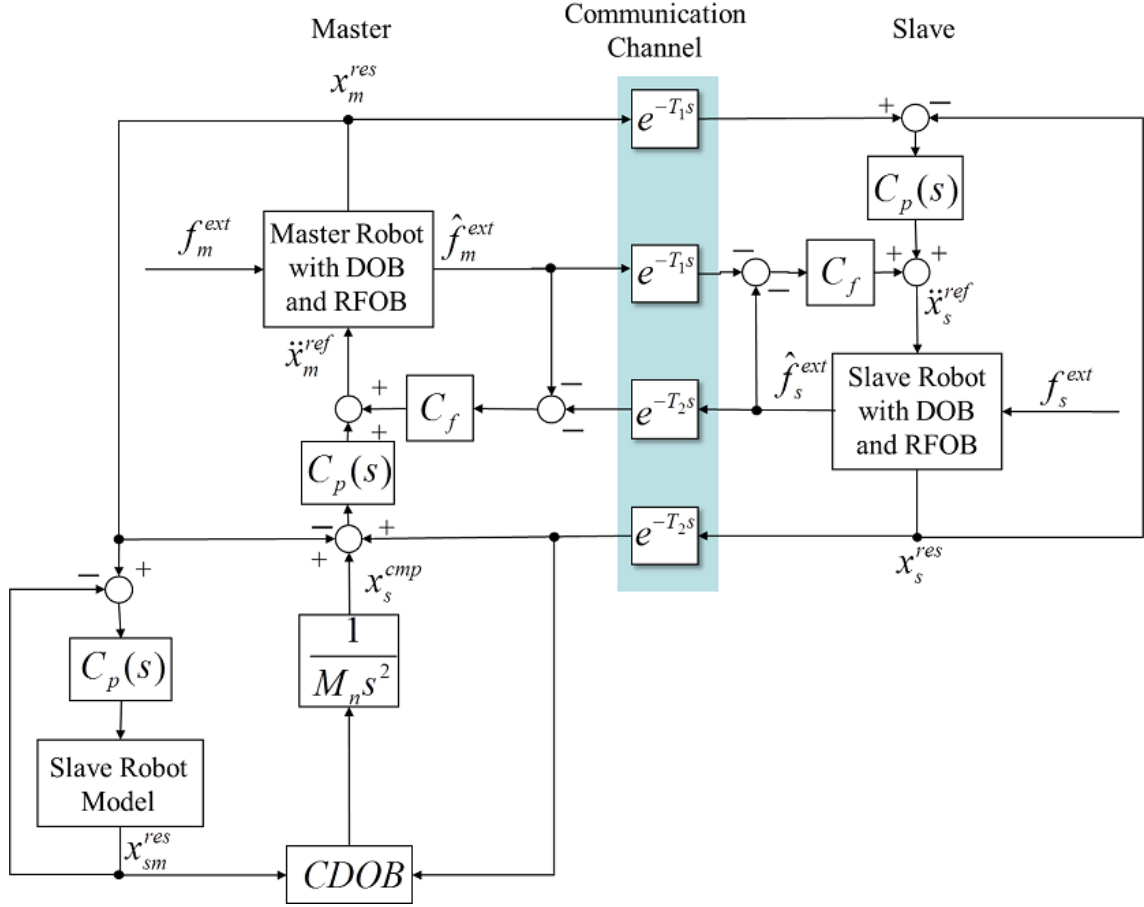


Fig. 7-4: Block diagram of four-channel structure with CDOB.

7.3 Time Delay Compensation with Model-Based Compensator

In this section, time delay compensations with model-based compensator are shown. The one is CDOB and the other is the delayed force feedback structure.

7.3.1 Communication Disturbance Observer

The four-channel control system with CDOB compensation is shown in Fig. 7-4. If cut-off frequencies of LPF in DOB, RFOB and CDOB approach infinity and time delay is $T = T_1 = T_2$, the acceleration response of the master robot in Fig. 7-4 is expressed as follows.

$$s^2 x_m^{res} = -C_f(\hat{f}_s^{ext} e^{-Ts} + \hat{f}_m^{ext}) + C_p(s)(x_s^{res} e^{-Ts} - x_m^{res} + x_s^{cmp}), \quad (7.1)$$

$$x_s^{cmp} = x_{sm}^{res} - x_s^{res} e^{-Ts}, \quad (7.2)$$

$$s^2 x_{sm}^{res} = C_p(s)(x_m^{res} - x_{sm}^{res}). \quad (7.3)$$

Here, DOB works ideally and the disturbance force including the parameter fluctuation is suppressed completely, i. e. $x_m^{res} = \ddot{x}_m^{ref}/s^2$ and $x_s^{res} = \ddot{x}_s^{ref}/s^2$. Thus, equation (7.1)-(7.3) do not include dynamics such as the mass variable. Equation (7.1)-(7.3) are not realized in the high-frequency area above the cut-off frequency of LPF in DOB (g_d). In usual cases, g_d can be set large enough, so this assumption is negligible in practical cases. From equation (7.1) to (7.3), (7.4) is derived.

$$\left(1 + \frac{C_p(s)}{s^2 + C_p(s)}\right) s^2 x_m^{res} = -C_f(\hat{f}_s^{ext} e^{-Ts} + \hat{f}_m^{ext}). \quad (7.4)$$

By the compensation of CDOB, the position control of the master robot is removed if the gain of the position control system ($C_p(s)$) becomes infinity. On the other hand, the acceleration response of the slave robot in Fig. 7-4 is expressed as follows.

$$s^2 x_s^{res} = -C_f(\hat{f}_m^{ext} e^{-Ts} + \hat{f}_s^{ext}) + C_p(s)(x_m^{res} e^{-Ts} - x_s^{res}).$$

It is shown that this bilateral control system is almost same to the three-channel bilateral control system [103], [104].

7.3.2 Stability Analysis in Modal Space

In this subsection, modal spaces for the bilateral control system are generalized. And, the stability of the conventional method is explained by using those modal spaces.

Modal Space for Bilateral Control

The acceleration based bilateral control is achieved in orthogonally crossed two virtual modal spaces : a force controller in the common modal space and a position controller in the differential modal space [31]. The force in the common mode f_c and the position in the differential mode x_d are defined as follows.

$$f_c = \hat{f}_m^{ext} + \hat{f}_s^{ext}, \quad (7.5)$$

$$x_d = x_m - x_s. \quad (7.6)$$

Equation (7.7) is defined to control the acceleration of the common mode and the differential mode.

$$\begin{bmatrix} \ddot{x}_c \\ \ddot{x}_d \end{bmatrix} = \begin{bmatrix} 1 & 1 \\ 1 & -1 \end{bmatrix} \begin{bmatrix} \ddot{x}_m \\ \ddot{x}_s \end{bmatrix}. \quad (7.7)$$

When perfect transparency is achieved, (7.8) and (7.9) are realized.

$$f_m^{ext} = -f_s^{ext}, \quad (7.8)$$

$$x_m = x_s. \quad (7.9)$$

To realize (7.8) and (7.9), the force response in the common mode and the position response in the differential mode should be controlled to be 0. Thus, the force controller in the common mode and the position controller in the differential mode are designed as shown in (7.10) and (7.11).

$$\ddot{x}_c^{ref} = -C_f(\hat{f}_m^{ext} + \hat{f}_s^{ext}), \quad (7.10)$$

$$\ddot{x}_d^{ref} = C_p(s)(x_m^{res} - x_s^{res}). \quad (7.11)$$

Stability in Modal Space

By utilizing (7.4), (7.5) and (7.7), block diagrams in the differential mode and the common mode are derived as shown in Fig. 7-5(a) and (c). z_h means the human impedance and z_e means the environmental impedance. In Fig. 7-5(a) and (c), DOB works ideally and the disturbance force including the parameter fluctuation is suppressed completely, i. e. $x_m^{res} = \ddot{x}_m^{ref}/s^2$ and $x_s^{res} = \ddot{x}_s^{ref}/s^2$. Thus, equations of Fig. 7-5(a) and (c) do not include dynamics such as the mass variable. Figure 7-5(a) and (c) are not realized in the high-frequency area above the cut-off frequency of LPF in DOB (g_d). In usual cases, g_d can be set large enough, so this assumption is negligible in practical cases.

From Fig. 7-5 (a), there exists no time delay element in the feedback loop. Then, the position control is stable in the conventional method. From Fig. 7-5 (c), there exists time delay elements in the feedback loop. Therefore, the force control is not stable in the conventional method.

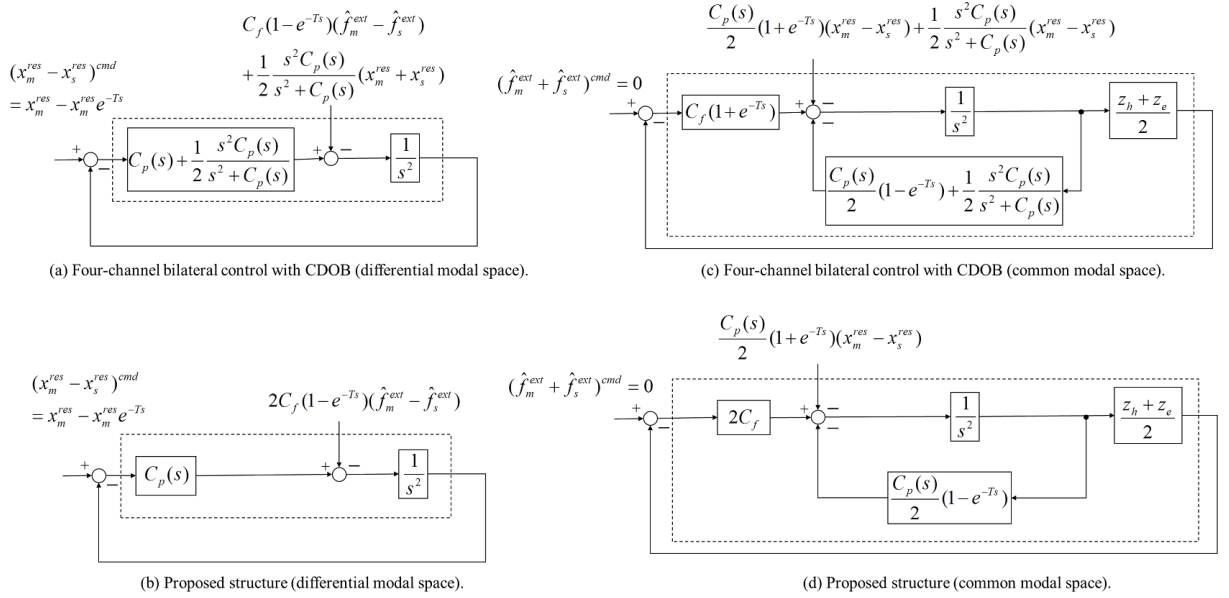


Fig. 7-5: Block diagram in modal space.

$$\begin{aligned}
 s^2 \left(x_m^{res} + \frac{C_p(s)}{s^2 + C_p(s)} x_m^{res} + x_s^{res} \right) &= - \underbrace{C_f(\hat{f}_s^{ext} e^{-Ts} + \hat{f}_m^{ext})}_{\text{master side force controller}} - \underbrace{C_f(\hat{f}_m^{ext} e^{-Ts} + \hat{f}_s^{ext})}_{\text{slave side force controller}} \\
 &\quad + C_p(s)(x_m^{res} e^{-Ts} - x_s^{res}) \\
 &= -C_f(1 + e^{-Ts})(\hat{f}_s^{ext} + \hat{f}_m^{ext}) \\
 &\quad + C_p(s)(x_m^{res} e^{-Ts} - x_s^{res}). \tag{7.12}
 \end{aligned}$$

7.3.3 Stability Improved Bilateral Control Structure

In this subsection, the stability improved bilateral control structure is derived from the modal space analysis. Moreover, the stability and the the performance are analyzed.

Proposed Structure

In the conventional method, the acceleration response of the common mode is derived as (7.12) from (7.4) and (7.5). By utilizing the delayed master and slave force responses, time delayed elements exist in the feedback loop of the common mode as shown in Fig. 7-5(c). This is the unavoidable characteristic in the bilateral control system with time delay.

In the proposed structure, time delay elements in the common modal space are tried to be deleted by changing the acceleration reference of the master robot and the slave robot. To delete time delay elements in the common modal space, the acceleration reference of the master robot and the slave robot are set as shown in (7.13) and (7.14) in the proposed structure.

$$s^2 x_m^{ref} = -C_f(\hat{f}_s^{ext} e^{-T_2 s} + 2\hat{f}_m^{ext} - \hat{f}_m^{ext} e^{-\hat{T}_2 s}), \tag{7.13}$$

$$s^2 x_s^{ref} = -C_f(\hat{f}_m^{ext} e^{-T_1 s} + 2\hat{f}_s^{ext} - \hat{f}_s^{ext} e^{-\hat{T}_1 s}) + C_p(s)(x_m^{res} e^{-Ts} - x_s^{res}). \tag{7.14}$$

In equation (7.13) and (7.14), time delay from the master robot to the slave robot (T_1) and time delay from the slave robot to the master robot (T_2) are estimated as \hat{T}_1 and \hat{T}_2 . These estimated time delay (\hat{T}_1 and \hat{T}_2) are utilized to add an artificial minor force feedback with time delay ($\hat{f}_m^{ext} e^{-\hat{T}_2 s}$ or $\hat{f}_s^{ext} e^{-\hat{T}_1 s}$) in the acceleration reference of the master robot and the slave robot. The advantages of setting the acceleration reference as shown in (7.13) and (7.14) is that the acceleration response in the common modal space does not include time delay elements as shown in equation (7.15). In equation (7.15), time delay is supposed to be $T = T_1 = T_2 = \hat{T}_1 = \hat{T}_2$ and DOB works ideally, i. e. $x_m^{res} = \ddot{x}_m^{ref} / s^2$ and

$$\begin{aligned}
 s^2 (x_m^{res} + x_s^{res}) &= \underbrace{-C_f(\hat{f}_s^{ext} e^{-Ts} + 2\hat{f}_m^{ext} - \hat{f}_m^{ext} e^{-Ts})}_{\text{master side force controller}} - \underbrace{C_f(\hat{f}_m^{ext} e^{-Ts} + 2\hat{f}_s^{ext} - \hat{f}_s^{ext} e^{-Ts})}_{\text{slave side force controller}} \\
 &\quad + C_p(s)(x_m^{res} e^{-Ts} - x_s^{res}) \\
 &= -2C_f(\hat{f}_s^{ext} + \hat{f}_m^{ext}) + C_p(s)(x_m^{res} e^{-Ts} - x_s^{res}), \tag{7.15}
 \end{aligned}$$

$x_s^{res} = \ddot{x}_s^{ref}/s^2$. In equation (7.13) and (7.14), $\hat{f}_m^{ext} - \hat{f}_m^{ext} e^{-\hat{T}_2 s}$ or $\hat{f}_s^{ext} - \hat{f}_s^{ext} e^{-\hat{T}_1 s}$ are enough to eliminate time delay elements. The added \hat{f}_m^{ext} or \hat{f}_s^{ext} works to realize the three-channel control system in the case of no time delay. If the time delay is zero, $\hat{f}_m^{ext} - \hat{f}_m^{ext} e^{-\hat{T}_2 s}$ or $\hat{f}_s^{ext} - \hat{f}_s^{ext} e^{-\hat{T}_1 s}$ in equation (7.13) and (7.14) becomes 0. Then, the acceleration references become as follows.

$$s^2 x_m^{ref} = -C_f(\hat{f}_s^{ext} + \hat{f}_m^{ext}), \tag{7.16}$$

$$s^2 x_s^{ref} = -C_f(\hat{f}_m^{ext} + \hat{f}_s^{ext}) + C_p(s)(x_m^{res} e^{-Ts} - x_s^{res}). \tag{7.17}$$

Thus, the added \hat{f}_m^{ext} or \hat{f}_s^{ext} is needed for using this control system in both conditions, i.e. no time delay and some time delay. Here, the time delay estimation means the calculation of time delay between the master robot and the slave robot. This is different from the time delay estimation (TDE) which is a model-independent simple dynamics estimation technique [105], [106].

From equations (7.13) and (7.14), the proposed structure is implemented as shown in Fig. 7-6. In Fig. 7-6, the bended arrows at $1 - e^{-\hat{T}_1 s}$ or $1 - e^{-\hat{T}_2 s}$ mean that time delay are estimated as \hat{T}_1 or \hat{T}_2 by the time stamp of the master robot and the slave robot. Then, the force control is compensated as shown in the dotted area in Fig. 7-6. The estimating time delay by using the time stamp faces the problem of the clock difference value between the master and the slave robot. This section supposed that the problem of the clock difference is solved by using reference papers [107] or [108].

If, the time delay is $T = T_1 = T_2 = \hat{T}_1 = \hat{T}_2$ and DOB works ideally, i. e. $x_m^{res} = \ddot{x}_m^{ref}/s^2$ and $x_s^{res} = \ddot{x}_s^{ref}/s^2$, the block diagram in the differential mode and the common mode are derived as shown in Fig. 7-5(b) and (d). From Fig. 7-5(b) and (d), it is shown that time delay element does not exist in the main loop not only in the differential mode but also in the common mode. Thus, it is shown that the stability is improved in the proposed structure.

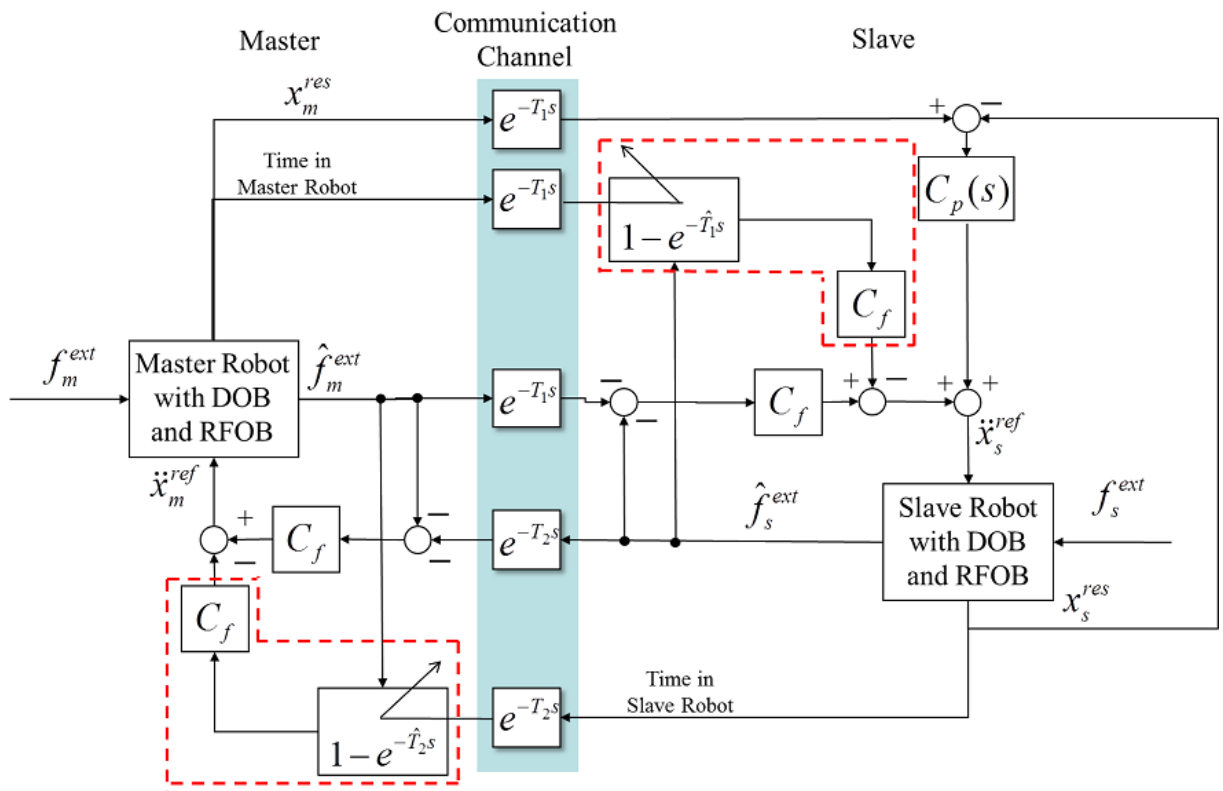


Fig. 7-6: Block diagram of the proposed structure.

Table 7.1: Parameters for analysis and experiment

Position feedback gain	K_P	900	
Velocity feedback gain	K_V	60	
Force feedback gain	K_f	0.5	
Cut-off frequency of DOB	g_{dis}	500	rad/s
Cut-off frequency of RFOB	g_{reac}	500	rad/s
Cut-off frequency of CDOB	g_{cdob}	500	rad/s
Human impedance	Z_h	850+50s	
Environmental impedance	Z_e	30000+50s	
Nominal mass	M_n	0.5	kg
Thrust coefficient	K_{tn}	32.5	N/A
Time delay(for analysis)	T	0.1	s
Sampling time(for experiment)	T_s	0.001	s

7.3.4 Discussion of Stability and Performance

In this subsection the stability and the performance are analyzed numerically. Parameters for analyses are shown in Table 7.1.

Stability Analysis in Modal Space

The stability analysis has been conducted in modal spaces such as the differential mode and the common mode. This is because the position control and the force control of the acceleration based bilateral control system are implemented in modal spaces. However, analyses in modal spaces assume constant time delay and $T_1 = T_2$. In the cases with time-varying delay, those conditions are not usually satisfied. Therefore, the stability under constant delay and $T_1 = T_2$ is analyzed by using Nyquist diagrams in this subsection. The stability under time-varying delay or $T_1 \neq T_2$ is demonstrated by experimental results in section 7.3.5.

Nyquist diagrams for the differential modal space and the common modal space are shown in Fig. 7-7. In Fig. 7-7, dotted arrow shows the direction of the plot line which is corresponding with the angular frequency from 0 to infinity. Here, the open-loop transfer function for each control method is shown as the dotted line in Fig. 7-5.

From Fig. 7-7(a) and (b), it is shown that position control of the conventional method and the proposed method are stable. Figure 7-7(c) and (d) show that the force control of the conventional method is not

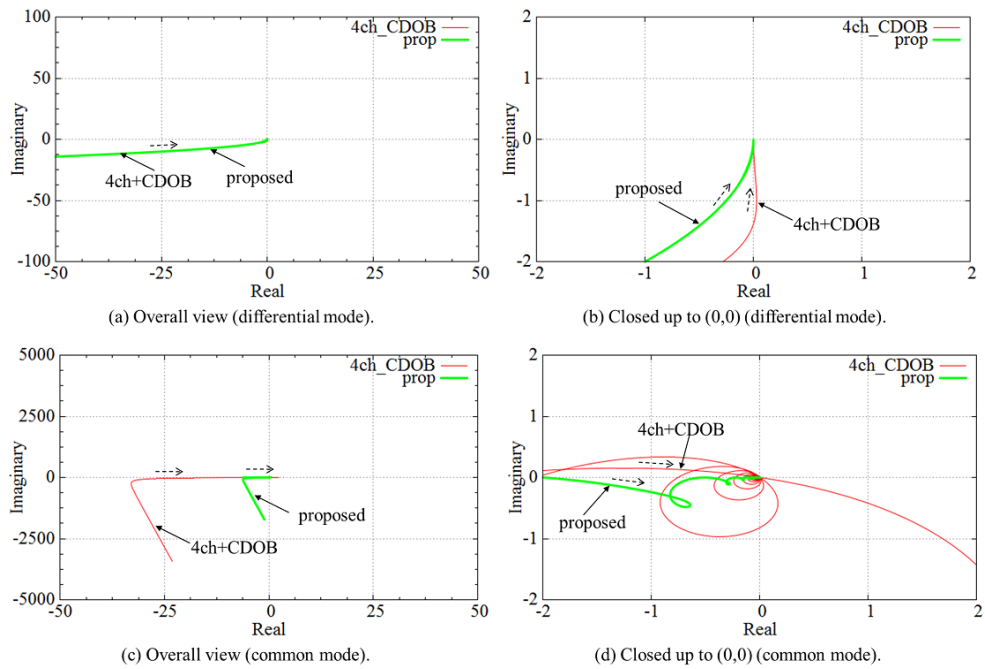


Fig. 7-7: Nyquist diagram.

stable, but the force control of the proposed method is stable. In Fig. 7-5(d), e^{-Ts} is still included in inner loop. However, considering the total open-loop transfer function which is shown as dotted line in Fig. 7-5(d), the force control of the proposed method is stable as shown in Fig.7-7(d).

For analyzing the stability of the common modal space in more general cases, the parametric study for the Nyquist diagram of the common modal space has been conducted. Fig. 7-8 shows the parametric study results. In Fig. 7-8, time delay, human / environmental impedances, a position control gain and a force control gain are parameterized. From Fig. 7-8, it is shown that the proposed method is always stable. Figure 7-8(a) shows that the conventional method is not stable in all cases of time delay. From Fig. 7-8(b), the conventional method can be stabilized by setting the environmental impedance to nearly zero which is close to the free motion. Figure 7-8(c) shows that stability of the conventional method is improved by increasing the position feedback gain. Figure 7-8(d) shows that stability of the conventional method is improved by decreasing the force feedback gain. Thus, increasing the position feedback gain or decreasing the force feedback gain are needed to stabilize the conventional control system. However, increasing the position feedback gain from $K_p = 1600.0$, $K_v = 80.0$ possibly makes the control system unstable due to the signal noise in practical cases. Decreasing the force feedback gain from $K_f = 0.25$ makes the contact with environment unstable in practical cases. Thus, the conventional method is not stabilized by tuning of the feedback gain. And, it is shown that the stability is overwhelmingly improved by using the proposed method.

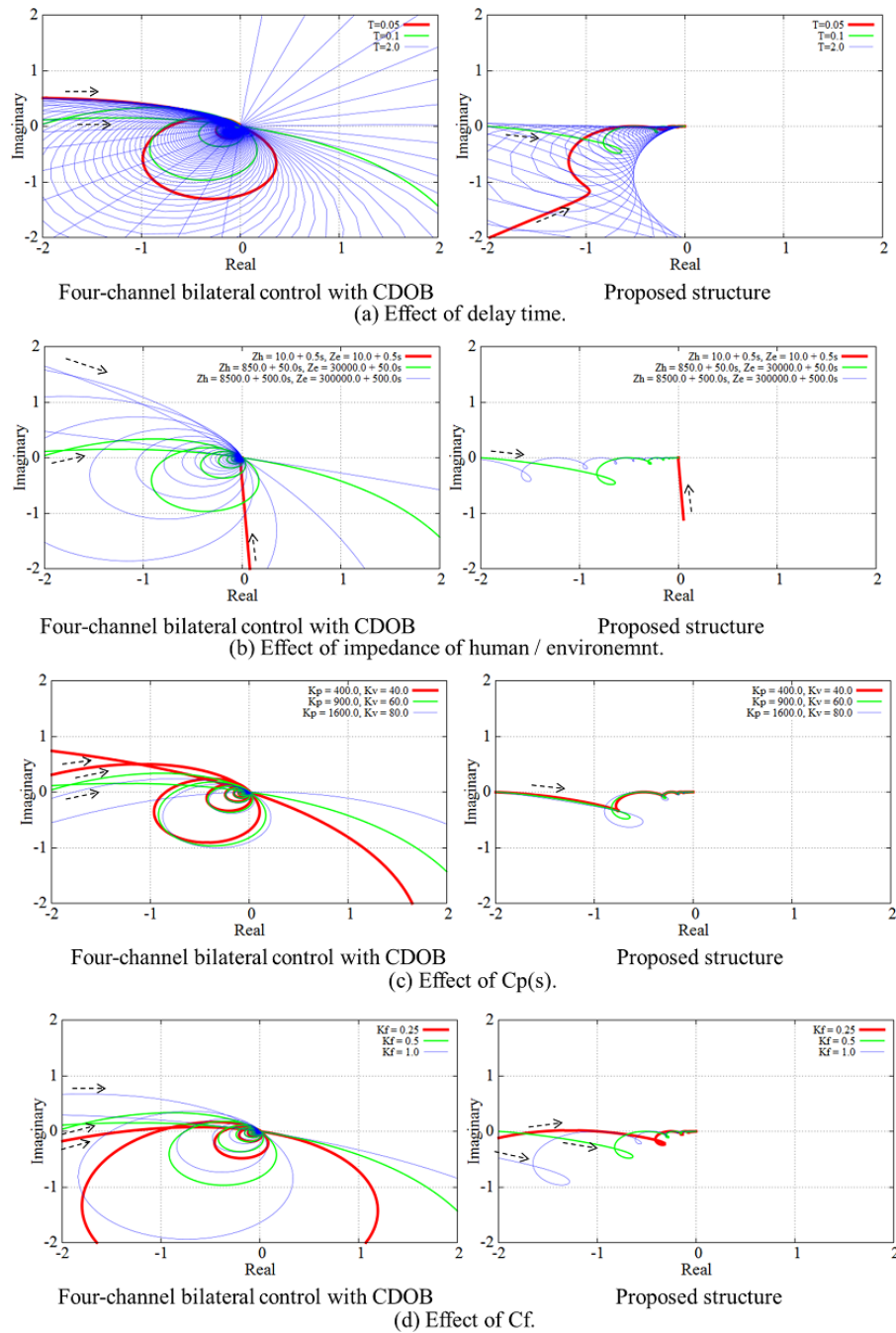


Fig. 7-8: Parametric study results of Nyquist diagram of common modal space.

Performance Analysis

For evaluating the performance of the bilateral control system, Hybrid parameters are utilized [65]. Equation (7.18) shows the definition of hybrid parameters.

$$\begin{bmatrix} f_m^{ext} \\ -x_s \end{bmatrix} = \begin{bmatrix} H_{11} & H_{12} \\ H_{21} & H_{22} \end{bmatrix} \begin{bmatrix} x_m \\ -f_s^{ext} \end{bmatrix}. \quad (7.18)$$

Perfect transparency as shown in (7.8) and (7.9) is achieved if $H_{11} = H_{22} = 0$ and $H_{12} = -H_{21} = 1$. The hybrid parameters for the conventional four-channel control structure with CDOB compensation are derived as (7.19) to (7.22) from (7.4) and (7.5).

$$H_{11} = -\frac{s^2}{C_f} \frac{s^2 + 2C_p(s)}{s^2 + C_p(s)}, \quad (7.19)$$

$$H_{12} = e^{-Ts}, \quad (7.20)$$

$$H_{21} = -e^{-Ts} \frac{(s^2 + C_p(s))^2 + C_p(s)s^2}{(s^2 + C_p(s))^2}, \quad (7.21)$$

$$H_{22} = \frac{C_f^2(e^{-2Ts} - 1)}{s^2 + C_p(s)}. \quad (7.22)$$

The hybrid parameters for the proposed structure are derived as (7.23) to (7.26) from (7.13) and (7.14).

$$H_{11} = -\frac{s^2}{C_f(2 - e^{-Ts})}, \quad (7.23)$$

$$H_{12} = \frac{e^{-Ts}}{2 - e^{-Ts}}, \quad (7.24)$$

$$H_{21} = -\frac{e^{-Ts}}{s^2 + C_p(s)} \left(\frac{s^2}{2 - e^{-Ts}} + C_p(s) \right), \quad (7.25)$$

$$H_{22} = \frac{C_f e^{-Ts}}{s^2 + C_p(s)} \left(\frac{2}{e^{-Ts}} - 1 - \frac{e^{-Ts}}{2 - e^{-Ts}} \right). \quad (7.26)$$

From (7.19) to (7.26), gain characteristics of hybrid parameters H_{11} , H_{12} , H_{21} and H_{22} are calculated as shown in Fig. 7-9. From Fig. 7-9(a), it is shown that both methods have small gains in H_{11} in the low-frequency area. However, they have the large gains in the high-frequency area. The force feedback gain C_f has to be set larger values to suppress the gain of H_{11} . Figure 7-9(b) and (c) show that the transmitted position and force bandwidths are restricted in the proposed control system. Figure 7-9(d) shows that condition of $|H_{22}| = 0$ is almost satisfied by using both methods. The position feedback gain $C_p(s)$ has to be set to a larger value to suppress the gain of H_{22} . Thus, considering H_{12} and H_{21} parameter, the performance of the proposed method is a little bit worse than the conventional method.

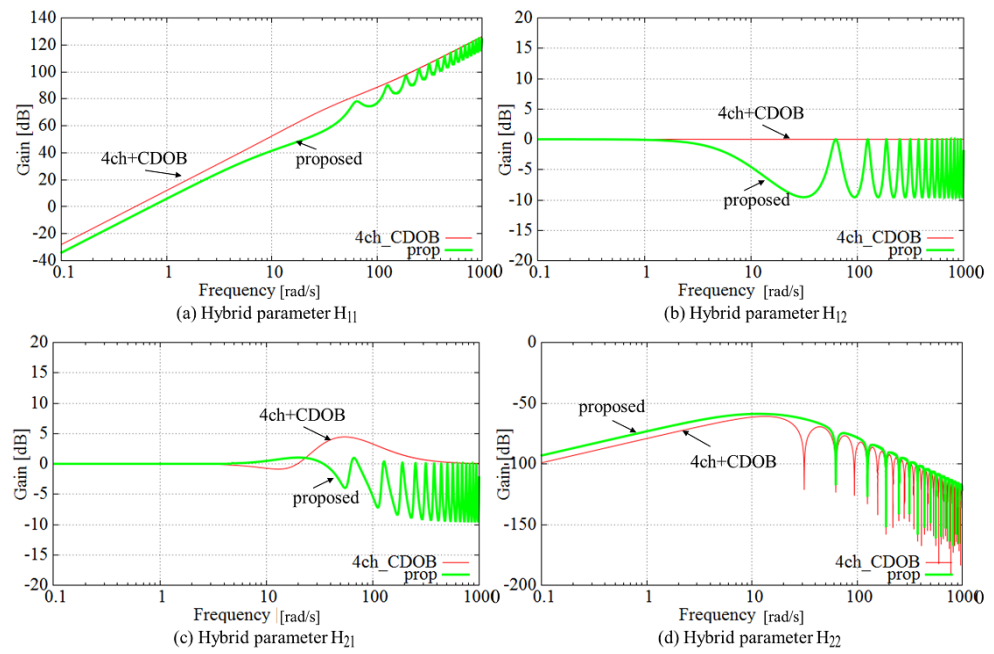


Fig. 7-9: Gain characteristics of hybrid parameter.

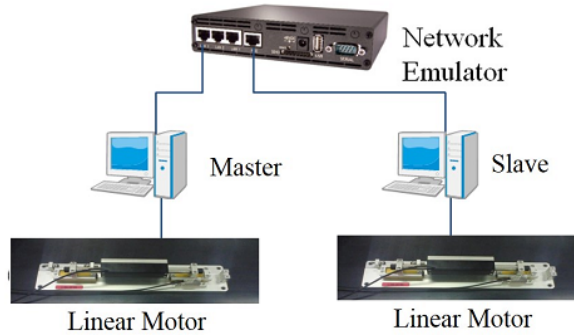


Fig. 7-10: Experimental system.

7.3.5 Experiment

. In this subsection, experimental results are shown to confirm the validity of the proposed structure.

Experimental System

Figure 7-10 shows the experimental system. Time delay is produced by the network emulator. The master and the slave system consist of 1-DOF robots. The robot consist of the linear motor and the encoder. A human operator manipulates the master side linear motor, and the slave side linear motor contacts with environment. The resolution of the encoder is $0.1 \mu\text{m}$. Control parameters used in the experiments are shown in Table 7.1. In the experiment, following kinds of time delay: constant delay and time varying delay are considered.

Case 1 $T_1 = T_2 = 100\text{ms}$

Case 2, 4, 6 $T_1 = T_2 = 100\text{ms}$ with 50ms random jitter

Case 3, 5, 7 $T_1 = T_2 = 100\text{ms}$ with 100ms random jitter

In case 2 and 3, random jitter is given by the standard distribution. In case 4 and 5, random jitter is given by the exponential distribution. In case 6 and 7, random jitter is given by the uniform distribution. Figure 7-11 shows the model and the time history of time delay for case 2 to case 7. In case 2 and case 3, minimum time delay and maximum time delay are set from the 3 sigma value of the standard deviation. In case 4 and case 5, those time delay are set for realizing time delay from 50 to 150ms or 0 to

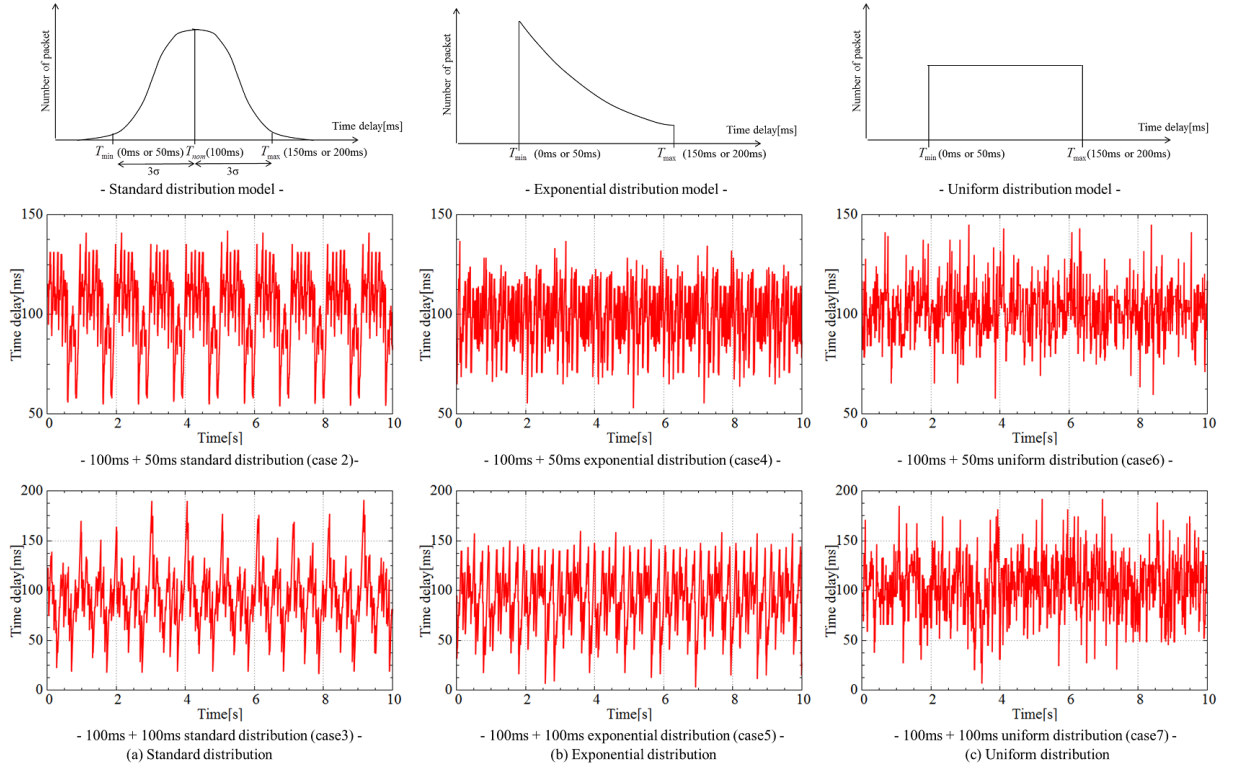


Fig. 7-11: The model and time history of time delay for case 2 to case 7.

200ms. In the time history of time delay, differential values between adjacent delays does not exceed the sampling time from the function of the network emulator. This function is implemented to prevent from interchanging of the sending data.

\hat{T}_1 in Fig. 7-6 is estimated by subtracting the time stamp of the slave robot from the time stamp of the master robot. \hat{T}_2 in Fig. 7-6 is estimated by subtracting the time stamp of the master robot from the time stamp of the slave robot. As this paper supposed that the problem of the clock difference is solved by using reference papers [107] or [108], clock times of the master robot and the slave robot are set to be the same value.

Here, $1 - e^{-\hat{T}_1 s}$ or $1 - e^{-\hat{T}_2 s}$ are implemented by memorizing the past force response of the master robot or the slave robot. From Table I, the sampling time of the experiment is set as 0.001s. 0.001s is enough to attain the control performance. So, considering the sampling period (0.001s) and time delay for the experiment (from 0.0s to 0.2s) as shown in Fig. 7-11, 200 memories are needed at most. This is not difficult to implement by using the master side computer and the slave side computer.

Experimental Results

Figure 7-12 shows the experimental results. The force response of the master robot is plotted in the reverse value to compare with the force response of the slave robot. Hatching areas are showing that the slave robot contacts environment.

Figure 7-12(a), (c), (e), (g), (i), (k) and (m) show the experimental results for the conventional method. Figure 7-12(b), (d), (f), (h), (j), (l) and (n) show the experimental results for the proposed method.

From Fig. 7-12(a), (c), (e), (g), (i), (k) and (m), it is shown that oscillations are occurred during the contact motion in the conventional method. Figure 7-12(b) shows that the oscillation during the contact motion is suppressed by using the proposed method. Moreover, Fig. 7-12(d), (f), (h), (j), (l) and (n) show that various kinds of time varying delay do not raise oscillations during the contact motion. Thus, it is shown that the proposed method is valid to improve the stability of the force control of the bilateral control system.

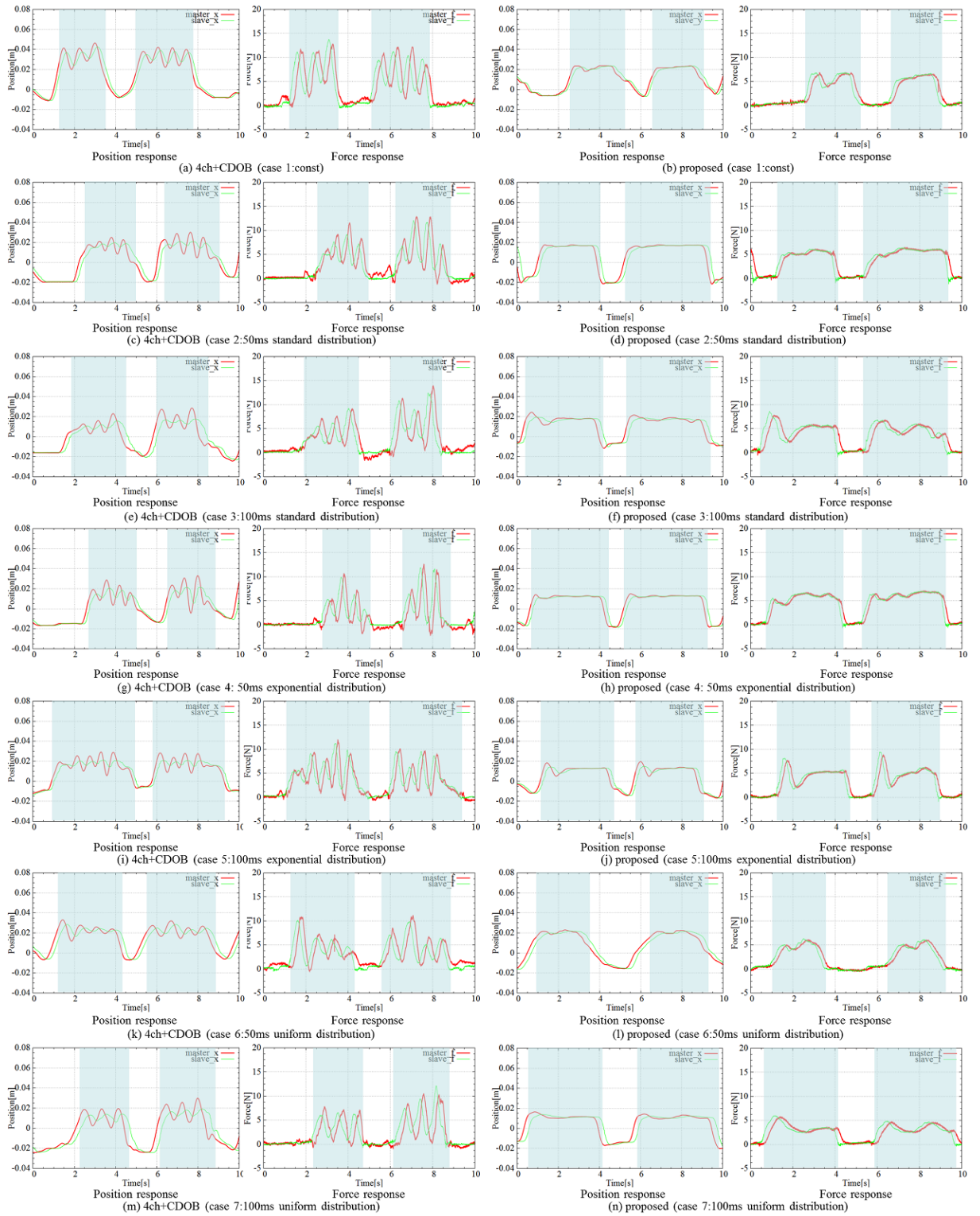


Fig. 7-12: Experimental results.

7.4 Time Delay Compensation with Model-Free Time Delay Compnesator

In this section, model-free time delay compensator is proposed. Firstly, two flow expression method of the four-channel bilateral control system is shown. The master system and the slave system of the four-channel bilateral control system are modeled as single input and single output (SISO) system by using this method. This method is useful to the stability analysis of the bilateral control system. Then, model-free time delay compensator is proposed. The proposed compensator does not utilize the time delay model and the plant model, but the position control and the force control are stabilized.

7.4.1 Two Flow Expression of Four-Channel Bilateral Control System

In the four-channel bilateral control system, the master system and the slave system are sending position and force information and receiving those of them. Thus, the master system and the slave system are multi input and multi output (MIMO) system. MIMO system is not easy to analyze the stability and the performance. Therefore, in this section, two flow expression method of the four-channel bilateral control system is proposed. By utilizing two flow expression method, the master system and the slave system are modeled as SISO system.

Firstly, the acceleration response of the four-channel bilateral control system is analyzed. If the cut-off frequency of LPF in DOB approaches infinity, the acceleration responses of the master robot and the slave robot in Fig. 7-2 are expressed as follows.

$$s^2 x_m^{res} = C_p(s)(e^{-T_2 s} x_s^{res} - x_m^{res}) - C_f(e^{-T_2 s} \hat{f}_s^{ext} + \hat{f}_m^{ext}), \quad (7.27)$$

$$s^2 x_s^{res} = C_p(s)(e^{-T_1 s} x_m^{res} - x_s^{res}) - C_f(e^{-T_1 s} \hat{f}_m^{ext} + \hat{f}_s^{ext}). \quad (7.28)$$

Here, DOB works ideally and the disturbance force including the parameter fluctuation is suppressed completely, i. e. $x_m^{res} = \ddot{x}_m^{ref}/s^2$ and $x_s^{res} = \ddot{x}_s^{ref}/s^2$. Thus, equation (7.27)-(7.28) do not include dynamics such as the mass variable. Equation (7.27)-(7.28) are not realized in the high-frequency area above the cut-off frequency of LPF in DOB (g_d). In usual cases, g_d can be set large enough, so this assumption is negligible in practical cases.

Then, the position control and the force control of the bilateral control system are decomposed as follows.

$$s^2 x_m^{res,p} = C_p(s)(e^{-T_2 s} x_s^{res} - x_m^{res}), \quad (7.29)$$

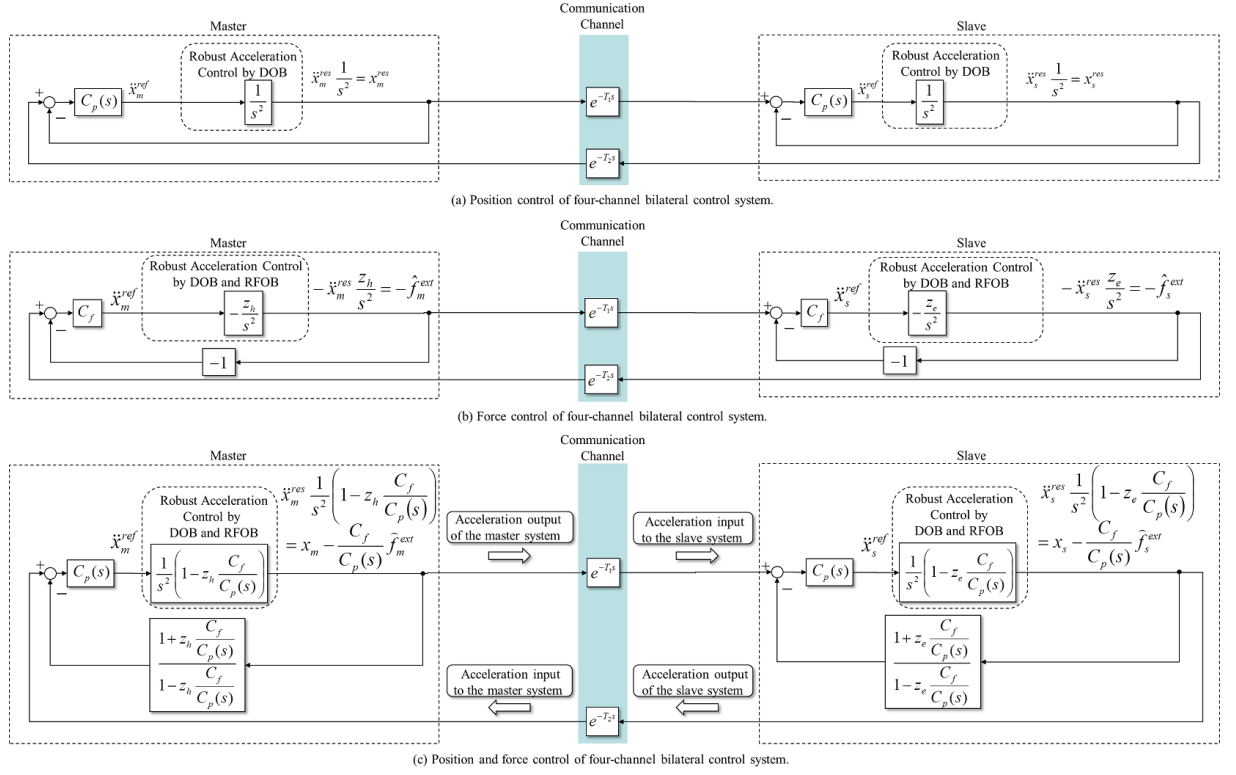


Fig. 7-13: Two flow expression of acceleration based four-channel bilateral control system.

$$s^2 x_s^{res,p} = C_p(s)(e^{-T_1 s} x_m^{res} - x_s^{res}), \quad (7.30)$$

$$s^2 x_m^{res,f} = -C_f(e^{-T_2 s} \hat{f}_s^{ext} + \hat{f}_m^{ext}), \quad (7.31)$$

$$s^2 x_s^{res,f} = -C_f(e^{-T_1 s} \hat{f}_m^{ext} - \hat{f}_s^{ext}). \quad (7.32)$$

Here, $s^2 x_m^{res,p}$ or $s^2 x_s^{res,p}$ are the acceleration response of the position control, $s^2 x_m^{res,f}$ or $s^2 x_s^{res,f}$ are the acceleration response of the force control.

From equation (7.29) and (7.30), the block diagram for the position control of the bilateral control system is expressed as Fig. 7-13(a). From equation (7.31) and (7.32), the block diagram for the force control of the bilateral control system is expressed as Fig. 7-13(b). In Fig. 7-13 (b), RFOB works ideally and the wideband force sensation is realized, i. e. $\hat{f}_m^{res} = x_m^{res} z_h$ and $\hat{f}_s^{res} = x_s^{res} z_e$. z_h means the human impedance and z_e means the environmental impedance. Figure 7-13(b) is not realized in the

high-frequency area above the cut-off frequency of LPF in RFOB (g_r). In usual cases, g_r can be set large enough, so this assumption is negligible in practical cases.

Finally, by summing Fig. 7-13(a) and (b), Fig. 7-13(c) is derived. As shown in Fig. 7-13(c), the master system and the slave system are modeled as SISO system. The input and the output of each system is acceleration information as shown in Fig. 7-13(c). Accelerations \ddot{x}_m^{res} or \ddot{x}_s^{res} work as an agent to connect both control systems. From the block diagrams of the master system and the slave system in Fig. 7-13(c), transfer functions of each system are derived in subsection 7.4.2.

7.4.2 Validation of Model-Free Time Delay Compensator

In this subsection, model-free time delay compensator is proposed. Moreover, the stability and the performance of the proposed control system are shown by using two flow expression method.

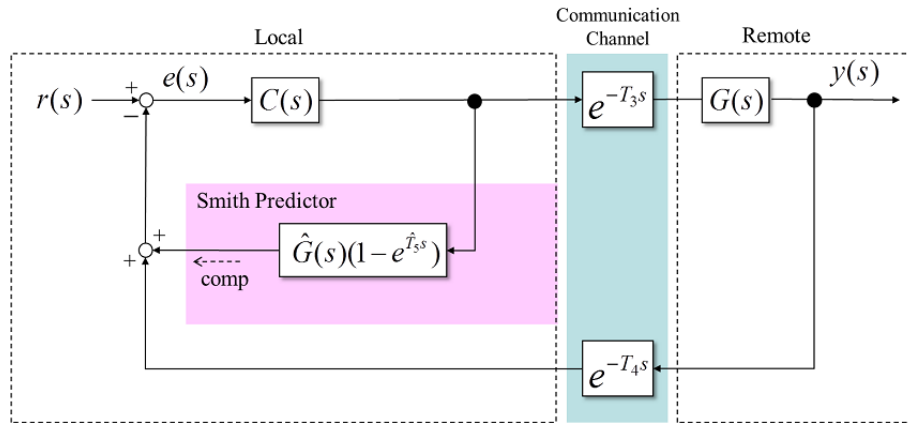
Model-Free Time Delay Compensator

Model-free time delay compensator is inspired from the idea of CDOB. Figure 7-14 shows a feedback control system with CDOB and Smith predictor. Figure 7-14(a) shows a feedback control system with Smith predictor and Fig. 7-14(b) shows a feedback control system with CDOB. In the figure, $G(s)$ is the controlled plant, $r(s)$ and $y(s)$ are the input and the output, respectively. T_3 denotes time delay from the local system to the remote system. T_4 denotes time delay from the remote system to the local system. $\hat{G}(s)$ is the plant model and \hat{T}_5 is the round trip time delay ($T_5 = T_3 + T_4$) model. From Fig. 7-14(a), Smith predictor stabilizes the feedback control system by utilizing the time delay model (\hat{T}_5) and the plant model ($\hat{G}(s)$). On the other hand, time delay compensation by CDOB which is shown in Fig. 7-14(b) only utilizes the plant model ($\hat{G}(s)$). Here, Fig. 7-14(c) shows the equivalent transformation of Fig. 7-14(b). It is shown that CDOB works the same performance with Smith predictor without the round trip time delay model. This is because that the CDOB calculates the compensation value 'comp' by the differentiation of 'comp1' and 'comp2'. This is the biggest advantage in CDOB approach.

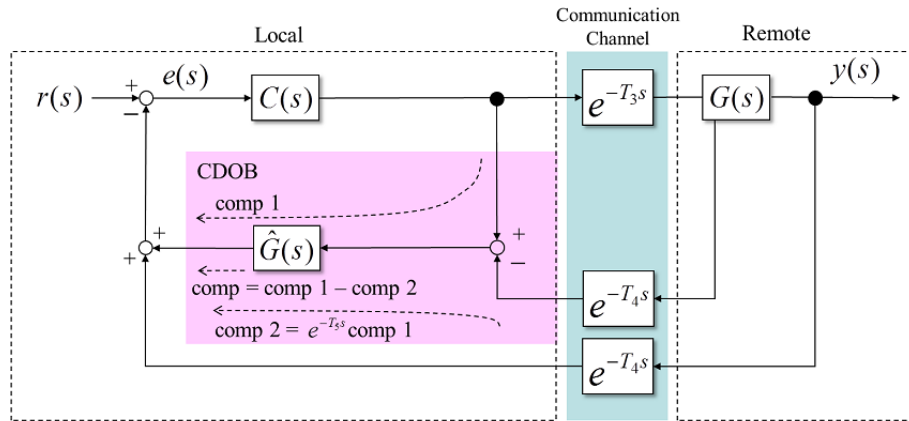
The proposed model-free time delay compensator utilizes the differentiation of the signal before and after going through the communication channel as the compensation values like CDOB approach. Examples of the differentiation signals in the four-channel bilateral control system are $x_m^{res} - x_m^{res}e^{-Ts}$ or $\hat{f}_m^{ext} - \hat{f}_m^{ext}e^{-Ts}$. Here, T is the round trip time delay ($T = T_1 + T_2$) in Fig. 7-2. These signals become 0 if the phase lag is around 0 degrees and $2x_m^{res}$ or $2\hat{f}_m^{ext}$ if the phase lag becomes around 180 degrees. Thus, these signals are valid to prioritize information in the master side control system. Then, the acceleration references of the bilateral control system with model-free time delay compensator are designed as follows.

$$s^2 x_m^{ref} = C_p(s)(e^{-T_2 s} x_s^{res} - x_m^{res}) - C_f(e^{-T_2 s} \hat{f}_s^{ext} + \hat{f}_m^{ext}) + C_p(s)(e^{-(T_1+T_2)s} x_m^{res} - x_m^{res}) + C_f(e^{-(T_1+T_2)s} \hat{f}_m^{res} - \hat{f}_m^{res}), \quad (7.33)$$

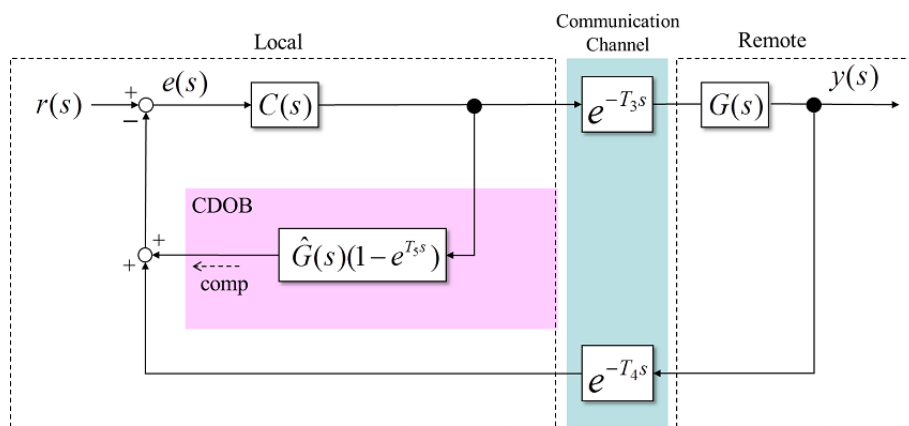
$$s^2 x_s^{ref} = C_p(s)(e^{-T_1 s} x_m^{res} - x_s^{res}) - C_f(e^{-T_1 s} \hat{f}_m^{ext} + \hat{f}_s^{ext}). \quad (7.34)$$



(a) Time delay compensation by Smith predictor.



(b) Time delay compensation by CDOB.



(c) Equivalent transformation of (b).

Fig. 7-14: Time delay compensation in feedback control system.

In equation (7.33), the third term and the fourth term are corresponding to the compensation values. In the case that the phase lag is around 0 degrees, these signals become 0. Then, the acceleration reference of the master system becomes as equation (7.35).

$$s^2 x_m^{ref} = C_p(s)(e^{-T_2 s} x_s^{res} - x_m^{res}) - C_f(e^{-T_2 s} \hat{f}_s^{ext} + \hat{f}_m^{ext}). \quad (7.35)$$

This is same as the acceleration reference of the four-channel bilateral control system for the master system. In the case that the phase lag is around 180 degrees, compensation values become $-2x_m^{res}$ or $-2\hat{f}_m^{ext}$. Then, by the compensation values, scaling is added in the master control system as equation (7.36).

$$s^2 x_m^{ref} = C_p(s)(e^{-T_2 s} x_s^{res} - 3x_m^{res}) - C_f(e^{-T_2 s} \hat{f}_s^{ext} + 3\hat{f}_m^{ext}). \quad (7.36)$$

This means that the master system utilizes more information of own system compared with the slave system. This is valid to reduce the time delay effect since the general bilateral control systems with time delay can become unstable when the phase lag becomes around 180 degrees.

By utilizing equation (7.33) and (7.34), the bilateral control system with model-free time delay compensator is implemented as Fig. 7-15. Compensation values for the position control and the force control of the bilateral control system are calculated in the hatched area of Fig. 7-15. Here, compensation values are calculated by the differentiation of the signal before and after going through the communication channel. Thus, the time delay model and the plant model are not utilized to calculate compensation values. So, it is called model-free time delay compensator.

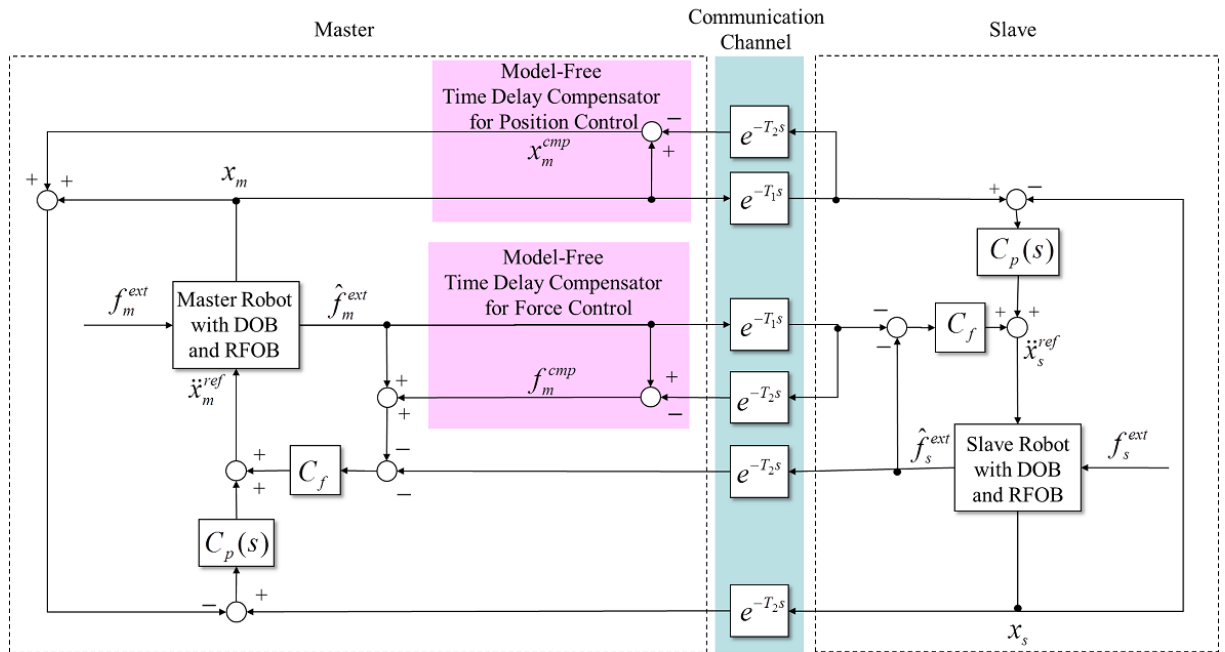


Fig. 7-15: Bilateral control system with model-free time delay compensator.

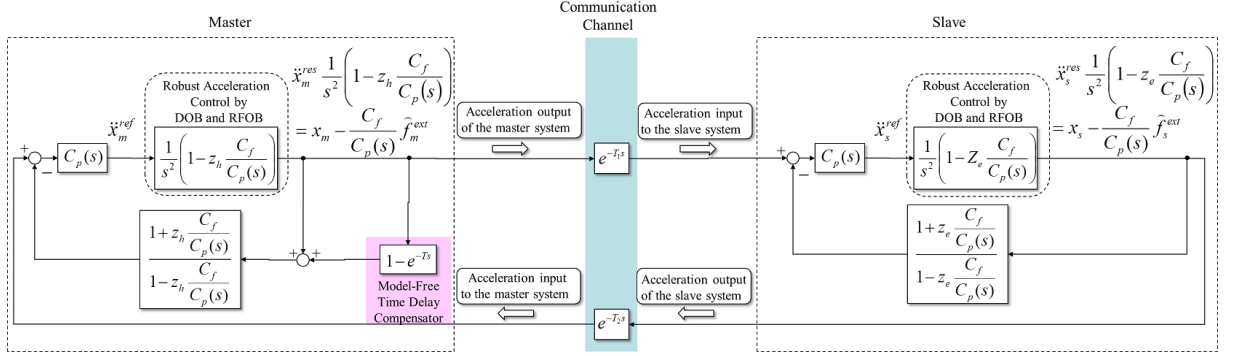


Fig. 7-16: Two flow expression of bilateral control system with model-free time delay compensator.

$$L_{w/o}(s) = - \underbrace{\frac{C_p(s) - Z_h C_f}{s^2 + C_p(s) + Z_h C_f}}_{\text{master system}} \cdot \underbrace{\frac{C_p(s) - Z_e C_f}{s^2 + C_p(s) + Z_e C_f}}_{\text{slave system}} \cdot \underbrace{e^{-(T_1+T_2)s}}_{\text{communication channel}} \quad (7.37)$$

Stability

In this subsection, the stability of the bilateral control system with model-free time delay compensator is discussed by using two flow expression method. Figure 7-16 shows the block diagram of the bilateral control system with model-free time delay compensator in two flow expression. Compared with Fig. 7-13(c), model-free time delay compensator is added in Fig. 7-16.

From Fig. 7-13(c) and Fig. 7-16, the open-loop transfer function for the bilateral control system without model-free time delay compensator ($L_{w/o}$) and those for the bilateral control system with model-free time delay compensator ($L_{w/c}$) are calculated as equation (7.37) and (7.38). Then, these open-loop transfer functions are decomposed as (7.39) to (7.43) for analyzing the stability.

$$L_{w/o}(s) = A(s) \cdot B(s), \quad (7.39)$$

$$L_{w/c}(s) = A(s) \cdot C(s), \quad (7.40)$$

$$A(s) = - \frac{C_p(s) - Z_h C_f}{s^2 + C_p(s) + Z_h C_f} \cdot \frac{C_p(s) - Z_e C_f}{s^2 + C_p(s) + Z_e C_f}, \quad (7.41)$$

$$B(s) = e^{-(T_1+T_2)s}, \quad (7.42)$$

$$\begin{aligned}
 L_{w/c}(s) &= \underbrace{-\frac{C_p(s) - Z_h C_f}{s^2 + C_p(s) + Z_h C_f}}_{\text{master system with compensator}} \cdot \frac{1}{1 + \frac{C_p(s) - Z_h C_f}{s^2 + C_p(s) + Z_h C_f} (1 - e^{-T_2 s})} \cdot \underbrace{\frac{C_p(s) - Z_e C_f}{s^2 + C_p(s) + Z_e C_f}}_{\text{slave system}} \\
 &\quad \cdot \underbrace{e^{-(T_1+T_2)s}}_{\text{communication channel}} \\
 &= \underbrace{-\frac{C_p(s) - Z_h C_f}{s^2 + C_p(s) + Z_h C_f}}_{\text{master system}} \cdot \underbrace{\frac{C_p(s) - Z_e C_f}{s^2 + C_p(s) + Z_e C_f}}_{\text{slave system}} \cdot \underbrace{\frac{e^{-(T_1+T_2)s}}{1 + \frac{C_p(s) - Z_h C_f}{s^2 + C_p(s) + Z_h C_f} (1 - e^{-T_2 s})}}_{\text{communication channel with compensator}}.
 \end{aligned} \tag{7.38}$$

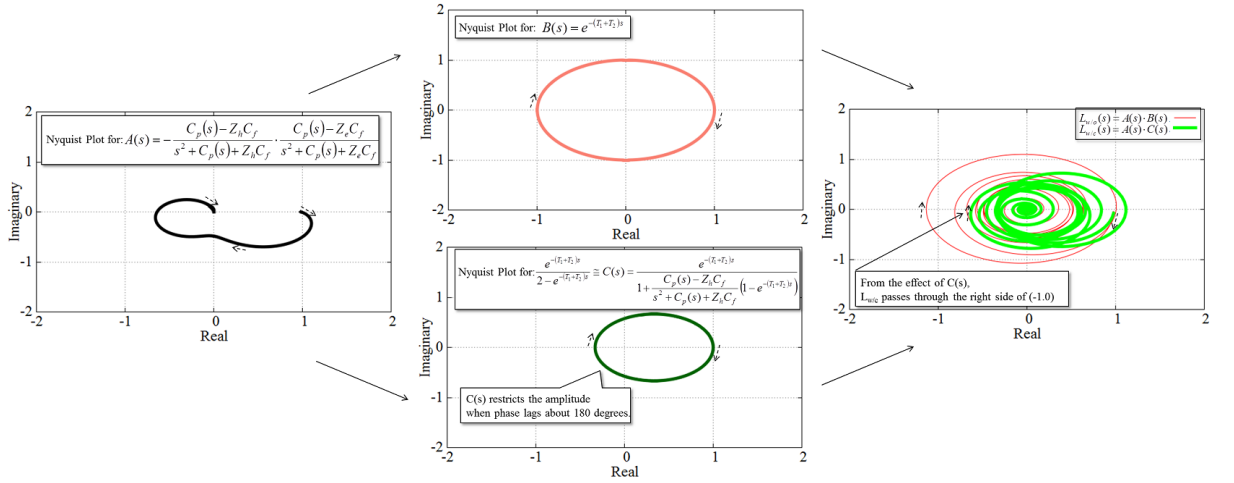


Fig. 7-17: Nyquist diagram for bilateral control system without and with model-free time delay compensator.

$$C(s) = \frac{e^{-(T_1+T_2)s}}{1 + \frac{C_p(s) + Z_h C_f}{s^2 + C_p(s) - Z_h C_f} (1 - e^{-(T_1+T_2)s})}. \tag{7.43}$$

Here, $A(s)$ is corresponding to the transfer function of the master system and the slave system with no time delay compensator. $B(s)$ is showing time delay from the communication channel. $C(s)$ is corresponding to time delay from the communication channel with model-free time delay compensator.

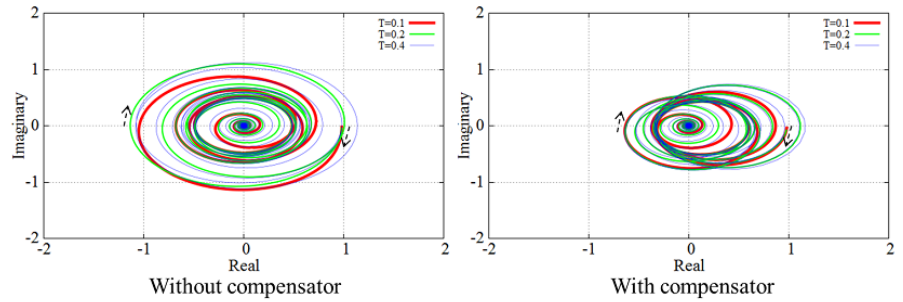
Figure 7-17 shows the Nyquist diagrams of those equations. Table 7.2 shows the parameter for the Nyquist diagrams. Here, the human impedance (z_h) is settled as $0 + 0s$ to see the stability in conservative ways. This is because that the control system can be stabilized from the damping effect of the human

Table 7.2: Parameters for analysis and experiment

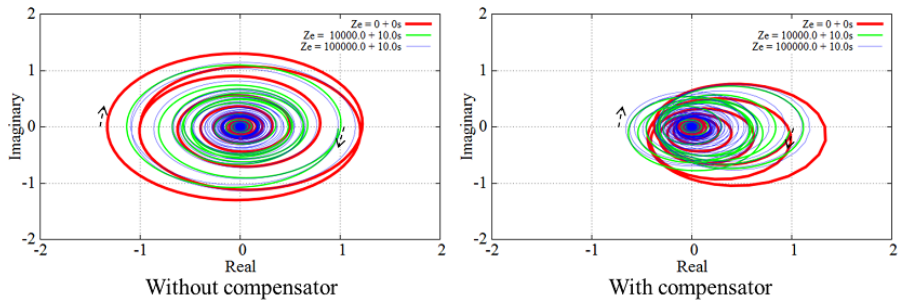
Position feedback gain	K_P	100
Velocity feedback gain	K_V	20
Force feedback gain	K_f	1.0
Human impedance(for analysis)	z_h	0+0s
Environmental impedance(for analysis)	z_e	10000+10s
Nominal mass	M_n	0.5kg
Thrust coefficient	K_{tn}	32.5N/A
One way time delay	T	0.2s

impedance. From Fig. 7-17, it is shown that the time delay effect $B(s)$ shifts the phase of $A(s)$ that the Nyquist diagram of $L_{w/o}(s)$ passes through the left side of (-1,0). On the other hand, the time delay effect with model-free time delay compensator $C(s)$ restricts the amplitude of the $A(s)$ when the phase lags about 180 degrees. Thus, the Nyquist diagram of $L_{w/c}(s)$ passes through the right side of (-1,0). Therefore, the bilateral control system is stabilized when the model-free time delay compensator is added. As shown in equation (7.38), there does not include dynamics such as the mass variable in the open loop transfer function of $L_{w/c}(s)$. So, model-free time delay compensator works even if the size of the master system and the slave system are different.

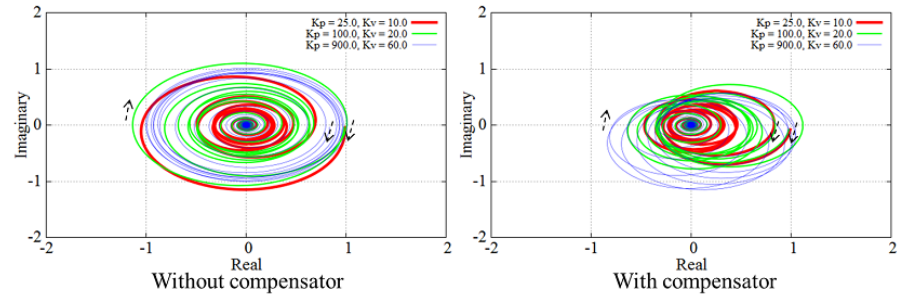
For analyzing the stability in more general cases, a parametric study for the Nyquist diagrams has been conducted. Figure 7-18 shows the parametric study results. In Fig. 7-18, time delay, an environmental impedance, a position feedback gain and a force feedback gain are parameterized. From Fig. 7-18, it is shown that the bilateral control system with model-free time delay compensator is always stable. Figure 7-18(a) shows that the bilateral control system without the compensator is not stable in all cases of time delay. From Fig. 7-18(b), the stability of the bilateral control system without the compensator becomes worse when the environmental impedance becomes small. Figure 7-18(c) shows that the stability of the bilateral control system without the compensator is improved by increasing the position feedback gain. Figure 7-18(d) shows that the bilateral control system without the compensator is not stable in all cases of the force feedback gain. Thus, model-free time delay compensator is valid to stabilize the bilateral control system with time delay.



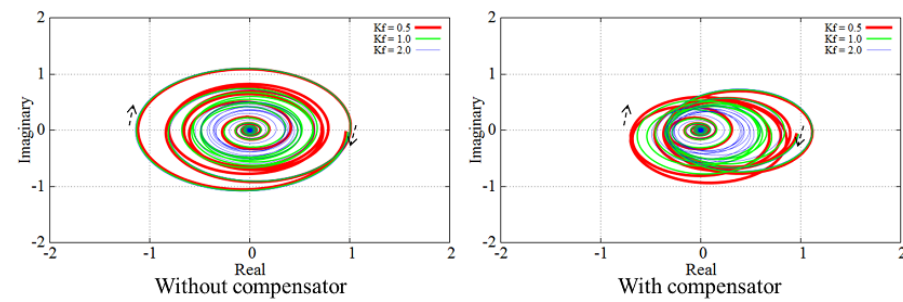
(a) Effect of delay time.



(b) Effect of environmental impedance.



(c) Effect of $C_p(s)$.



(d) Effect of C_f .

Fig. 7-18: Parametric study results of Nyquist diagram.

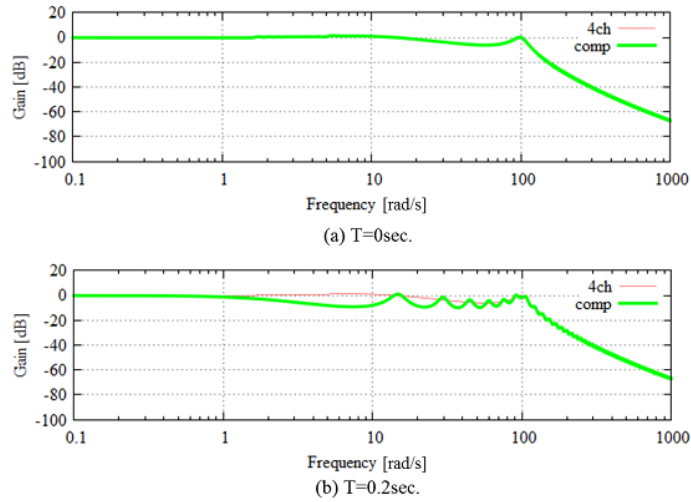


Fig. 7-19: Gain characteristics of open loop transfer function.

Performance

In this subsection, the performance of the bilateral control system with model-free time delay compensator is analyzed by using two flow expression method.

Figure 7-19 shows the gain characteristics of the open loop transfer function. The open loop transfer functions are derived from equation (7.37) and (7.38). Figure 7-19(a) shows those with no time delay ($T = 0$) and Fig. 7-19(b) shows those with time delay ($T = 0.2s$). As shown in Fig. 7-19 (a), gain characteristics are same in the bilateral control system without and with model-free time delay compensator when there is no time delay. Figure 7-19 (b) shows that gain characteristics are restricted in the bilateral control system with model-free time delay compensator when there is 0.2s time delay. Therefore, as shown in subsection 7.4.2, model-free time delay compensator works to restrict the performance to stabilize the control system. This restriction works automatically depending on time delay and does not need the time delay model and the system model.

7.4.3 Experiment

In this subsection, experimental results are shown to confirm the validity of the proposed method.

Experimental System

Figure 7-20 shows the experimental system. The master and the slave system are consisted of 1-DOF

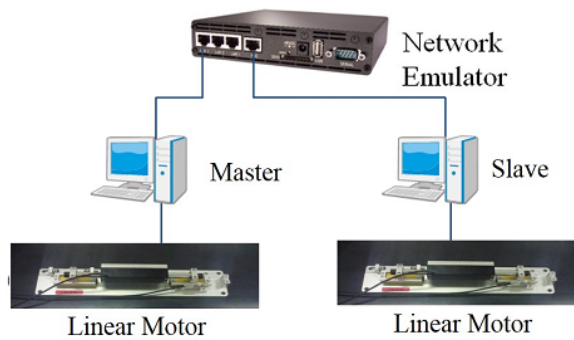


Fig. 7-20: Experimental system.

robots. The robot consists of the linear motor and the encoder. A human operator manipulates the master side linear motor, and the slave side linear motor contacts environment. The resolution of the encoder is $0.1 \mu\text{m}$. Time delay is created by the network emulator. In the experiment, one way time delay is set as 0.2s. Control parameters used in the experiments are shown in Table 7.2.

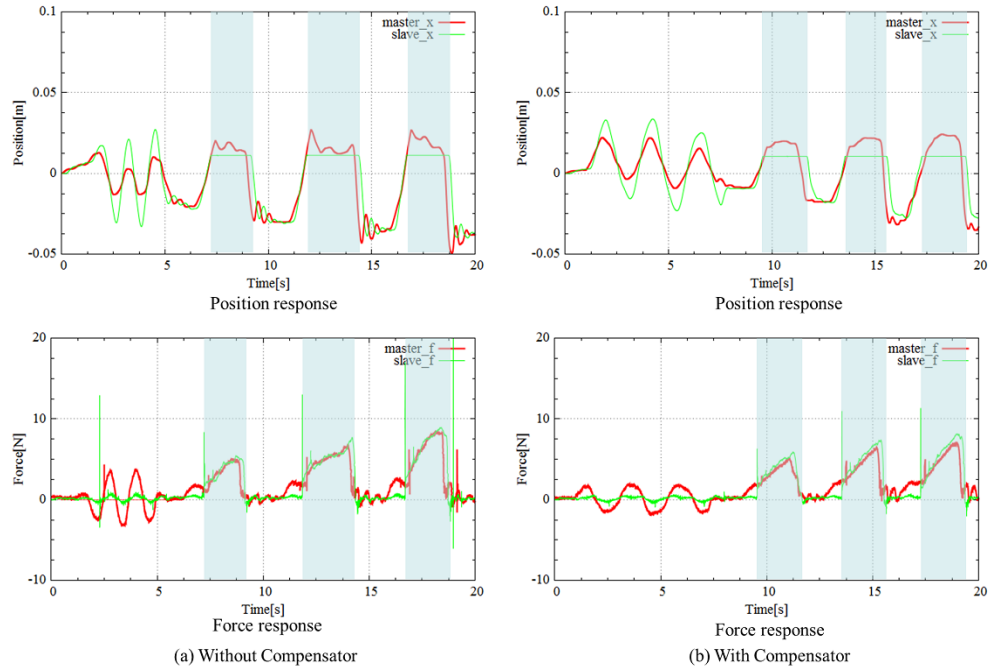


Fig. 7-21: Experimental results.

Experimental Results

Figure 7-21 shows the experimental results. The force response of the master robot is plotted in the reverse value to compare with the force response of the slave robot. Hatched areas are showing that the slave robot contacts environment. Figure 7-21(a) shows the experimental results of without model-free time delay compensator, Fig. 7-21(b) shows those with model-free time delay compensator.

In the case of without model-free time delay compensator, the position response is vibrating during contact with environment. On the other hand, in the case of with model-free time delay compensator, there is no vibration during contact with environment. Therefore, it is shown that model-free time delay compensator is valid to stabilize the bilateral control system with time delay.

7.5 Synchronization of Haptic and Visual Sense

In this section, the bilateral control system to Synchronize Haptic and Visual Sense has been proposed.

7.5.1 Utilization of Round Trip Time Delayed Force Information

The position of the master robot and the visual image of the slave robot should be same to synchronize haptic and visual sense. For realizing this control target, the round trip time delayed master force is effective. By using the round trip time delayed master force, the master robot moves after the slave robot moves.

Then, the acceleration references of the master robot and the slave robot are set as shown in equation (7.44) and (7.45) in the proposed control system.

$$s^2 x_m^{ref} = C_p(s)(e^{-T_2 s} x_s^{res} - x_m^{res}) - C_f(e^{-T_2 s} \hat{f}_s^{ext} + e^{-(T_1+T_2)s} \hat{f}_m^{ext}) + C_p(s)(e^{-(T_1+T_2)s} x_m^{res} - x_m^{res}), \quad (7.44)$$

$$s^2 x_s^{ref} = C_p(s)(e^{-T_1 s} x_m^{res} - x_s^{res}) - C_f(e^{-T_1 s} \hat{f}_m^{ext} - \hat{f}_s^{ext}). \quad (7.45)$$

In the acceleration reference of the master robot, the first term is the position controller, the second term is the force controller and the third term is model-free time delay compensator for the position control. The round trip time delayed master force is utilized in the force controller of the master robot. So, the master robot moves depending on the round trip time delayed force input from the human operator. Then, the position response of the master robot (x_m^{res}) are synchronized with the position response of the slave robot which is passed from the communication channel ($e^{-T_2 s} x_s^{res}$). If the visual image of the slave robot is supposed to be transmitted to the master robot at the same time with the position and the force response of the slave robot, i. e. $T_1 = T_3$ in Fig. 7-1, the position response of the master robot synchronizes with the visual image of the slave robot. By utilizing equation (7.44) and (7.45), the proposed control system is implemented as Fig. 7-22. The model-free time delay compensator for the force control is omitted in equation (7.44) to prioritize the synchronization of the position of the master robot and the visual image of the slave robot. The stability effect will be discussed in the next subsection.

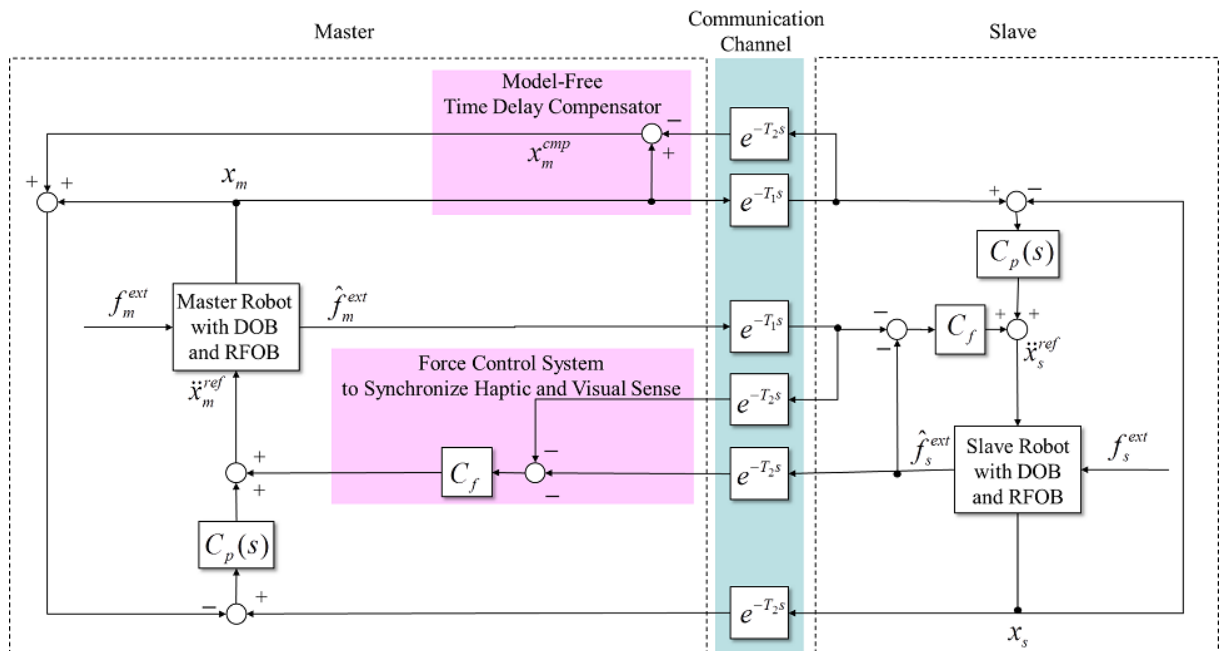


Fig. 7-22: Bilateral control system to synchronize haptic and visual sense.

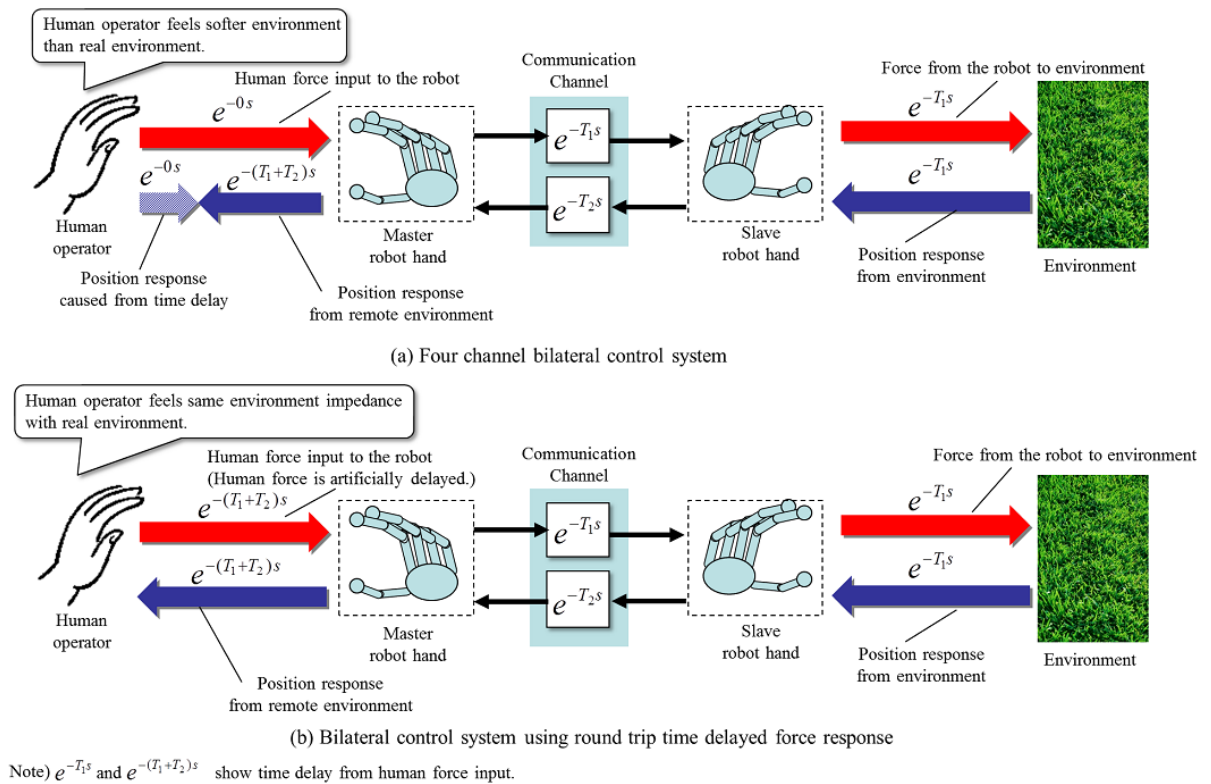


Fig. 7-23: The advantage of using round trip time delayed force information.

There is the additional advantage for utilizing the round trip time delayed master force. Figure 7-23 shows the advantage for utilizing the round trip time delayed force. In the four-channel bilateral control system, the human force input is transmitted to the master robot hand in real time. Then, the force input is transmitted to the slave robot hand with the communication delay T_1 . After that, the environmental position response is back to the master robot hand with the communication delay T_2 . In that time, the human operator feels the environmental impedance. However, immediately after inputting the human force, the position response is caused from time delay. Thus, the human operator feels the softer environment than the real environment. On the other hand, if the human force input to the master robot hand is artificially delayed while transmitting force information to the slave robot hand, there is no position response caused from time delay. So, the human operator feels the same environmental impedance with the real environment. This is the additional advantage for utilizing the round trip time delayed master force.

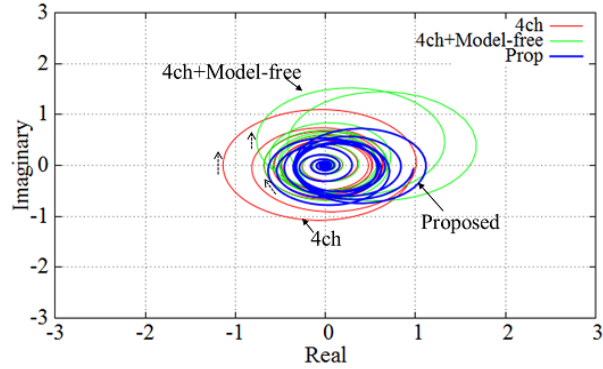


Fig. 7-24: Nyquist plot.

Table 7.3: Parameters for analysis and experiment

Position feedback gain	K_P	100	
Velocity feedback gain	K_V	20	
Force feedback gain	K_f	1.0	
Cut-off frequency of DOB	g_{dis}	500	rad/s
Cut-off frequency of RFOB	g_{reac}	500	rad/s
Cut-off frequency of CDOB	g_{cdob}	500	rad/s
Human impedance	Z_h	0+0s	
Enviromental impedance	Z_e	10000+10s	
Nominal mass	M_n	0.5	kg
Thrust coefficient	K_{tn}	32.5	N/A
One way time delay(for analysis)	T	0.2	s

7.5.2 Discussion of Stability and Performance

In this subsection, the stability and the performance of the proposed control system are analyzed.

Stability Analysis

Figure 7-24 shows Nyquist diagram which are calculated by utilizing two flow expression method. Table 7.3 shows parameters for this analysis. In Fig. 7-24, Nyquist diagram of the four-channel bilateral control system, the four-channel bilateral control system with model-free time delay compensator and the proposed control system are described. It is shown that the proposed control system is stable as the four-channel bilateral control system with model-free time delay compensator.

Performance Analysis

For evaluating the performance of the bilateral control system, Hybrid parameters, "reproducibility" and "operationality" are utilized [65], [44]. The relation between the master robot and the slave robot are formulated by independent variables H as shown in equation (7.46).

$$\begin{bmatrix} f_m^{ext} \\ -x_s \end{bmatrix} = \begin{bmatrix} H_{11} & H_{12} \\ H_{21} & H_{22} \end{bmatrix} \begin{bmatrix} x_m \\ -f_s^{ext} \end{bmatrix}. \quad (7.46)$$

Then, the slave force is treated as follows with the environmental impedance z_e .

$$f_s^{ext} = z_e x_s. \quad (7.47)$$

From (7.46) and (7.47), the force in the master robot is represented as shown in equation (7.48).

$$f_m^{ext} = \left(\frac{H_{12}H_{21}}{1 - H_{22}z_e} z_e + H_{11} \right) x_m. \quad (7.48)$$

Here P_r and P_o are defined as follows.

$$P_r = \frac{H_{12}H_{21}}{1 - H_{22}z_e}, \quad (7.49)$$

$$P_o = H_{11} \quad (7.50)$$

Hence, (7.48) is represented as follows.

$$f_m^{ext} = (P_r x_e + P_o) x_m. \quad (7.51)$$

P_r and P_o are defined as "reproducibility" and "operationality". Because the reproduction of the environmental impedance in the master side is the important condition in the bilateral teleoperation, $|P_r| = 1$ should be satisfied. Additionally, when the operational force is small, ideally $P_o = 0$ is realized, the operator can feel the real environmental impedance naturally. The ideal condition that satisfies perfect reproducibility and operationality is called the condition with high transparency. Hybrid parameters of the proposed control system are derived as follows.

$$H_{11} = -\frac{C_p(s)(e^{-Ts} - 1) - s^2}{C_f} e^{-Ts}, \quad (7.52)$$

$$H_{12} = e^{T_1 s}, \quad (7.53)$$

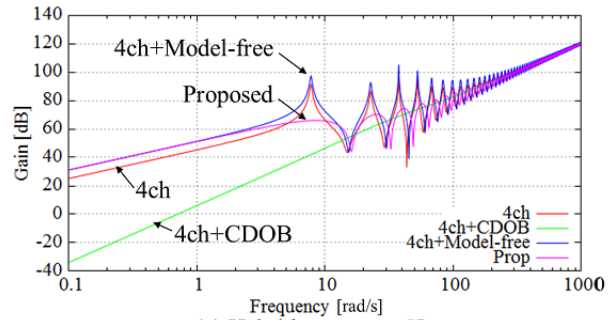
$$H_{21} = -e^{-T_2 s}, \quad (7.54)$$

$$H_{22} = 0. \quad (7.55)$$

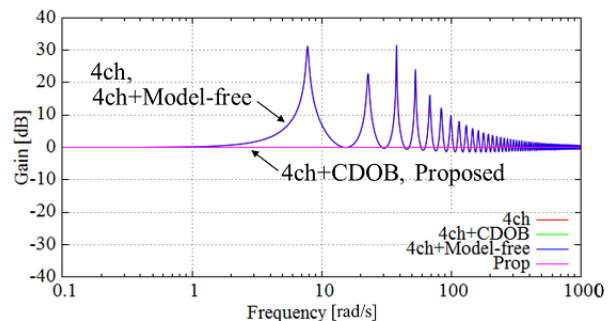
From H_{21} parameters, it is shown that $x_m = x_s e^{-T_2 s}$ is realized. Then, in the teleoperation system with haptic and visual sense feedback which is shown in Fig. 7-1, the position of the master robot and the visual image of the slave robot are same, if $T_2 = T_3$ is realized. This is important in haptic and visual sense synchronization.

Figure 7-25 and Fig. 7-26 show gain characteristics of hybrid parameters, reproducibility and operability. Gain characteristics of the four-channel bilateral control system, the four-channel bilateral control system with CDOB, the four-channel bilateral control system with model-free time delay compensator are described as references.

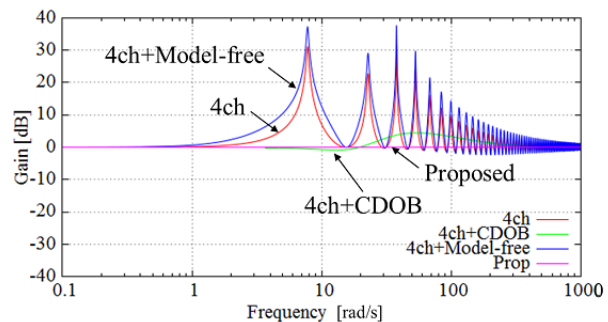
From Fig. 7-25(a), the proposed control system has large values compared with four-channel bilateral control system with CDOB. Thus, as shown in Fig. 7-26(b), operability is not so good. For improving operability, the position feedback gain should be decreasing or the force feedback gain should be increasing. As shown in Fig. 7-25(b), (c) and (d), gain characteristics of the proposed control system are well improved. Thus, as shown in Fig. 7-26(a), reproducibility of the proposed control system is the best compared with other conventional methods. The point is that the gain of reproducibility is 0 in the all frequency area. Therefore, the gain of the environmental impedance is perfectly reproduced in the proposed control system.



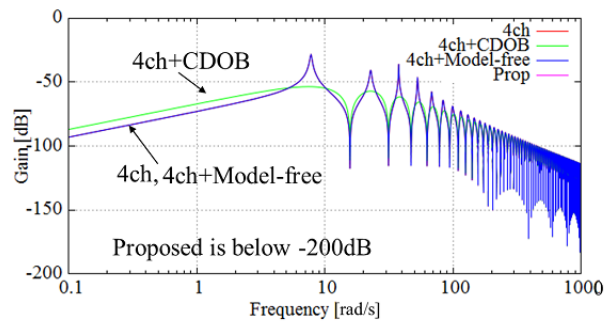
(a) Hybrid parameter H_{11}



(b) Hybrid parameter H_{12}



(c) Hybrid parameter H_{21}



(d) Hybrid parameter H_{22}

Fig. 7-25: Gain characteristics of hybrid parameters.

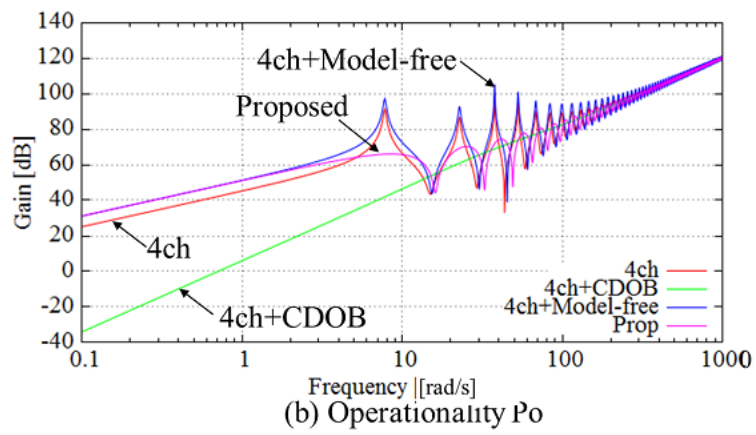
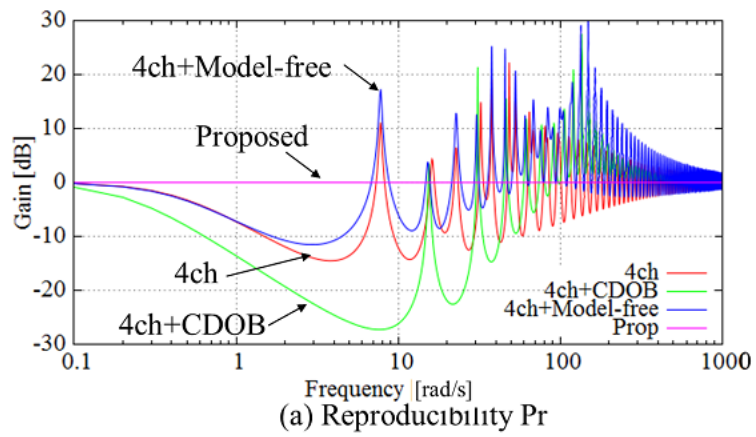


Fig. 7-26: Gain characteristics of reproducibility and operationality.

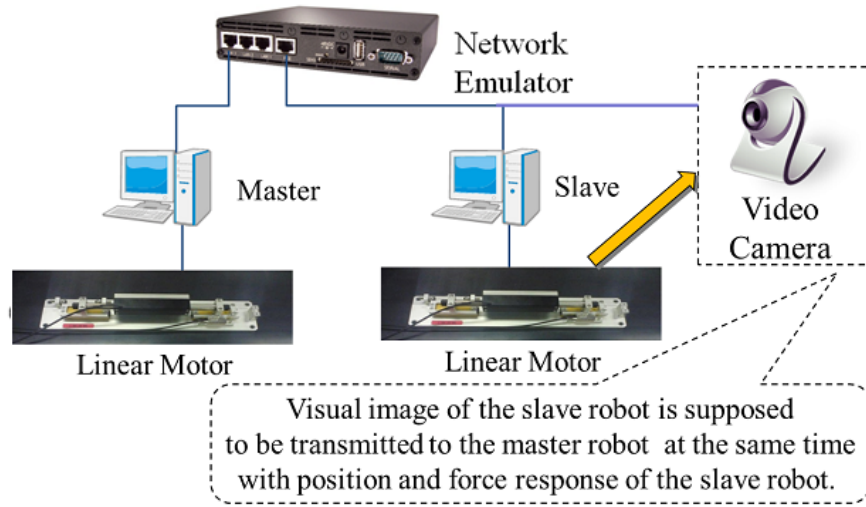


Fig. 7-27: Experimental system.

7.5.3 Experiment

In this subsection, experimental results are shown to confirm the validity of the proposed system.

Experimental System

Figure 7-27 shows the experimental system. The master and the slave system consist of 1-DOF robots. The robot consists of the linear motor and the encoder. A human operator manipulates the master side linear motor, and the slave side linear motor contacts environment. The resolution of the encoders is $0.1 \mu\text{m}$. Time delay is created by the network emulator. In the experiment, one way delay is set as 200ms with 30ms random jitter. The random jitter is given by uniform distribution. Control parameters used in the experiments are shown in Table 7.3. In the experiment, the visual image of the slave robot is supposed to be transmitted to the master side at the same time with the position and the force response of the slave robot, i. e. $T_1 = T_3$.

Experimental Results

Figure 7-28 shows the experimental results. The force response of the master robot is plotted in the reverse value to compare with the force response of the slave robot. Figure 7-28(a), (b) and (c) show the experimental results for the four-channel bilateral control system with CDOB, the four-channel bilateral control system with model-free time delay compensator and the proposed control system. The upper part

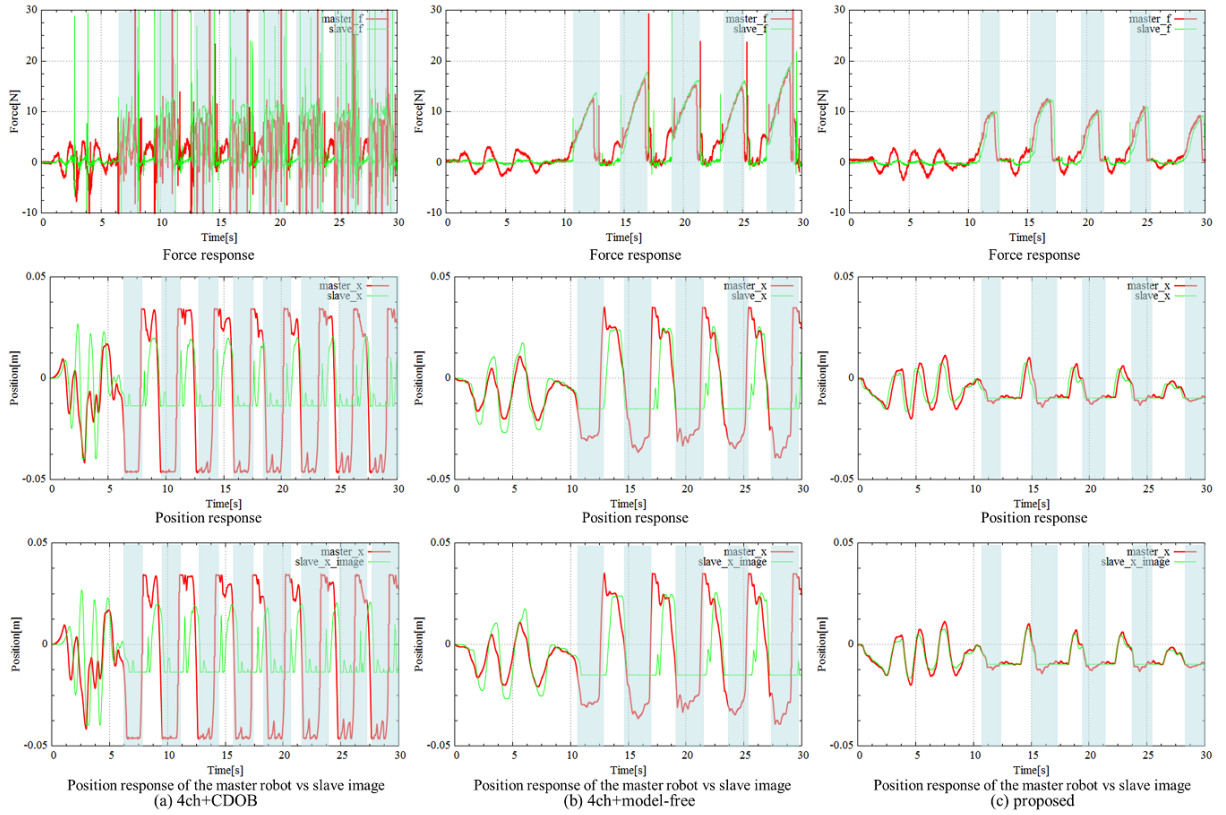


Fig. 7-28: Experimental results.

of Fig. 7-28 shows the force response, the middle part shows the position response and the bottom part shows the position response of the master robot and the visual image of the slave robot. Hatched areas are showing that slave robot contacts environment.

From the bottom part of Fig. 7-28, the position response of the master robot and the visual image of the slave robot are almost same in the proposed control system. Thus, the human operator does not feel a gap between each of them. Additionally, contact and disconnection with environment is stable. From Fig. 7-28 (a), contact with environment is not stable in the four-channel bilateral control system with CDOB. As shown in Fig. 7-28 (b), there is an overshoot in disconnection with environment in the four-channel bilateral control system with model-free time delay compensator.

Thus, it is shown that the proposed control system is valid to synchronize haptic and visual sense.

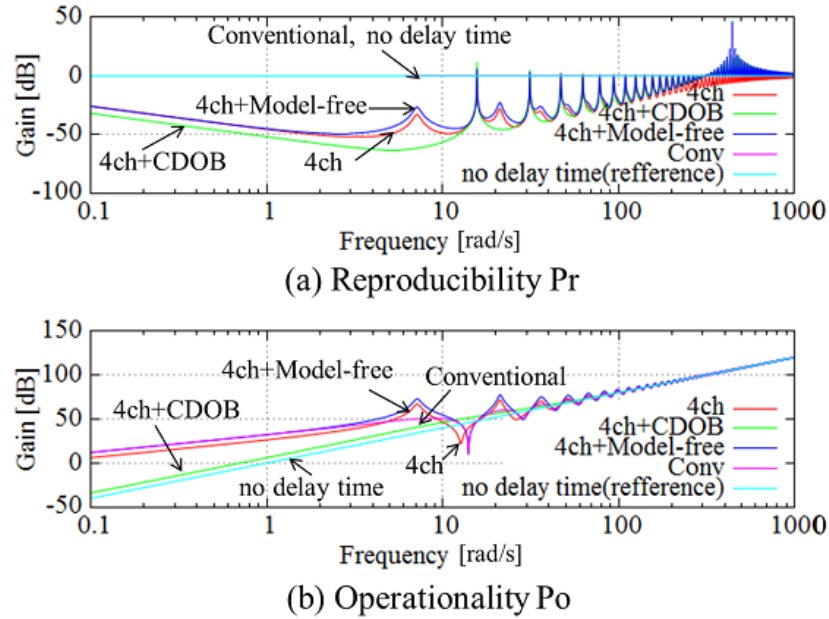


Fig. 7-29: Comparison of performance.

7.6 Performance Improvement

In this section, allocations of HPF are studied to attain the almost same performance with systems which do not include time delay. Firstly, the performance of the conventional bilateral control system is shown. Then, three type of allocations of HPF are studied.

7.6.1 Performance of Conventional Bilateral Control System

In this subsection, the performance of the conventional bilateral control system have been compared. Figure 7-29 shows gain characteristics of reproducibility and operationality for the conventional bilateral control system. Gain characteristics of the four-channel bilateral control system, the four-channel bilateral control system with CDOB, the four-channel bilateral control system with model-free time delay compensator, the conventionally proposed bilateral control system which is explained in 7.5 and the bilateral control system with no time delay are plotted. Here, one way time delay is set as 0.2s.

From Fig. 7-29(a), reproducibility of the conventionally proposed control system is the best compared with other conventional methods. The point is that the gain of reproducibility is 0 in the all frequency area. Therefore, the gain of the environmental impedance is perfectly reproduced in the conventionally

proposed control system. However, as shown in Fig. 7-29(b), operability is not so good compared to other methods. This is because that the position control system adds some undesirable forces. In this section, operability is tried to be improved by allocating HPF in the position control system. This HPF is implemented to remove undesirable forces in the low frequency area.

7.6.2 Allocation of HPF

In this subsection, a case study is conducted for deciding allocations of HPF. Firstly, three types of the allocation are introduced. Then, the stability and the performance for each type are discussed.

Case Study

Figure 7-30 (a), (b) and (c) show the candidates for allocating HPF. In type 1, HPF is allocated to the compensation value of model-free time delay compensator. This is because that the output of the model-free time delay compensator adds some undesirable operational forces to the master robot. HPF will decrease the undesirable operational force in the low frequency area. Additional HPF is allocated in the position control of the master side in type 2. In type 3, additional HPF is allocated in the position control of the slave side.

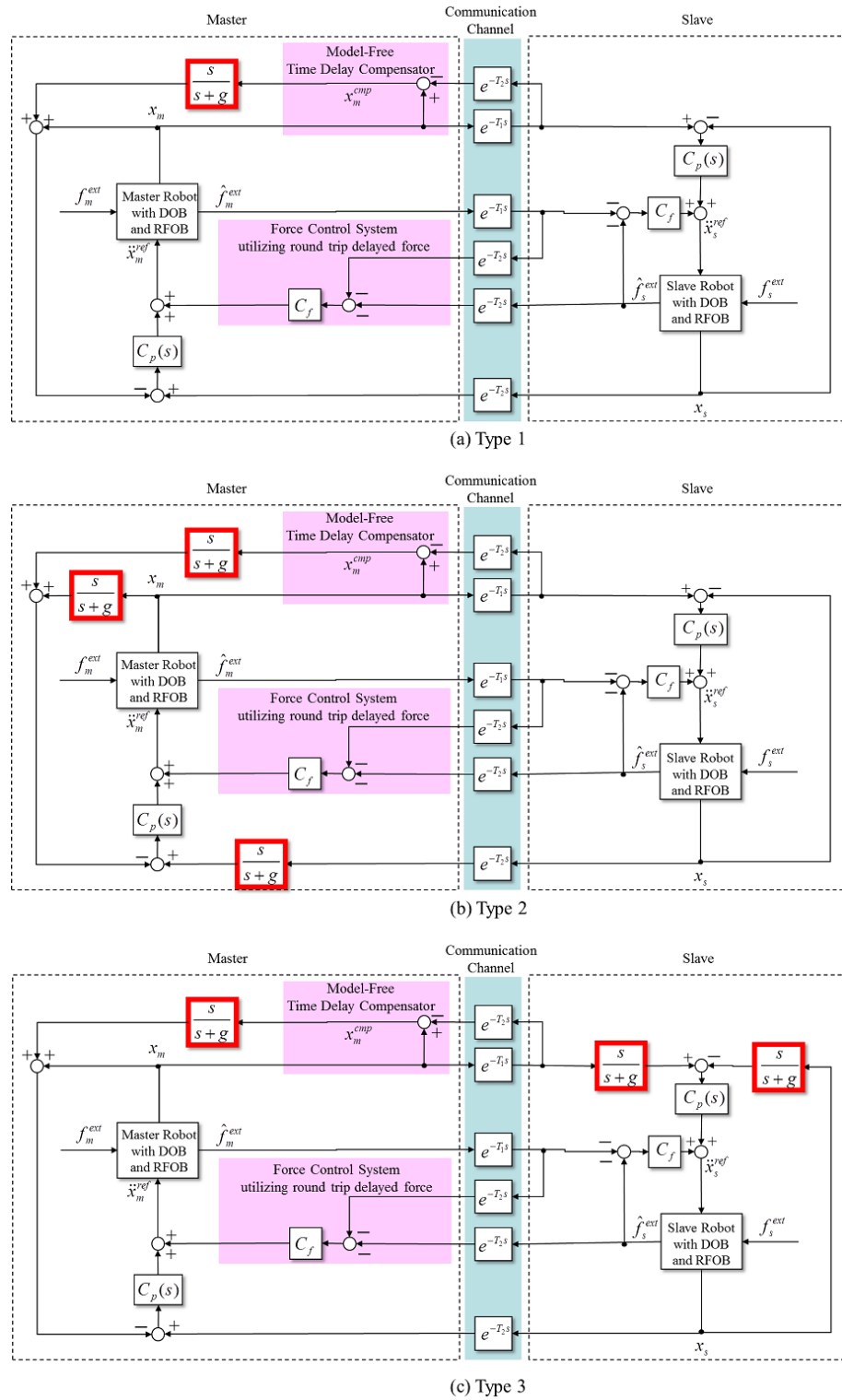


Fig. 7-30: Candidates for allocating the HPF.

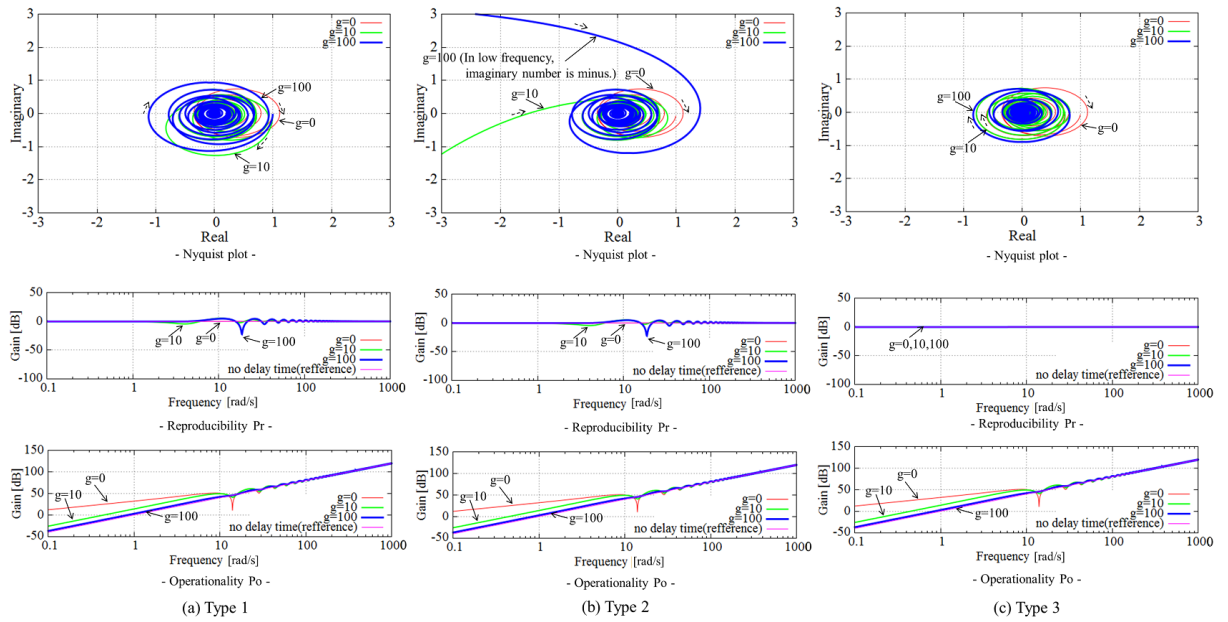


Fig. 7-31: Comparisons from type 1 to type 3.

Discussion of Stability and Performance

In this subsection, the stability and the performance of each type are analyzed. In Fig. 7-31, type 1 to type 3 are compared in the point of the stability and the performance. Upper parts are showing Nyquist diagrams. These Nyquist diagrams are calculated from two flow expression of the bilateral control system. Middle parts are showing gain characteristics of reproducibility. Bottom parts are showing gain characteristics of operability. In all figures, the cut off frequency of HPF is parameterized from 0 to 100 rad/s. In reproducibility and operability, gain characteristics of the four-channel bilateral control system with no time delay are plotted as a reference. Here, one way time delay is set as 0.2s.

From the Nyquist diagram of Fig. 7-31, type 1 and type 2 are destabilized by increasing the cut off frequency of HPF. In type 3, the stability is maintained. From gain characteristics of reproducibility, reproducibility is worsen in type 1 as increasing the cut-off frequency of HPF. In type 2 and type 3, reproducibility is 0 in the all frequency area. From gain characteristics of operability, operability is improved as increasing the cut-off frequency of HPF in type 1 to type 3. From analysis results in Fig. 7-31, type 3 has reproducibility and operability which are almost same in the case of no time delay. Furthermore, the stability is maintained.

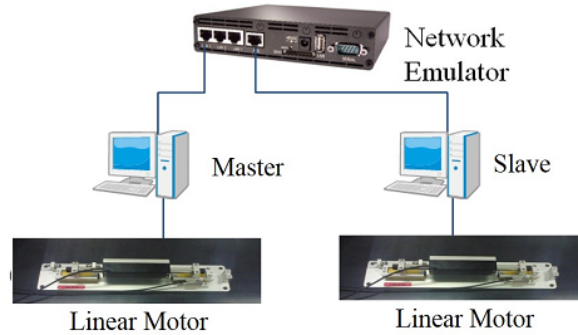


Fig. 7-32: Experimental system.

Table 7.4: Parameters for analysis and experiment

Position feedback gain	K_P	100	
Velocity feedback gain	K_V	20	
Force feedback gain	K_f	0.5	
Cut-off frequency of DOB	g_{dis}	500	rad/s
Cut-off frequency of RFOB	g_{reac}	500	rad/s
Cut-off frequency of CDOB	g_{cdob}	500	rad/s
Human impedance	Z_h	0+0s	
Environmental impedance	Z_e	10000+10s	
Nominal mass	M_n	0.5	kg
Thrust coefficient	K_{tn}	32.5	N/A

7.6.3 Experiment

In this subsection, experimental results are shown to confirm the validity of the proposed system.

Experimental System

Figure 7-32 shows the experimental system. The master and slave system consist of 1-DOF robots. The robot consists of the linear motor and the encoder. A human operator manipulates the master side linear motor, and the slave side linear motor contacts environment. The resolution of the encoder is $0.1 \mu\text{m}$. Time delay is created by the network emulator. In the experiment, one way time delay is set as 200 ms with 30 ms random jitter. The random jitter is given by uniform distribution. In the proposed control

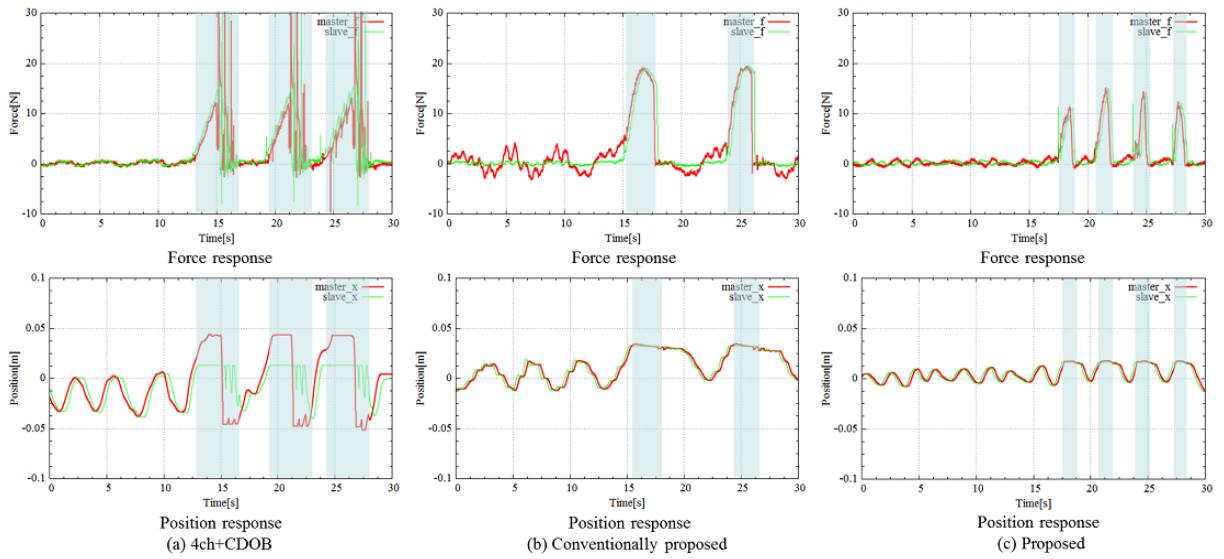


Fig. 7-33: Experimental results.

system, the cut off frequency of HPF is set as 10 rad/s. Here, the proposed control system means type 3 in 7.6.2.

Experimental Results

Figure 7-33 shows the experimental results. The force response of the master robot is plotted in the reverse value to compare with the force response of the slave robot. Figure 7-33(a) show the experimental results for the four-channel bilateral control system with CDOB. Figure 7-33(b) show the experimental results for the conventionally proposed control system. Figure 7-33(c) show the experimental results for the proposed control system. The upper part of Fig. 7-33 shows the force response, and the bottom part shows the position response.

From Fig. 7-33 (a), contact and disconnection with environment are not stable in the four-channel bilateral control system with CDOB. On the other hand, from Fig. 7-33 (b), contact and disconnection with environment is stable in the conventionally proposed control system. Moreover, there is no overshoot in the position response before and after contact with environment. As shown in Fig. 7-33 (c) the operational force is decreased in the proposed control system. Therefore, it is shown that the proposed control system is valid to reduce the operational force.

7.7 Summary

In this chapter, model-free time delay compensator has been proposed. The proposed control system does not utilize the time delay model and the plant model, but the position control and the force control of the bilateral control system are stabilized. A bilateral control system to synchronize haptic and visual sense has also been proposed. By utilizing the proposed method, reproducibility is well improved and the gain of the environmental impedance is reproduced in the all frequency area. Moreover, allocations of HPF have been studied to attain almost the same performance with systems which do not include time delay. By allocating HPF correctly, operability is improved with keeping the stability and reproducibility.

Chapter 8

Conclusions

In this dissertation, to establish fundamental technologies of motion control for haptics, haptic data analysis, haptic display and communication technologies are researched.

Chapter 3 to Chapter 5 focused on haptic data analysis and haptic display technologies as basic researches of motion control for haptics. Chapter 3 proposed the flexible actuator as robot hand mechanisms for haptics. The position and the force transfer characteristics of the flexible actuator have been verified. It was shown the flexible actuator was considered to be valuable for robot hand mechanisms for haptics. Moreover, as one of the application of the flexible actuator, the experimental results of the bilateral teleoperation system with the flexible actuator were shown. Chapter 4 focused on haptic data analysis and display for environmental impedances. A method for abstraction of environment based on frequency characteristics has been proposed. The force response and the position response of environment were transformed from time domain to frequency domain. Then, frequency characteristics of environment were abstracted. A method for reproduction of environment using FIR filter was also proposed. Desired frequency characteristics were approximated by using FIR filter. This method is valuable for abstraction and reproduction of real environment based on frequency characteristics. Chapter 5 focused on haptic analysis and display for human motions. This chapter defined human action mode and environmental action mode. A measured haptic motion was divided to each human action and environmental action by human action mode and environmental action mode. Furthermore, two types of haptic motion display systems were designed. One was based on human action mode. The other was based on human action mode and environmental action mode.

Chapter 6 and Chapter 7 focused on communication technology for applying haptics to delayed com-

munication systems. Chapter 6 studied the time delay effect to motion control systems. This chapter proposed the control system which is robust to unstable time delay. This chapter modified the structure of time delayed control system with CDOB considering unstable time delay. As the nonlinear effect like communication packet dropouts or jitter can deteriorate the total control system with integrators, a case study has been accomplished considering allocations of the system model in CDOB. Then, the more robust CDOB structure against packet dropouts and jitter was designed. Chapter 7 proposed the bilateral teleoperation system for delayed communication systems. Firstly, model-free time delay compensator was proposed. The proposed control system did not utilize the time delay model and the plant model, but the position control and the force control of the bilateral control system were stabilized. A bilateral teleoperation system to synchronize haptic and visual sense was also proposed. Moreover, allocations of HPF were studied to attain the almost same performance with no time delay system. By allocating HPF correctly, the performance was improved with keeping the stability.

The technology of haptic data analysis will contribute to construct knowledge data bases of the environmental stiffness and the human motion. The technology of haptic display will be a basement of haptic training systems. The flexible actuator will be the key structure for the robot hand mechanism for haptics. Proposed theories relating to delayed communication systems will widen the applications such as telesurgeries and haptic communications like telephones.

Each technology is integrated in future applications. When a remote teleoperation is conducted by using communication technology, haptic data analysis technology will be needed to analyze and record the environmental impedance of the remote sight. In case of teleoperations, the normal motion should be automatized and the special motion should be manualized to focus on the special operation. Thus, for the teleoperation of multi degree of freedom robots, haptic display technology should be applied to the normal motion and communication technology should be applied to the special motion.

For expanding the haptics to multi degree of freedom robot hands, manipulability problems have to be considered for realizing targeted motions. Two solutions are considered. First one is to constraint the working area. Second one is to constraint mechanical interfaces as same with human beings. The outcomes will be varied whether directions are taken.

References

- [1] H. Shirado and T. Maeno, “Modeling of Structure and Tactile Sensation of Human Finger”, *Journal of Instrument and Control Engineers*, Vol. 45, No. 12, pp.1005–1009, 2006.(in Japanese)
- [2] Y. Iwamura, “Structure and function of human tactile receptors”, *Journal of the Robotics Society of Japan*, Vol. 2, No. 5, pp. 438–444, 1984.(in Japanese)
- [3] S. Usui, “Signal Analysis”, *Ohmsha*, 1998.(in Japanese)
- [4] S. Liapis and G. Tziritas, “Color and texture image retrieval using chromaticity histograms and wavelet frames”, *IEEE Trans. on Multimedia*, Vol. 6, No. 5, pp. 676 – 686, 2004.
- [5] T. Maeno, “Structure and Function of Finger Pad and Tactile Receptors”, *Journal of the Robotics Society of Japan*, Vol. 18, No. 6, pp. 772–775, 2000. (in Japanese)
- [6] H. Shinoda, “Tactile Sensing for Dexterous Hand”, *Journal of the Robotics Society of Japan*, Vol. 18, No. 6, pp. 767–771, 2000. (in Japanese)
- [7] M. Reiner, “The role of haptics in immersive telecommunication environments”, *IEEE Trans. on Circuits and Systems for Video Technology*, Vol. 14, No. 3, pp. 392–401, 2004.
- [8] T. Tsuji, T. Shimazaki and M. Kaneko, “Analysis of Human Perception Ability for Robot Impedance”, *Journal of the Robotics Society of Japan*, Vol. 20, No. 2, pp. 180–186, 2002. (in Japanese)
- [9] K. Salisbury, F. Conti, and F. Barbagli, “Haptic rendering: introductory concepts”, *IEEE Computer Graphics and Applications Magazine*, Vol. 24, No. 2, pp. 24–32, 2004.
- [10] Y. Yokokohji and T. Yoshikawa, “Bilateral control of master-slave manipulators for ideal kinesthetic coupling – formulation and experiment”, *IEEE Trans. on Robotics and Automation*, Vol. 10, No. 5, pp. 605 – 620, 1994.
- [11] K. Hastrudi-Zaad and S. E. Salcudean, “On the use of local force feedback for transparent teleoperation”, In Proc. of *IEEE International Conf. Robotics and Automation*, pp. 1863 – 1869, 1999.

References

- [12] B. Hannaford, “A design framework for teleoperators with kinesthetic feedback”, *IEEE Trans. on Robotics and Automation*, Vol. 5, No. 4, pp. 426 – 434, 1989.
- [13] D. A. Lawrence, “Stability and transparency in bilateral teleoperation”, *IEEE Trans. on Robotics and Automation*, Vol. 9, No. 5, pp. 624–637, 1993.
- [14] T. Tanikawa and T. Arai, “Development of a micro-manipulation system having a two-fingered micro-hand”, In Proc. of *IEEE International Conf. on Robotics and Automaction*, pp. 152–162, 1999.
- [15] G. Venture, D. S. Haliyo, A. Micaelli, and S. Regnier, “Force-feedback coupling for micro-handling applications”, *Journal of Micromechatronics*, Vol. 3, No. 3–4, pp. 307–327, 2006.
- [16] H. Kajimoto, N. Kawakami, T. Maeda and H. Tachi, “Electrocutaneous Display with Receptor Selective Stimulations”, *Journal of IEICE*, Vol. j84-D-II, No. 1, pp. 120–128, 2001. (in Japanese)
- [17] T. Shimono, S. Katsura, and K. Ohnishi, “Abstraction and Reproduction of Force Sensation From Real Environmenta by Bilateral Control”, *IEEE Trans. on Robotics*, Vol. 54, No. 2, pp. 907–918, 2007.
- [18] K. Ohnishi, S. Katsura, and T. Shimono, “Robot as physical agentn”, In Proc. of *IEEE International Conf. on Industrial Technology, Keynote Lecture - I*, 2006.
- [19] T. Yoshikawa, “Manipulability of Robotic Mechanisms”, *Internation Journal of the Robotics Research*, Vol. 4, pp. 3–9, 1985.
- [20] J. T. Y. Wen and L. S. Wilfinger, “Kinematic Manipulability of General Constrained Rigid Multi-body Systems”, *IEEE Trans. on Robotics and Automation*, Vol. 15, No. 5, pp. 558–567, 1999.
- [21] Y. Yokokohji, “Dynamic Manipulability of Multifingered Grasping”, *IEEE Trans. on Robotics*, Vol. 25, No. 4, pp. 947–954, 2009.
- [22] Y. Yokokoji and T. Yoshikawa, “Design Guide of Master Arms Considering Operator Dynamics”, *ASME Journal of Dynamic Systems, Measurement, and Control*, Vol. 115, pp. 253–260, 1985.
- [23] E. Steinbach, S. Hirche, M. Ernst, F. Brandi, R. Chaudhari, J. Kammerl and I. Vittorias, “Haptic Communications”, *Proc. of IEEE*, Vol. 100, No. 4, pp. 937–956, 2012.
- [24] R. Liu, A. Monti, F. Ponci and A. H. C. Smith, “A Design Approach For Digital Controllers Using Reconfigurable Network-Based Measurement”, *IEEE Trans. on Instrumentation and Measurement*, Vol. 59, No. 5, pp. 1073–1081, 2010.

References

- [25] G. Niemeyer and J. J. E. Slotine, “Stable Adaptive Teleoperation,” *IEEE Journal of Oceanic Engineering*, Vol. 16, No. 1, pp. 152–162, 1991.
- [26] K. Ohnishi, M. Shibata, and T. Murakami, “Motion control for advanced mechatronics”, *IEEE/ASME Trans. on Mechatronics*, Vol. 1, No. 1, pp. 56–67, 1996.
- [27] T. Murakami, F. Yu, and K. Ohnishi, “Torque sensorless control in multidegree-of-freedom manipulator”, *IEEE Trans. on Industrial Electronics*, Vol. 40, No. 2, pp. 259–265, 1993.
- [28] S. Katsura, Y. Matsumoto, and K. Ohnishi, “Analysis and experimental validation of force bandwidth for force control”, *IEEE Trans. on Industrial Elements*, Vol. 53, No. 3, pp. 922–928, 2006.
- [29] N. Nishikawa, T. Murakami, and K. Ohnishi, “Variable Compliance Control for 3 Dimensional Biped Robot considering Environmental Fluctuations”, *IEEJ Transaction on Industry Applications*, Vol. 126, No. 5, pp. 630–638, 2006. (in Japanese)
- [30] T. Tsuji, H. Nishi, and K. Ohnishi, “A Controller design method of decentralized control system”, *IEEJ Transaction on Industry Applications*, Vol. 126, No. 5, pp. 630–638, 2006.
- [31] Y. Matsumoto, S. Katsura, and K. Ohnishi, “An analysis and design of bilateral control based on disturbance observer”, In Proc. of *IEEE Internatinal Conf. on Industrial Technology*, pp. 802–807, 2003.
- [32] K. J. Kyriakopoulos, J. V. Riper, A. Zink, and H. E. Stephanou, “Kinematic analysis and position/force control of the anthropot dexterous hand”, *IEEE Trans. on Systems, Man, and Cybernetics*, Vol. 27, No. 1, pp. 95–104, 1997.
- [33] G. S. Gupta, S. Chandra, C. H. Messom, and S. N. Demidenko, “Master-slave control of a teleoperated anthropomorphic robotic arm with gripping force sensing”, *IEEE Trans. on Instrumentation and Measurement*, Vol. 55, No. 6, pp. 2136–2145, 2006.
- [34] T. Morizono, K. Kurahashi, and S. Kawamura, “Analysis and control of a force display system driven by parallel wire mechanism”, *Journal of Robotica*, Vol. 16, pp. 551–563, 1998.
- [35] S. Kawamura, S. Tanaka W. Choe, and S. R. Pandian, “Development of an ultrahigh speed robot FALCON using wire drive system”, In Proc. of *IEEE International Conf. on Robotics and Automation*, pp. 215–220.
- [36] G. M. Prisco and M. Bergamasco, “Dynamic modeling of a class of tendon driven manipulators”, In Proc. of *IEEE International Conf. on Advanced Robotics*, pp. 893–899, 1997.

References

- [37] K. Ikuta and M. Nokata, “Two-lead-wire drive for multi-micro actuators”, In Proc. of *IEEE International Conf. on Robotics and Automation*, pp. 2378–2384, 1999.
- [38] H. Kino and S. Kawamura, “Development of a serial link structure / parallel wire system for a force display”, In Proc. of *IEEE International Conf. on Robotics and Automation*, pp. 829–834, 2002.
- [39] G. Rosati, P. Gallina, and S. Masiero, “Design, implementation and clinical tests of a wire-based robot for neurorehabilitation”, *IEEE Trans. on Neural Systems and Rehabilitation Engineering*, Vol. 15, No. 4, pp. 560–569, 2007.
- [40] C. Ferraresi, M. Paoloni, and F. Pescarmona, “A new methodology for the determination of the workspace of Six-DOF redundant parallel structures Actuated by Nine Wires”, *Journal of Robotica*, Vol. 25, pp. 113–120, 2007.
- [41] L. R. Lin and H. P. Huang, “Integrating fuzzy control of the dexterous national taiwan university (NTU) hand”, *IEEE/ASME Trans. on Mechatronics*, Vol. 1, pp. 216–229, 1996.
- [42] H. Kawasaki, T. Komatsu, and K. Uchiyama, “Dexterous anthropomorphic robot hand with distributed tactile sensor: gifu hand II”, *IEEE/ASME Trans. on Mechatronics*, Vol. 7, No. 3, pp. 296–303, 2002.
- [43] I. Yamano and T. Maeno, “Five-fingered robot hand using ultrasonic motors and elastic elements”, In Proc. of *IEEE International Conf. on Robotics and Automation*, pp. 2673–2678, 2005.
- [44] W. Iida and K. Ohnishi, “Reproducibility and operationality in bilateral teleoperation”, In Proc. of *IEEE Workshop on Advanced Motion Control*, pp. 217–222, 2004.
- [45] K. Tsuji, Y. Soeda, H. Nagatomi, M. Kitajima, Y. Morikawa, S. Ozawa, T. Furukawa, T. Kawai, and K. Ohnishi, “Free allocation of actuator against end-effector by using flexible actuator”, In Proc. of *IEEE Workshop on Advanced Motion Control*, pp. 329–333, 2006.
- [46] S. Hyodo and K. Ohnishi, “Transmission of force sensation using linear motor and release”, In Proc. of *IEEE International Conf. on Industrial Technology*, pp. 842–847, 2006.
- [47] N. A. Tanner and G. Niemeyer, “High-frequency acceleration feedback in wave variable tele-robotics,” *IEEE/ASME Trans. on Mechatronics*, vol. 11, no. 2, pp. 119–127, 2006.
- [48] J. J. Abbott and A. M. Okamura, “Effects of position quantization and sampling rate on virtual-wall passivity”, *IEEE Trans. on Robotics*, Vol. 21, No. 5, pp. 952–964, 2005.

References

- [49] J. E. Colgate and J. M. Brown, “Factors affecting the z-width of a haptic display”, In Proc. of *IEEE Robot. Autom.*, pp. 3205–3210, 1994.
- [50] N. Diolaiti, C. Melchiorri, and S. Stramigioli, “Contact impedance estimation for robotic systems”, *IEEE Trans. on Industrial Electronics*, Vol. 21, No. 5, pp. 925–935, 2005.
- [51] J. Jiang, J. Xia, and G. Xiao, “MPEG-2 based lossless video compression”, *IEEE Trans. on Multimedia*, Vol. 153, No. 2, pp. 244–252, 2006.
- [52] J. Jiang, J. Xia, and G. Xiao, “B-spline design of maximally flat and prolate spheroidal-type FIR filters”, *IEEE Trans. on Signal Processing*, Vol. 47, No. 3, pp. 701–716, 1999.
- [53] J. Jiang, J. Xia, and G. Xiao, “FIR filter design: frequency-sampling method based on evolutionary programming”, In Proc. of *IEEE Evolutionary Computation*, pp. 244–252, 2006.
- [54] P. Vadakkepat, P. Lim, L. C. D. Silva, L. Jing, L. L. Ling, “Multimodal approach to human–face detection and tracking” *IEEE Trans. on Industrial Electronics* , vol. 55, no. 3, pp. 1385–1393, 2008.
- [55] R. Stiefelhagen, H. K. Ekenel, C. Fugen, P. Gieselmann, H. Holzapfel, F. Kraft, K. Nickel, M. Voit and A. Waibel, “Enabling Multimodal Human–Robot Interaction for the Karlsruhe Humanoid Robot,” *IEEE Trans. on Robotics* , vol. 23, no. 5, pp. 840–851, 2007.
- [56] E. Sato, T. Yamaguchi and F. Harashima, “Natural interface using pointing behavior for human–robot gestural interaction,” *IEEE Trans. on Industrial Electronics* , vol. 54, no. 2, pp. 1105–1112, 2007.
- [57] H. Prendinger and M. Ishizuka, “Symmetric multimodality revisited: unveiling users’ physiological activity,” *IEEE Trans. on Industrial Electronics*, vol. 54, no. 2, pp. 692–698, 2007.
- [58] N. Kubota and K. Nishida, “Perceptual control based on prediction for natural communication of a partner robot,” *IEEE Trans. on Industrial Electronics*, vol. 54, no. 2, pp. 868–877, 2007.
- [59] T. Takeda, Y. Hirata and K. Kosuge, “Dance step estimation method based on HMM for dance partner robot,” *IEEE Trans. on Industrial Electronics*, vol. 54, no. 2, pp. 699–706, 2007.
- [60] H. N. Chow and Y. Xu, “Learning human navigational skill for smart wheelchair in a static cluttered route,” *IEEE Trans. on Industrial Electronics*, vol. 53, no. 4, pp. 1350–1361, 2006.
- [61] V. I. Pavlovic, R. Sharma and T. S. Huang, “Extraction of essential interactions through multiple observations of human demonstrations,” *IEEE Trans. on Industrial Electronics*, vol. 50, no. 4, pp. 667–675, 2003.

References

- [62] M. Skubic and R. A. Volz, "Acquiring robust, force-based assembly skills from human demonstration," *IEEE Trans. on Robotics and Automation*, vol. 16, no. 6, pp. 772–781, 2000.
- [63] S. Katsura and K. Ohishi, "Transmission of force sensation by environment quarryer based on multilateral control," *IEEE Trans. on Industrial Electronics*, vol. 54, no. 2, pp. 898–906, 2007.
- [64] Y. Yokokohji and T. Yoshikawa, "Bilateral control of master-slave manipulators for ideal kinesthetic coupling—formulation and experiment," *IEEE Trans. on Robotics and Automation*, vol. 10, no. 5, pp. 605–620, 1994.
- [65] B. Hannaford, "A design framework for teleoperators with kinesthetic feedback," *IEEE Trans. on Robotics and Automation*, vol. 5, no. 4, pp. 426–434, 1989.
- [66] K. B. Sim, K. S. Byun and F. Harashima, "Internet-based teleoperation of an intelligent robot with optimal two-layer fuzzy controller," *IEEE Trans. on Industrial Electronics*, vol. 53, no. 4, pp. 1362–1372, 2006.
- [67] S. Katsura and K. Ohishi, "Acquisition and analysis of finger motions by skill preservation system," *IEEE Trans. on Industrial Electronics*, vol. 54, no. 6, pp. 3533–3361, 2007.
- [68] M. Morisawa and K. Ohnishi, "Motion control taking environmental information into account," *EPE Journal*, vol. 12, no. 4, pp. 37–41, 2002.
- [69] R. Kubo and K. Ohnishi, "Mechanical Recognition of Unknown Environment Using Active/Passive Contact Motion," *IEEE Trans. on Industrial Electronics*, vol. 56, no. 5, pp. 1364–1374, 2009.
- [70] T. Tsuji, K. Ohnishi and A. Šabanović, "A controller design method based on functionality," *IEEE Trans. on Industrial Electronics*, vol. 54, no. 6, pp. 3335–3343, 2007.
- [71] F. T. Luk and H. Park, "A proof of convergence for two parallel jacobi SVD algorithms," *IEEE Trans. on Computers*, vol. 38, no. 6, pp. 806–811, 1989.
- [72] L. Feng, H. Kun and W. Shunjun, "Research for acquiring eigenvector of real symmetric matrix," *Proc. of the IEEE International Conference on CIE*, pp. 1–3, 2006.
- [73] A. Muis, A. Kato, T. Tsuji, and K. Ohnishi, "RTLinux based real-time control cooperation through internet protocol", In *Proc. of IEEE International Conf. on Mechatronics and Robotics*, pp. 117–122, 2004.
- [74] J. P. Richard, "Time-delay systems; an overview of some recent advances and open problems," *Automatica*, Vol. 39, No. 10, pp. 1667–1694, 2003.

References

- [75] R. A. Gupta and M. Y. Chow, “Networked Control System: Overview and Research Trends,” *IEEE Trans. on Industrial Electronics* , Vol. 57, No. 7, pp. 2527–2535,2010.
- [76] W. P. M. H. Heemels, A. R. Teel, N. van de Wouw and D. Nesic, “Networked Control Systems With Communication constraints: Tradeoffs Between Transmission Intervals, Delays and Performance,” *IEEE Trans. on Automatic Control* , Vol. 55, No. 8, pp. 1781–1796,2010.
- [77] X. Yu, F. Yu, W. Hou and X. Wang, “State-of-the-Art of Transmission Protocols for Deep Space Communication Networks,” *Proc. of Conf. on Networking and Distributed Computing* , pp. 123–127, 2010.
- [78] O. J. M. Smith, “A controller to overcome dead time,” *ISA Journal* , Vol. 6, No. 2, pp. 28–33,1959.
- [79] K. J. Astrom, C. C. Hang and B. C. Lim “A New Smith Predictor for Controlling a Process with an Integrator and Long Dead-Time,” *IEEE Trans. on Automatic Control* , Vol. 39, No. 2, pp. 343–345,1994.
- [80] N. Hohenbichler, “All stabilizing PID controllers for time delay systems,” *Automatica* , Vol. 45, No. 11, pp. 2678–2684,2009.
- [81] N. Abe and K. Yamanaka, “Smith Predictor Control and Internal Model Control - A Tutorial -,” *Proc. of the SICE 2003 Annual Conf.* , Vol. 2,pp. 1383–1387, 2003.
- [82] K . Natori and K. Ohnishi, “A Design Method of Communication Disturbance Observer for Time-Delay Compensation, Taking the Dynamic Property of Network Disturbance Into Account,” *IEEE Trans. on Industrial Electronics* , Vol. 55, No. 5, pp. 2152–2168,2008.
- [83] K . Natori, R. Oboe and K. Ohnishi, “Stability Analysis and Practical Design Procedure of Time Delayed Control Systems With Communication Disturbance Observer,” *IEEE Trans. on Industrial Informatics* , Vol. 4, No. 3, pp. 185–197,2008.
- [84] A. A. Rahman and K. Ohnishi, “Robust Time Delayed Control System Based on Communication Disturbance Observer with Inner Loop Input,” *Proc. of the IEEE International Conf. on Industrial Electronics Society*, pp. 1621–1626, 2010.
- [85] K. Natori and K. Ohnishi, “Disturbance-Attenuation Characteristic of A Structure of Time-Delay System with Communication Disturbance Observer,” *Proc. of the IEEE International Conf. on Mechatronics*, pp. 880–885, 2012.
- [86] Y. Ohno, N. Yoshimura and K. Ohnishi, “Analysis and Compensation of Operational Force in Bilateral Control Systems under Time-Varying Delay,” *Proc. of the IEEE International Conf. on Industrial Electronics Society*, pp. 132–137, 2015.

References

- [87] C. L. Philips and H. T. Nagle, “Digital control system analysis and design,” third edition ed. Prentice Hall.
- [88] L. Chan, F. Naghdy and D. Stirling, “Application of Adaptive Controllers in Teleoperation Systems: A Survey,” *IEEE Trans. on Human-Machine Systems*, Vol. 44, No. 3, pp. 337–352, 2014.
- [89] J. H. Cho, H. I. Son, D. G. Lee, T. Bhattacharjee and D. Y. Lee, “Gain-Scheduling Control of Teleoperation Systems Interacting With Soft Tissues,” *IEEE Trans. on Industrial Electronics*, Vol. 60, No. 3, pp. 946–957, 2013.
- [90] A. Y. Mersha, S. Stramigioli and R. Carloni, “On Bilateral Teleoperation of Aerial Robots,” *IEEE Trans. on Robotics*, Vol. 30, No. 1, pp. 258–274, 2014.
- [91] T. Imaida, Y. Yokokohji, T. Doi, M. Oda and T. Yoshikawa, “Ground-Space Bilateral Teloperation of ETS-VII Robot Arm by Direct Bilateral Coupling Under 7-s Time Delay Condition,” *IEEE Trans. on Robotics and Automation*, Vol. 20, No. 3, pp. 499–511, 2004.
- [92] S. Livatino, L. T. D. Paolis, M. Dagostino, A. Zocco, A. Agrimi, A. D. Santis, L. V. Bruno and M. Lapresa, “Stereoscopic Visualization and 3-D Technologies in Medical Endoscopic Teleoperation,” *IEEE Trans. on Industrial Electronics*, Vol. 62, No. 1, pp. 525–535, 2015.
- [93] T. Li, L. Ding, H. Gao, G. Duan and C. Y. Su, “Trilateral Teleoperation of Adaptive Fuzzy Force/Motion Control for Nonlinear Teleoperators With Communication Random Delays,” *IEEE Trans. on Fuzzy Systems*, Vol. 21, No. 4, pp. 610–624, 2013.
- [94] A. Bolopion and S. Regnier, “A Review of Haptic Feedback Teloperation Systems for Micromanipulation and Microassembly,” *IEEE Trans. on Automation Science and Engineering*, Vol. 10, No. 3, pp. 496–502, 2013.
- [95] H. I. Son, J. H. Cho, T. Bhattacharjee, H. Jung and D. Y. Lee, “Analytical and Psychophysical Comparison of Bilateral Teleoperators for Enhanced Perceptual Performance,” *IEEE Trans. on Industrial Electronics*, Vol. 61, No. 11, pp. 6202–6212, 2014.
- [96] I. Nisky, F. A. Mussa-Ivaldi and A. Karniel, “Analytical Study of Perceptual and Motor Transparency in Bilateral Teleoperation,” *IEEE Trans. on Human-Machine Systems*, Vol. 43, No. 6, pp. 570–582, 2013.
- [97] B. Wilaert, D. Reynaerts, H. Brussel and B. V. Poorten, “Bilateral Teleoperation: Quantifying the Requirements for and Restrictions of Ideal Transparency,” *IEEE Trans. on Control Systems Technology*, Vol. 22, No. 1, pp. 387–395, 2014.

References

- [98] T. Ando, R. Tsukahara, M. Seki and G. Fujie, “A Haptic Interface “Force Blinker 2” for Navigation of the Visually Impaired,” *IEEE Trans. on Industrial Electronics*, Vol. 59, No. 11, pp. 4112–4119, 2012.
- [99] G. Du, P. Zhang and D. Li, “Human-Manipulator Interface Based on Multisensory Process via Kalman Filters,” *IEEE Trans. on Industrial Electronics*, Vol. 61, No. 10, pp. 5411–5418, 2014.
- [100] J. Kim, P. H. Chang and H. Park, “Two-Channel Transparency-Optimized Control Architectures in Bilateral Teleoperation With Time Delay,” *IEEE Trans. on Control Systems Technology*, Vol. 21, No. 1, pp. 40–51, 2013.
- [101] H. Li and K. Kawashima, “Achieving Stable Tracking in Wave-Variable-Based Teleoperation,” *IEEE/ASME Trans. on Mechatronics*, Vol. 19, No. 5, pp. 1574–1582, 2014.
- [102] K. Natori, T. Tsuji, K. Ohnishi, A. Hase and K. Jezernik, “Time-Delay Compensation by Communication Disturbance Observer for Bilateral Teleoperation Under Time-Varying Delay,” *IEEE Trans. on Industrial Electronics*, Vol. 57, No. 3, pp. 1050–1062, 2010.
- [103] A. Suzuki and K. Ohnishi, “Frequency-Domain Damping Design for Time-Delayed Bilateral Teleoperation System Based on Modal Space Analysis,” *IEEE Trans. on Industrial Electronics*, Vol. 60, No. 1, pp. 177–190, 2013.
- [104] R. Kubo, N. Iiyama, K. Natori, K. Ohnishi and H. Furukawa, “Performance Analysis of a Three-Channel Control Architecture for Bilateral Teleoperation with Time Delay,” *IEEE Transaction on Industry Applications*, Vol. 127-D, No. 12, pp. 1224–1230, 2007.
- [105] R. G. Bonitz and T. C. Hsia, “Internal Force-Based Impedance Control for Cooperating Manipulators,” *IEEE Trans. on Robotics and Automation*, Vol. 12, No. 1, pp. 78–89, 1996.
- [106] M. Jin, S. H. Kang and P. H. Chang, “Robust Compliant Motion Control of Robot With Nonlinear Friction Using Time-Delay Estimation,” *IEEE Trans. on Industrial Electronics*, Vol. 55, No. 1, pp. 258–269, 2008.
- [107] J. Hua, T. Liang, H. Sun and Z. Lei, “Time-delay Compensation Control of Networked Control Systems Using Time-stamp based State Prediction,” *Proc. of the IEEE Int. Conf. on ISECS*, pp. 198–202, 2008.
- [108] M. Akhlaq and T. R. Sheltami, “RTSP: An Accurate and Energy-Efficient Protocol for Clock Synchronization in WSNs,” *IEEE Trans. on Instrumentation and Measurement*, Vol. 62, No. 3, pp. 578–589, 2013.

List of Achievements

Journals (First Author)

- [1] Shoyo Hyodo and Kouhei Ohnishi, “A Structural Approach to Improve the Stability of Bilateral Control System with Time Delay,” *IEEJ Transactions on Industry Applications*, (Accepted for publication)
- [2] Shoyo Hyodo and Kouhei Ohnishi, “A Two Flow Expression Method of Four-Channel Bilateral Control System with Time Delay and Validation of Model-Free Time Delay Compensator,” *IEEJ Transactions on Industry Applications*, (Accepted for publication)
- [3] Shoyo Hyodo and Kouhei Ohnishi, “A Method for Allocation of System Model in Communication Disturbance Observer Considering Unstable Network,” *IEEJ Transactions on Industry Applications*, vol. 135-D, No. 3, pp. 192–198, 2015. (in Japanese)
- [4] Shoyo Hyodo and Kouhei Ohnishi, “A Method for Motion Abstraction Based on Haptic Information Directionality and An Application to Haptic Motion Display System,” *IEEE Transactions on Industrial Electronics*, vol. 56, No. 5, pp. 1356–1363, 2009.
- [5] Shoyo Hyodo and Kouhei Ohnishi, “A Method for Haptic Motion Abstraction and Display Based on Action Force Directionality,” *IEEJ Transactions on Industry Applications*, vol. 129-D, No. 1, pp. 59–66, 2009. (in Japanese)
- [6] Shoyo Hyodo and Kouhei Ohnishi, “A Method for Abstraction and Reproduction of Environment Based on Frequency Characteristic,” *IEEJ Transactions on Industry Applications*, vol. 128-D, No. 11, pp. 1254–1261, 2008. (in Japanese)
- [7] Shoyo Hyodo, Yujiro Soeda and Kouhei Ohnishi, “Verification of Flexible Actuator From Position and Force Transfer Characteristic and Its Application to Bilateral Teleoperation System,” *IEEE Transactions on Industrial Electronics*, vol. 56, No. 1, pp. 36–42, 2008.

Journals (Co-author)

- [1] Tatsuya Kobayashi, Tomoyuki Shimono, Shoyo Hyodo, and Kouhei Ohnishi, “Transmission of High Precision Force Sensation by Bilateral System with Flexible Actuator,” *IEEJ Transactions on Industry Applications*, vol. 129-D, No 7, pp. 748–755, 2009. (in Japanese)
- [2] Hiroaki Kuwahara, Shigeru Susa, Shoyo Hyodo, and Kouhei Ohnishi, “Design Method for a Bilateral Control System Considering Ambient Environment around Operated Objects,” *IEEJ Transactions on Industry Applications*, vol. 129-D, No 6, pp. 649–657, 2009. (in Japanese)

International Conferences (First Author)

- [1] Shoyo Hyodo, Kouhei Ohnishi,
“A Bilateral Control System to Synchronize with Haptic and Visual Sense for Teleoperation over Network”
Proceedings of the 1st IEEJ International Workshop on Sensing, Actuation, and Motion Control, SAMCON’15, Nagoya, Japan, 2015.
- [2] Shoyo Hyodo, Kouhei Ohnishi,
“Implementation of Dual Model-Free Time Delay Compensator for Bilateral Control System with Time Delay”
Proceedings of the IEEE International Conference on Mechatronics, ICM’15, Nagoya, Japan, pp. 576–581, 2015.
- [3] Shoyo Hyodo, Kouhei Ohnishi,
“A Structure of Bilateral Control System with Time Delay Considering Improvement of Stability”
Proceedings of the 10th IEEE International Workshop on Advanced Motion Control, AMC’14, Yokohama, Japan, pp. 284–289, 2014.
- [4] Shoyo Hyodo, Kouhei Ohnishi,
“A Method for Motion Extraction and Guide Based on Haptic Information Relationship”
Proceedings of the 10th IEEE International Workshop on Advanced Motion Control, AMC’08, Trento, Italy, pp. 428–433, 2008.
- [5] Shoyo Hyodo, Kouhei Ohnishi,
“Transmission of Force Sensation Using Linear Motor and Release”
Proceedings of the IEEE International Conference on Industrial Technology, ICIT’06, Mumbai, India, pp. 842–847, 2006.

- [6] Shoyo Hyodo, Ryogo Kubo, Kouhei Ohnishi,
“A Stable Grasping and Manipulating Control Method Based on Grasp Plane”
Proceedings of the 32nd IEEE Annual Conference of the IEEE Industrial Electronics Society, IECON’06, Paris, France, pp. 4030–4035, 2006.

International Conferences (Co-author)

- [1] Keiichi Taguchi, Shoyo Hyodo, Kouhei Ohnishi,
“A Design Method of Autonomous Hazard Avoidance Controller with Selected Ratio in Bilateral Teleoperation”
Proceedings of the 10th IEEE International Workshop on Advanced Motion Control, AMC’08, Trento, Italy, pp. 607–612, 2008.
- [2] Tatsuya Kobayashi, Yujiro, Soeda, Shoyo Hyodo, Kouhei Ohnishi,
“An Experimental Validation of Flexible Actuator with Torque Wire for Haptic Motion”
Proceedings of the 10th IEEE International Workshop on Advanced Motion Control, AMC’08, Trento, Italy, pp. 595–600, 2008.

Domestic Conference (First Author)

- [1] Shoyo Hyodo, Kouhei Ohnishi,
“Bilateral Control System to Overcome Destabilization from Network Delay”
Proceedings of the 2014 Annual Conference of the IEEJ Industry Applications Society, JIASC ’14, Tokyo, Japan , Vol. 2, pp. 105–110, 2005.
- [2] Shoyo Hyodo, Kouhei Ohnishi,
“A Structure of Time Delayed Control System with Communication Disturbance Observer Considering Unstable Network”
Papers of the IEEJ Technical Meeting on Industrial Instrumentation and Control, IIC-14, Tokyo, Japan , No. 49, 2014. (in Japanese)
- [3] Shoyo Hyodo, Kouhei Ohnishi,
“A Method for Motion Extraction and Guide Based on Action Force Directionality”
Papers of the IEEJ Technical Meeting on Industrial Instrumentation and Control, IIC-08, Tokyo, Japan , No. 130, 2008. (in Japanese)
- [4] Shoyo Hyodo, Kouhei Ohnishi,
“A Method for Abstraction and Reproduction of Environment based on Frequency Characteristic”

Proceedings of the 2007 Annual Conference of the IEEJ Industry Applications Society, JIASC '07, Osaka, Japan , Vol. 2, pp. 397–402, 2007. (in Japanese)

- [5] Shoyo Hyodo, Kouhei Ohnishi,
“A Force Control Method Based on Acceleration Control”
Papers of the IEEJ Technical Meeting on Industrial Instrumentation and Control, IIC-07, Tokyo, Japan , No. 97, 2007. (in Japanese)
- [6] Shoyo Hyodo, Kouhei Ohnishi,
“Manipulating and Grasping Control Taking into Account Contact with Environment” *Papers of the IEEJ Technical Meeting on Industrial Instrumentation and Control, IIC-06*, Hamamatsu, Japan , No. 48, 2006. (in Japanese)

Domestic Conferences (Co-author)

- [1] Tasuya Kobayashi, Shoyo Hyodo, Kouhei Ohnishi,
“Compensation of Disturbance on Flexible Actuator for Bilateral Control”
Papers of the IEEJ Technical Meeting on Industrial Instrumentation and Control, IIC-08, Tokyo, Japan , No. 122, 2008. (in Japanese)
- [2] Hiroaki Kuwahara, Shigeru Susa, Shoyo Hyodo, Kouhei Ohnishi,
“A Design Method of Bilateral Control Taking Ambient Environment into Account”
Papers of the IEEJ Technical Meeting on Industrial Instrumentation and Control, IIC-08, Tokyo, Japan , No. 68, 2008. (in Japanese)
- [3] Keiichi Taguchi, Shoyo Hyodo, Tomoyuki Shimono, Kouhei Ohnishi:
“A Method of Bilateral Teleoperation
Taking Autonomous Hazard Avoidance into Account”
Proceedings of the 2007 Annual Conference of the IEEJ Industry Applications Society, JIASC '07, Osaka, Japan , Vol. 2, pp. 329–334, 2007. (in Japanese)

Awards

[1] Excellent Presentation Award

IEEJ Industry Applications Society

Date: August 28th, 2008.

[2] Young Investigator Award

Tokyo Branch of the IEEE IEEJ Industry Applications Society

Date: March 31th, 2006.

Career

[1] April 2008 – present

Engineer

Mitsubishi Heavy Industries, Ltd.

Space System Division